UNIVERSITY OF CALIFORNIA
RIVERSIDE

Optical Study of Intervalley Excitons and Phonon Replicas in Bilayer WSe_2

A Dissertation submitted in partial satisfaction
of the requirements for the degree of

Doctor of Philosophy

in

Physics

by

Mashael Mutlaq Altaiary

March 2022

Dissertation Committee:
Dr. Chun Hung Lui, Chairperson
Dr. Yongtao Cui
Dr. Peng Wei

The Dissertation of Mashael Mutlaq Altaiary is approved:

Committee Chairperson

University of California, Riverside

ACKNOWLEDGEMENTS

Pursuing a Ph.D. is a distinctive experience. Throughout my journey at UCR, I have had the privilege of both meeting and working with outstanding people and scientists. Completing my Ph.D. has proved an exceptional journey; it has shaped my personality and offered me unrivalled opportunities to be a part of a remarkable community. All the people I have met during the last seven years have taught me to be a better scientist, an honest friend, and a compassionate person.

First and foremost, I would like to thank my advisor Prof. Joshua Lui for his mentorship and support of this work. I first joined his group in July 2016 in the early stage of the construction of the research lab. It has been a pleasant and unique experience for me. He has been supportive and patient. Thank you for giving me the chance to be part of your research group.

I would like to particularly thank our postdoc Erfu Liu, who joined our lab when I was in the third year of my Ph.D. He has made remarkable contributions to our lab. I had a pleasant time working with Erfu, and we worked closely on fabricating two-dimensional (2D) heterostructure devices. We had fruitful discussions about 2D materials research, recent projects, and the potential of conducting specific projects in our lab. This led to the study of intervalley excitons in dual-gated bilayer WSe_2 devices. Erfu conducted the work presented in Chapter 5, and I performed similar measurements in a different bilayer WSe2 device. I am tremendously thankful to you, Erfu, for the time you spent introducing me to scientific experiments and conducting new measurements, and for your talent and the

efforts you dedicated to improving our lab. I am grateful to our theoretical collaborator, Prof. Yia-Chung Chang, who provided thorough theoretical calculations to explain our experimental results of bilayer WSe_2. I am also grateful to Prof. Chang's postdoc and student for their help in the theoretical work.

I would like to thank the current members and some former members of the Lui lab: Jeremiah van Baren, Matthew Wilson, Mohammed Alghamdi, Xian Wang, Benjamin Leong, Jannia Blas Gonzalez, Ao Shi, Tianyi Ouyang. Thank you all for the support and the moments of friendship we spent together in the lab. I also thank Prof. Nathan Gabor, Prof. Yongtao Cui, Prof. Peng Wei, Prof Jing Shi, Fatemeh Barati, Jacky Wan, Mina Rashetnia, for their support and discussions during our work. I thank all the SMALL lab members for sharing experimental equipment and making the shared lab function. I thank Prof. Qiong Ma and the Jarillo-Herrero group for providing me with the great opportunity to work and learn about 2D heterostructure fabrication techniques.

Before joining the Lui group, I was a member in Prof. Robert Haddon's research team. He was a distinguished professor of Chemistry and Chemical and Environmental Engineering, and the Director of the Center of Nanoscale Science & Engineering. Prof. Haddon passed away on April 21, 2016. Prof. Haddon was a pioneer scientist in his fields, a generous, kind, and thoughtful person. He has made impactful contributions to scientific research. Prof. Haddon introduced me to the graduate program at UCR and offered me the opportunity to work with him. I am very honored to have been his student, and tremendously thankful to have the opportunity to learn so much from him. His passing was

a huge loss to the international scientific community, his students, and most importantly to his family, particularly Dr. Elena Haddon. I also owe huge thanks to Dr. Elena Haddon for her support and guidance during my first experiences in the lab. She is a kind and generous lady; I will never forget her help on getting me settled when I first arrived at Riverside. Thanks to Misha Itkis, Nancy Jahr, and all of Prof. Haddon's laboratory members. I am grateful for the privilege of working with you and being a friend of you.

I also owe a tremendous debt of gratitude to Prof. Zain Yamani from King Fahd University of Petroleum and Minerals. I have known Prof. Yamani since my undergraduate days, and he has been a constant source of inspiration since I first took his courses. Throughout my graduate studies, he has been a supportive mentor and served as a great role model of how to be a good scientist and ask good scientific questions. I learned from him how to be a good scientist, think critically, and build up my own networks for research. He has been a constant source of encouragement and guidance, not only in the aspect of research, but also in the aspect of personal interaction and influence on my future career. I sincerely thank Prof. Yamani for his continuous support. I would also like to express my gratitude to Prof. Fahad Al-Marzouki and Prof. Yas Al-Hadeethi from King Abdulaziz University, for their supports.

I would also like to acknowledge several of my friends: Sarah Helalia for all the funny, happy, and knowledgeable moments we spent together at UCR; Najoud Alsaiari for being so supportive and inspiring, and for encouraging me to think positively all the time.

To all the friends whom I have met in the last seven years, thanks for your true friendship. I have learned from all of you, and your friendship has augmented my personal life.

My utmost and very special gratitude goes to my family: my parents Mutlaq and Moznh, without your unwavering unconditional love, support, wisdom, and unlimited patience, this work would not have been possible; my brother Muath, thank you for joining me on part of this journey. We went through difficult times together, but we overcame them; my sisters and brothers, you are the sincerest friends that life has offered me. For that I cannot be more thankful.

Mashael Altaiary

Riverside, CA

DEDICATION

To my beloved parents, for their continuous support and patience
To my sisters, brothers, and friends
And to myself, for remaining strong-willed

"Better to illuminate than merely to shine,
to deliver to others contemplated truths than merely to contemplate."

— Thomas Aquinas

Acknowledgement of Previously Published Material

M. Altaiary, E. Liu, C. T. Liang, F. C. Hsiao, J. van Baren, T. Taniguchi, K. Watanabe, N. Gabor, Y. C. Chang & C. H. Lui, "Electrically switchable intervalley excitons with strong two-phonon scattering in bilayer WSe_2", DOI:10.1021/acs.nanoletter.1c01590

ABSTRACT OF THE DISSERTATION

Optical Study of Intervalley Excitons and Phonon Replicas in Bilayer WSe_2

by

Mashael Mutlaq Altaiary

Doctor of Philosophy, Graduate Program in Physics
University of California, Riverside, March 2022
Dr. Chun Hung Lui, Chairperson

Atomically thin transition metal dichalcogenides (TMDs, *e.g.*, MoS_2, $MoSe_2$, WS_2, WSe_2) exhibit intriguing tunable properties. For instance, their electronic band structure and optical spectra can be significantly modulated under the application of an electric field. Such electrical tunability allows for interesting scientific research and versatile applications of the materials. In this dissertation, we investigate 2H-stacked bilayer WSe_2 dual-gated devices encapsulated by boron nitride. Bilayer WSe_2 hosts two competing low-lying excitons, namely the QK and QΓ intervalley excitons. Although its electronic band structure suggests the QK exciton as the lowest-lying exciton, we observe the QΓ exciton at ~18 meV below the QK exciton. Our observation reveals that the QΓ exciton has larger binding energy than the QK exciton. The QK and QΓ excitons possess different interlayer electric dipole moments, which give rise to different Stark shifts under the application of an out-of-plane electric field. By controlling the electric field, we can switch the energy ordering of the QΓ and QK excitons, and control which exciton dominates the luminescence of bilayer WSe_2. Remarkably, both QΓ and QK excitons exhibit unusually

strong two-phonon replicas, which are comparable to or even stronger than the one-phonon replicas. By detailed theoretical simulation, we infer the existence of numerous two-phonon scattering paths involving (nearly) resonant exciton-phonon scattering in bilayer WSe_2. Such electric-field-switchable intervalley excitons with strong two-phonon replicas make bilayer WSe_2 a distinctive valleytronic material.

We have also observed coherent states between multiple excitons with different center-of-mass momenta in bilayer WSe_2. By studying the reflection spectra, we resolve two weak features arising from KQ and KQ' intervalley excitons. Under the application of the out-of-plane electric field, both excitons exhibit strong Stark splitting, coupled with each other and with the nearby KK intravalley exciton. We can quantitatively simulate the results with a model that considers defect-mediated coherent coupling between the KQ, KQ' and KK excitons. The good experiment-theory agreement strongly supports the emergence of coherent states between momentum-mismatched excitons and provides important insight into the role of defects in coherent excitonic coupling in semiconductors.

Table of Contents

List of Figures

List of Tables

Chapter 1

Introduction and background

1.1 Background of two-dimensional materials

Two-dimensional (2D) materials with intriguing properties have attracted significant scientific and technological interest over the last decade. Bulk crystals composed of van der Waals bonded layers can be separated into stable flakes of a few nanometers atomic thickness. The resulting thin, two-dimensional membranes have demonstrated unique mechanical, electronic, and optical properties which are absent in their bulk counterparts. Such properties are remarkably tunable by doping, external fields, strain, and environmental effects. The most important aspect of 2D material is that it can be easily integrated into other systems or devices, or stacked layer by layer to build heterostructures with desired functionalities.

Following the successful isolation of a single layer of carbon atoms arranged in the hexagonal honeycomb structure, graphene, the field of 2D material has grown rapidly, and further materials have been explored. Yet graphene was the first two-dimensional material known to researchers (**Figure 1.1)**. Before diving into the great importance of graphene, it is imperative to establish the definition of 2D crystals. A single atomic plane is undoubtedly a 2D crystal, while more than 50 layers are considered a thin film of 3D material. However, we need to determine the maximum number of layers at which a structure is to still be considered a 2D crystal.

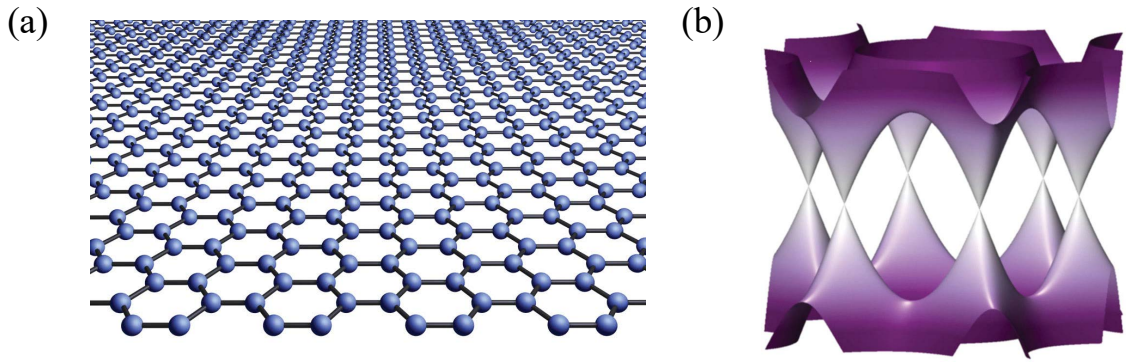

Figure 1.1. The crystal structure of graphene: (a) a hexagonal honeycomb lattice of carbon atoms; **(b)** energy band structure of graphene. Adopted from [93].

In the case of graphene, studies have shown that the electronic structure evolves with respect to film thickness, reaching the 3D threshold at a thickness of 10 layers [1]. Moreover, graphene and its bilayer are zero-gap semiconductors and have relatively simple electronic bands. The electronic bands become increasingly complicated for more than three layers: significant overlapping occurs in the conduction and valence bands with several charge carriers.

Numerous properties of graphene, such as mechanical stiffness, strength and elasticity, and electrical and thermal conductivity, are exceptional. These superior properties justify graphene's nickname, 'miracle material.' Moreover, graphene research has evolved rapidly because laboratory procedures allow researchers to obtain relativity simple and cheap high-quality graphene. Its characteristics have been measured experimentally and have exceeded those obtained in any other material, with some reaching theoretically predicted limits. For example, graphene's electron mobility at room

temperature is 2.5 x 10^5cm $V^{-1}s^{-1}$ [2] (theoretical limit ~ 2x10^5 cm V^{-1} s^{-1}) [3]; its Young's modulus is 1 TPa, and intrinsic strength, 130 GPa [4]; these experimental values are very close to those predicted by theory [5]. In addition, it exhibits very high thermal conductivity above 3,000 W mK^{-1} [6], optical absorption at infrared wavelengths of exactly $\pi\alpha \approx 2.3\%$ (where α is the fine structure constant) [7], and high sustainability of extremely high electric fields, a million times higher than copper [8].

Two findings were surprising: the existence of isolated atomic planes of graphene, and the fact that it remains continuous and conductive under ambient conditions. There are many reasons to be surprised by the survival of the graphene lattice. First, over many decades studies of ultrathin films have shown that it is very challenging to fabricate continuous monolayer materials [9]; because of a process called 'island growth,' a material coagulates into small islands. Such a process is driven by the fact that a system tends to minimize its surface energy. The second reason is that theory shows that an isolated monolayer graphene should be thermodynamically unstable, with calculations indicating that carbon structure is least stable until approximately 6000 atoms [10]. 3D configuration is energetically more favorable than 2D configuration until ~24000 [11]. In cases with large-sized graphene sheets, calculations also indicate instability with regard to scrolling due to the competing contributions from the bending and surface energies [12]. Another surprising finding is the claim that a 2D crystal cannot be grown without an epitaxial substrate to provide an atomic bonding. The Landau-Peierls reveals that the density of thermal fluctuation of 2D crystal in a 3D space diverges with temperature [13]. Finally, the

most important finding is that graphene remines stable under ambient conditions. Normally surfaces of materials can react with air and become moisturized. Thus, ultrahigh vacuum facilities and liquid helium temperatures allow the surface materials to stabilize and avoid reactive species. Monolayer graphene has two surfaces, leading us to expect it to be more reactive in air. However, graphene flouts all of the above considerations. First, most methods of obtaining graphene start with a 3D bulk crystal or a sheet of graphene formed on top of an epitaxial substrate. This procedure quenches the diverging thermal fluctuation. Second, cleaving and releasing of graphene from the substrate is typically carried out at room temperature. Thus, the energy barriers remain high, allowing the atomic planes to form isolated, non-scrolled graphene sheets without any substrate. This is least favorable energetically, however. On the other hand, if graphene is placed on the substrate, van der Waals interaction would also be sufficient to prevent it from scrolling. Third, ambient conditions appear sufficient for graphene lattice to survive. Since graphene reacts weakly with air and pollutants at room T, a temperature > 300^{o}C is required to damage graphene in the air.

An important aspect of graphene's utility was the fact it is possible to observe under an optical microscope when a sheet of graphene placed on a Si wafer with a chosen thickness of SiO_2 results in an interference-like contrast with respect to the wafer. This makes scanning substrates in search of graphene crystallites very simple. Indeed, finding graphene always requires special care because a slight change in the SiO_2 thickness affects the interference contrast. For example, a 5% difference in SiO_2 thickness makes a single

layer of graphene completely invisible. In addition, Raman microscopy can be helpful for a rapid inspection of thickness.

Although there is a new class of 2D materials, an abundance of theoretical and experimental efforts have focused on graphene. The significant electronic quality exhibited by the isolation of graphene layers is the primary reason for this considerable interest. Charge carriers in graphene ambipolar electric field effects can be tuned continuously between electrons and holes with concentration n as high as 10^{13} cm^{-2}, and mobilities μ can exceed 15,000 cm^{-2} V^{-1} s^{-1} under ambient conditions. In fact, graphene mobilities depend on temperature, meaning that μ at 300 K is limited by impurity scattering. Therefore, it can be improved up to ≈100,000 cm^{-2} V^{-1} s^{-1}. A further indication of the system's exponential electronic quality is the observation of quantum hall effect (QHE) even at room temperature [14].

Another reason for this interest is the unique nature of graphene charge carriers. In condensed matter physics, the Schrödinger equation describes an electronic property of materials. However, the relativistic nature of charge carriers in graphene is more easily used in the Dirac equation than in the Schrödinger equation [15–17]. Electrons' interaction with the periodic potential of graphene's honeycomb lattice give rise to new quasiparticles. These new quasiparticles are called massless Dirac fermions, which at low energy are accurately described by the Dirac equation with an effective speed of light $\nu_F \approx 10^6$ m^{-1} s^{-1}. Furthermore, graphene's zero-field conductivity σ exhibits value close to the conductivity quantum e^2/h per carrier in the limit of vanishing the carrier's concentration n.

The fact that graphene has metallic behaviour even at the neutrality point is a significant problem for logic applications. The distinctive linear dispersion relation in graphene gives extraordinary optical and electronic properties, but zero-gap energy greatly limits graphene applications for semiconductors. Therefore, discovering monolayer group-VIB transition metal dichalcogenides (TMDs), MX_2 (M = Mo, W; X= S, Se), has opened a new window for photonics and optoelectronics.

1.2 Transition metal dichalcogenides

The emergence of transition metal dichalcogenides brings excitement and puzzlement to the field of 2D materials, as it offers a broad range of electronic properties, from insulating or semiconducting (e.g., Ti, Hf, Zr, Mo, and W dichalcogenides) to metallic or semi-metallic (V, Nb, and Ta dichalcogenides). All TMDs have a hexagonal structure, with each monolayer comprising a single layer of metal sandwiched between two layers of chalcogenide atoms in the formula MX_2 (X-M-X). Trigonal prismatic (e.g., MoS_2 and WS_2) and octahedral (e.g., TiS_2) are the most common polytypes. Their bulk structures built up a stacking of monolayers of weak van der Waals-like forces and strong covalent bonds that provide in-plan stabilities of monolayers.

1.2.1 Metallic transition metal dichalcogenides materials

The density of states (DOS) of metallic TMDs materials has two major features. First, for undoped materials the fermi level always crosses the d-orbital of the metal layers allowing electrons to move mostly inside the metal layers. Second, the Fermi level lies

higher than semiconductors or insulators (**Figure 1.2).** This can explain the phase transitions that occur in these materials. The great interest in these materials arises from the existence of charge density waves (CDWs) and superconductivity in their phase diagrams. In the CDW phase, a gap is opened, and the DOS is suppressed at the Fermi level; there must be a finite DOS for the superconducting phase to occur.

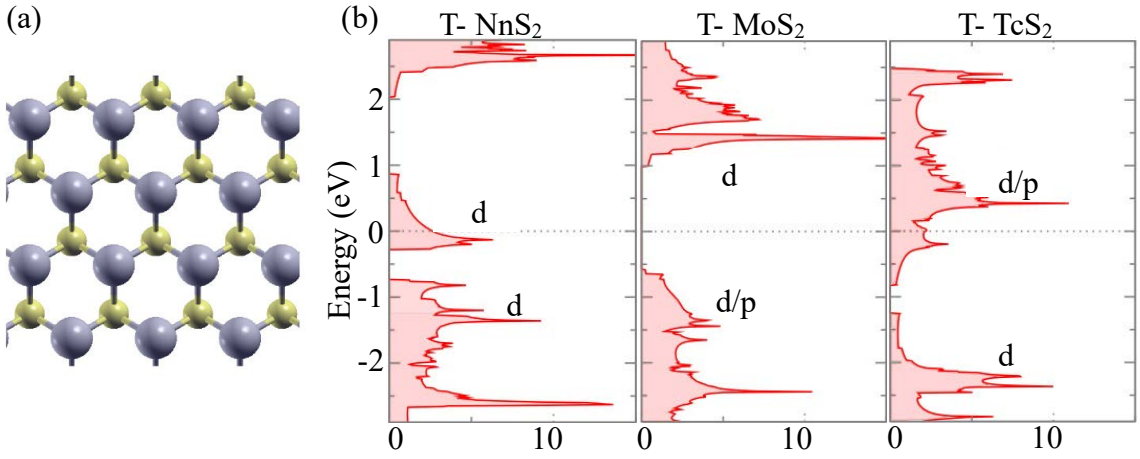

Figure 1.2. Electronic properties of TMDs: (a) a hexagonal honeycomb lattice of TMDs; **(b)** Density of states at different class of TMDs (fermi level set at zero). Adopted from [18].

1.2.2 Semiconducting group-VIB transition metal dichalcogenides

Two distinctive features are of fundamental importance in TMDs semiconductors: strong excitonic effects, and valley and spin-dependent properties. Due to the charge confinement and reduced dielectric screening of Coulomb interactions between charge carriers [19–22], the excitonic effects dominate this category of materials. The excitonic effects in STMDs determine the strength of light-matter interactions, radiative combination lifetime of the exciton (electron-hole pairs) [23], and their optoelectronics characteristics.

The second aspect of STMDs originates from their unique electronic band structure from which the valley and spin-dependent optical and electrical properties arise.

Among a wide range of TMD materials, group-VIB (M = Mo, W; X= S, Se) have been extensively explored in different structures, both monolayers and bulk. STMDs possess direct energy gaps in the near infrared to visible spectral range that potentially impact optoelectronics application. Like graphene, a monolayer of STMDs can be prepared in different ways, such as mechanical cleaving from 3D crystals, chemical vapor deposition, and molecular beam epitaxy. The extraordinary properties of these materials are associated with the remarkable quantum degree of freedom of electrons. **Figure 1.3a** shows a 2D hexagonal Brillouin zone of thin layer TMDs (BZ); the conduction band and valence band have degenerate band extrema in momentum space referred to as valleys. Bulk TMDs are found to be indirect bandgap semiconductors with conduction-band minimum and valence-band maximum located at the Q and the Γ valleys, respectively. When 2D bulk is thinned to a monolayer limit, a crossover to direct bandgap occurs, with gaps located at the K and K′ valleys [24,25]. The optical transition in monolayer STMDs is dominated by the direct transition between conduction and valence bands around K(K′). The peculiar property of STMDs is that their interband transitions at K(K′) are valley selective as σ^+ (right circularly polarized light) is coupled to the transition at K and σ^-(left circularly polarized light) is coupled to the transition at K′. Valley-dependent selection rules give rise to quantum manipulation of valley pseudospin degrees of freedom, including optical generation and detection of valley polarization and valley coherence. In a monolayer of STMDs, when a photon with suitable energy is absorbed, an electron in the

valence is promoted to the conduction band, leaving behind a hole. A hydrogen-like bound state is then formed, the electron and hole tightly bound together by the attraction of Coulomb force to form an exciton. Excitons in STMDs have binding energies on the order of 0.5 eV [20–22,26], and wave function extended over a large number of cells. Moreover, spin-orbit interaction is of critical importance in these materials, inducing spin splitting of several hundreds of meV in the valence band and a few tens of meV in the conduction band.

1.2.3 Hexagonal boron nitride

Thin layers of hexagonal boron nitride (hBN) consist of a hexagonal lattice of alternating Boron and Nitrogen atoms with a lattice constant identical to graphene; due to its close analogue of the graphite honeycomb structure, hBN is called “white graphene”. hBN has a large bandgap in the UV range, making it suitable for use as an encapsulating layer or substrate for 2D stacked devices. Encapsulating hBN devices have been shown to have smooth surfaces free of defects, disorder, charge traps, and dangling bonds. hBN serves as an exceptional substrate for graphene, providing an enhancement of its electronic quality by a factor of 10. Also, a few layers of hBN have been used as gate dielectrics and tunnel barriers due to the sustainability of its bias, which reaches ≈ 0.8V/nm [27,28].

1.3 Semiconductor TMDs and novelty of van der Waals heterostructures

Two-dimensional transition metals dichalcogenides can be stacked into a multilayer heterostructure. Because monolayer TMDs can be held together by van der Waals

interactions, designing a variety of desired heterostructures with different functionalities becomes possible. Recently, a large variety of novel TMD transfer techniques have been carried out. However, mechanical assembly is the most versatile technique for 2D heterostructure fabrication.

1.3.1 Assembly techniques

The manual assembly technique flourished in 2010 when the first graphene device on top of hBN with very high performance was demonstrated [29]. This technique provides high-quality heterostructures with clean interfaces between layers. It allows for relatively easy changes in layer sequences. The standard stacking procedure starts by isolating a micrometer-sized 2D flake on top of a thin transparent adhesive film, typically a thin polymer layer. Then the first layer can be placed down onto a chosen target of another 2D material. The transfer is repeated again with different 2D materials until the desired structure is assembled. The layers must be carefully aligned to avoid rubbing and accumulation of air bubbles. This process is typically performed under an optical microscope with micromanipulators. In Chapter 3, I will discuss the transfer function of our state-of-the-art optical microscope and the 2D heterostructure stacking procedure.

1.3.2 Optoelectronics applications

This section will illuminate recent applications of 2D TMD-based structures, especially deployments in optoelectronic devices such as photodetectors and excitonic light-emitting devices (LEDs). Operational wavelengths of TMD photodetectors are

common in conventional silicon photodetectors. However, due to their mechanical flexibility and high electronical tunability, TMDs can offer new applications; for example, flexible optoelectronics, and tunable excitonic devices. 2D TMDs devices can be operated in different operation mechanisms for photodetection because of the large energy gap. They are based on the photovoltaic effect under low dark currents, and high responsivity and slow operation speed in most devices. In contrast, graphene photodetectors operate on the basis of the weak photovoltaic, photo-thermoelectric, and bolometric effects. Graphene's photodetectors exhibit wider operational bandwidths, higher dark currents, and smaller responsivity.

Photodetection is based on the photovoltaic effect and primarily consists of two standard modes: photoconduction, in which the photoexcited carriers increase the device conductance, and photocurrent. Photoexcited carriers in photocurrent mode are converted into the current in the presence of a built-in electric field. Photodetectors based on 2D TMDs have a crucial issue: exciton dissociation by the electric field as a result of extremely strong excitonic effects. TMDs photodetectors can be in out-of-plane as well as in-plane structure, as both have demonstrated improvements in photodetectors' performance The advantage of the in-plane design is the control of material properties by electrostatic gating. In addition, photodetectors based on in-plane geometry have a significant contribution from extrinsic effects related to impurities and defect states. The first in-plane photoconduction was observed when the 2D MoS_2 transistor was illuminated with a diffraction-limited laser beam [25]. Monolayer MoS_2 transistors under a bias field of 4V μm^{-1} have reported high responsivity of approximately 880 AW^{-1} [30].

Moreover, photodetectors based on photocurrent mode are more efficient. This type of photodetector consists of a junction where a built-in electric field is created. The junction can be out-of-plane or in-plane. In general, the efficiency of in-plane junctions is limited by the difficulty of capturing excitons and the high built-in field to dissociate them. Out-of-plane junctions have superior performances. These are comprised of two different layers – one n-type, the other p-type – which are stacked vertically. In addition, their doping level can be tuned through electrostatic gates. These devices do not require exciton diffusion to the depletion region because their exposure area is large and provides efficient optical absorption.

Excitonic light-emitting devices also have optoelectronic applications. Excitonic LED devices are based on electron-hole recombination in junctions such as p-n junctions [31–33], Schottky junctions [34], and vertical tunnel junctions [35]. Emission efficiency in TMDs excitonic LEDs is expected to increase with high photoluminescence (PL) quantum yield. Furthermore, it has been demonstrated that emissions in such devices are tunable between natural excitons and charged excitons (trions) through electrostatic gates.

1.4 Basic electronic structure and optical selection rules of TMDs

1.4.1 TMDs' electronic structure

Crystal structures of 2D TMDs have a large impact on their electronic structure. Bulk TMDs are known to crystalize in different structures. Three layered structures are most well-known and intensively studied, i.e., 1T, 2H, and 3R (**Figure 1.3).** In group

VIBTMDs, 2H and 3R phases are more stable than 1T. Monolayers in 2H and 3R phases have a similar structure, but the difference lies in the stacking order of layered structures. In fact, the monolayer structure consists of three atomic planes. The top and bottom are two triangular lattice structure planes of chalcogen atoms; another triangular lattice in the middle consists of a metal atom (**Figure 1.3b).** These three atomic planes form the elementary building blocks of the 2D hexagonal lattice, with one metal atom located in the A-sublattice and two chalcogen atoms at the B-sublattice. 2H bulk crystal possesses hexagonal symmetry, with two monolayers per repeat unit and the adjacent monolayers are at 180° rotation of each other, with A site of the first layer on top of the B site of the second layer, and vice versa. The 3R phase has rhombohedral symmetry, with three layers per repeat unit in the translation of each other.

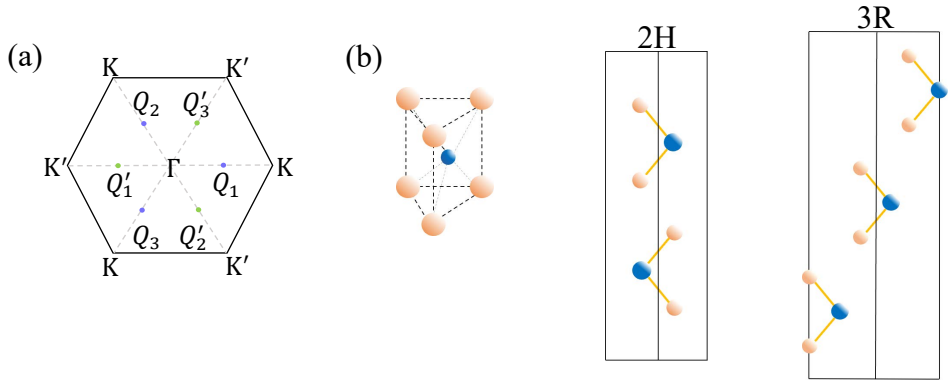

Figure 1.3. Crystal structure of TMDs: (a) Brillion zone of TMDs; **(b)** Different layered phases, 2H and 3R, in TMDs. Adopted and replotted from [36].

These 2D TMD films exfoliated from bulk crystals are primarily in the 2H stacking phase; in fact, calculations show the bilayer in 2H stacking is more stable than in 3R stacking [37]. This dissertation principally studies the 2H stacking phase structure. One critical difference between bulk crystal and monolayer in the 2H phase is symmetry. The

2H bulk has inversion symmetry, and when the thickness of the film is reduced to a monolayer the unit cell becomes half of its bulk unit cell and noninversion symmetric. Therefore, the crystal symmetry reduces from the space group D_{6h}^{4} in bulk structure to a space group D_{3h}^{1} in monolayer structure. The inversion symmetry is present in bulk and films with an even number of layers, and it is broken for a film with an odd number of layers.

Extrema points of the energy bands, sometimes referred to as critical points, play crucial roles in determining the transport and optical properties. The conduction band minimum (CBM) and the valence band maximum (VBM) in monolayer TMDs are located at the corners of the first Brillouin zone. The top valence and lowest conduction bands are the most active bands considered in 2D TMDs research. The six corners of the first BZ are related to two equivalent groups, namely K and K' valleys, where each group has three equivalent points associated with each other by reciprocal lattice vectors (**Figure 1.3a).** Extrema bands at K and K' are energetically degenerate but inequivalent and transform into each other under time-reversal operation. In addition, the conduction band has six minima at low symmetry Q points, while the valence band has a local maximum at the Γ point, Q_c, and Γ_v, respectively. These points are as crucial as K_c and K_v because they are energetically close to each other. K and Γ are high symmetry points that are invariant under the C_3 operation, which is a rotation by $2\pi/3$ around the z-axis. Like K valleys, the six Q_c valleys have two groups Q and $-Q$. Three Q valleys transform into $-Q$ through $C3$ operation, while two groups are related by time-reversal operation.

First-principles calculations show that in monolayer the four minimum bands of CB and seven maximum bands of VB are predominantly from the M-d orbitals and X-p orbitals, while other orbitals such as M-s, p and X-s have a negligible contribution. In addition, the first-principles calculations find that the band-edge states at K_c and K_v are primarily from the M- $d_{x^2-y^2}$, d_{xy}, d_{z^2} orbits with some mixture of X-p orbitals, **(Table 1.1)**. Moreover, X-p_z composition at Q_c and Γ_v has crucial importance in the crossover from

State	Majority of orbitals	Minority of orbitals
K_c	M-d_{z^2}	X-p_x, p_y
K_v	M-$d_{x^2-y^2}$, d_{xy}	X-p_x, p_y
Q_c	M-$d_{x^2-y^2}$, d_{xy}	M-d_{z^2}, X-p_x, p_y, p_z
Γ_v	M-d_{z^2}	X-p_z

Table 1.1. Orbital compositions of Bloch states at conduction and valence bands. Adopted from [37].

direct to indirect bandgap from monolayer to bulk. Large hopping occurs between adjacent layers due to a close distance between X-p_z orbitals, which changes the energy of Q_c and Γ_v [38,39].

The wave-vector group, at K and K', is C_{3h}, which is the mirror reflection of the xy plane across the metal atoms. C_3 and σ_h are generators to C_{3h}, where σ_h symmetry divides the five orbitals of M-d into two sets: even ($d_{x^2-y^2}$, d_{xy}, d_{z^2}) and odd (d_{xz}, d_{yz}). Additionally, X-p orbitals above and below the metal atom plane can be arranged in a linear superposition of odd and even σ_h symmetry.

1.4.2 Optical band gaps and the excitonic effect

The bandgap is the energy difference between CBM and VBM and can be determined by transport or optical means. The band gap as determined by transport measurements is known as the electronic gap. It's defined as the sum of energies needed to tunnel an electron and a hole into the system separately. The bandgap size as determined by transport measurement differs from the one determined by the optical means because of the excitonic effect present in the optical process. In optical measurements, the absorption of a photon stimulates an electron in the CB and leaves a hole in VB, which forms an exciton by binding through Coulomb interaction. The optical band gap is the energy required to create an exciton. The optical bandgap of monolayer TMDs can be determined from the PL measurements, and for all group VIB TMDs the band gap is in the visible frequency range.

Moreover, experiments show that substrates and dielectric environments influence the optical bandgap and change it by a few percent [25,40]. By using scanning tunneling and ARPES, the electronic bandgap can be determined. For example, monolayer MoS_2 on highly ordered pyrolytic graphite has an electronic bandgap of 2.15 eV or 2.35 eV at 77 K [41], while, on the same sample, the optical gap is 1.93 eV at 79 K.

1.4.3 Optical selection rules

One of the exciting properties of monolayer TMDs is that their two valleys couple differently with circularly polarized light. The optical transition from valence band top VB to conduction band bottom CB at *K* valley is prompted exclusively by the left circularly

polarized light. While at K' valley, the optical transition is prompted exclusively by right circularly polarized light. Such valley selectivity in monolayer TMDs arises from the difference in quantum numbers m associated with the conduction and valence bands. At K valley, the down- spin of the valence bands are assigned as m = -1/2, and m =1/2 is assigned for the up-spin. While down-spin and up-spin of conduction bands are assigned as m = -3/2 and -1/2, respectively. Hence, the interband transition from VB to CB in K valley requires absorption of left circularly polarized light (σ^-), which has an angular momentum Δm = -1. Since the K' valley is linked to K valley by time-reversal symmetry, the quantum numbers have opposite signs to the K valley. Thus, the interband transition in K' valley occurs through absorption of right-circularly polarized light (σ^+) with Δm = +1; these quantum numbers can explain the valley selectivity. Moreover, spherical symmetry in atoms allows electron orbitals to have magnetic quantum numbers m = 0, ±1, ±2, ±3, …, and the crystal lattice has a space group D_{3h}^1 that requires trigonal symmetry C_3 at the K symmetry points.

In order to get the quantum numbers of the conduction and valence band (**Table 1.2),** we consider the eigenvalue γ_α (α = c, v) of the rotation C_3 on the Bloch functions $C_3\psi_\alpha = \gamma_\alpha \psi_\alpha$, Including both components of Bloch functions: construction atomic orbitals and the plane wave as

$$\Psi_\alpha(r) = \frac{1}{\sqrt{N}} \sum_R e^{\pm iK\cdot(r+\delta)}\ d_\alpha(r - R - \delta)$$

Where R is the lattice vector, δ is the position of M atom in the unity cell, $d_c = d_{z^2}$ and $d_v = (d_{x^2-y^2} \pm i d_{xy})/\sqrt{2}$.

By using the symmetry of C_3 on the Bloch functions, we can get the eigenvalue

$$\gamma_{\alpha}^{\rho} = e^{\pm iK\cdot\left(C_3^{-1}\delta-\delta\right)}\gamma_{d_\alpha}$$

Where δ is the M atom position with respect to rotation centre ρ, which can be M, X, or the h position (the centre of the hexagon formed by M and X), and γ_{d_α} is the eigenvalue about the centre of atomic orbitals [36]. We can obtain the orbital quantum number m_l from $\gamma = \exp\left(\frac{i2\pi ml}{3}\right)$. For example, at ρ = M ($\delta = 0$) the lattice phase has zero contribution then, $\gamma_c^{Mo} = \gamma_{d_c} = 1$ and $\gamma_v^{Mo} = \gamma_{d_v} = \exp\left(\frac{\pm i2\pi}{3}\right)$. $m_l = 0$ for the conduction bands at K and K' valley, while $m_l = -1$ for the valence bands at K valley and +1 at K' valley.

	M d	X p	ρ (M)	ρ (X)	ρ (h)
CBM	d_{z^2}	$p_x - ip_y$	0	+1	-1
VBM	$d_{x^2-y^2} + id_{xy}$	$p_x + ip_y$	+1	-1	0

Table 1.2. Rotational symmetry and orbital compositions of conduction and valence bands in monolayer TMDs. Adopted from [42].

The choice of rotation centre ρ has an essential role in determining the quantum numbers associated with conduction and valence bands. However, the upward optical transition between the spin-conserving bands remains fixed, meaning Δm = -1 at K Valley and +1 at K' valley. These valley selectivity rules allow optical pumping and detection of valley polarization; consequently, circularly polarized light exclusively injects photocarriers into one valley. Valley polarization of electron-hole pairs will conform through circularly polarized luminescence. Another consequence of valley selectivity is optically generated valley coherence.

On the other hand, excitation by linearly polarized laser, which is a superposition of (σ^+) and (σ^-) polarized photons, can inject photocarriers in linear superposition at K and K'.

1.5 Electronic band structure of bilayer WSe_2

This dissertation focuses on the bilayer system, particularly bilayer WSe_2. In a homobilayer system 2H stacking is considered the most stable configuration, and the upper layer is at 180^o rotation in respect to the lower layer (**Figure 1.3b)**. Thus, the valley dependent physics in 2H stacking average to zero, as required by the rotational symmetry. However, a perpendicular electric field can break the inversion symmetry, which provides a potentially controllable way to tune the valley-dependent physics by changing the system's symmetry.

Interlayer hopping in the 2H stacking system results from the crossover from a direct bandgap in the monolayer to an indirect bandgap at the bilayer and multilayer system. By increasing the number of layers, the band extrema K_v, Γ_v, and Q_c all split. Such splitting is direct evidence of the interlayer hopping and represents the interlayer hopping strength. Different amounts of splitting occur in the different bands. Splitting at Γ_v and Q_c are much larger than K_v due to the different predominant orbitals at these bands' extrema. At K_v, the metal d orbitals dominate Bloch states, while the chalcogen p_z orbitals have nonnegligible contributions in the Bloch states at Γ_v and Q_c. The two metal planes have more significant separation in comparison to the two nearest neighbor chalcogen planes from two layers, which makes the interlayer hopping at K_v considerable weaker than at Γ_v and Q_c.

As a consequence, the energy of Γ_v is raised, and that of Q_c is lowered, while K_v and K_c do not change when the number of layers increases.

A salient feature in 2H system stacking is that the interlayer hopping at K and K' valleys quench due to spin-orbit coupling. First-principles calculations with SOC turned on show nearly identical band dispersions at K_v for mono-, bi-, tri, and quad-layers. This is because of the presence of out-of-plane spin splitting with opposite signs in the K and K' valleys, and the presence of 180° rotation of one layer in respect of the other switches the two valleys in the lower layer, but the spin remains unchanged. Hence, both the valley and layer index determine the sign of spin splitting. The spin splitting corresponds to an energy cost of the interlayer hopping. As result, the interlayer hopping is quenched when SOC is strong, especially for WX_2. At K and K' valleys, the spin index is locked to the layer index, meaning that the Bloch states are localized either in the upper or lower layers, depending on the spin.

In the remainder of this section, we mainly focus on the first-principles calculations of the band energies of bilayer WSe_2 after applying the perpendicular electric field.

1.5.1 Electric-field effect on the band energies of bilayer WSe_2

We have calculated the shift of band-edge energies and transition energies of various intervalley electron-hole pairs (with no excitonic effect) of bilayer WSe_2 under the application of an electric field (E) along the z-axis (perpendicular to the plane). The applied electric field gives rise to a perturbation term $\widehat{H}_1 = eEz$, which is included in the density-functional theory (DFT) to calculate the effect of electric field on the band structure. We

include the spin-orbit interaction and the van der Waals interaction between the two WSe_2 monolayers in our calculation.

By using reasonable lattice constants, we have calculated the band structure of bilayer WSe_2, which displays the conduction band minimum (CBM) at the Q point (near the middle point between K and Γ) and the valance band maximum (VBM) at the K point **(Figure 1.4)**. The Γ point has lower energy than the K point in the valance band. By adopting a lattice constant a = 0.3279 nm, which is close to the experimental value (a = 0.3282 nm) [43]. we can obtain a Γ-K separation of 140 meV in the valance band **(Figure 1.4a)**. which matches the Γ-K separation measured by a recent experiment of angle-resolved photoemission spectroscopy (ARPES) on a BN-supported bilayer WSe_2 sample [44]. For a slightly larger lattice constant a = 0.3313 nm, the Γ-K separation drops to 69 meV **(Figure 1.4b)** indicating that the Γ-K separation depends sensitively on the lattice constant. In all of the following calculations, we use the lattice constant a = 0.3279 nm.

We then consider the effect of a perpendicular electric field on the strained bilayer WSe_2. **Figure 1.5** displays the calculated band structure of bilayer WSe_2 under perpendicular electric fields E = 0.04, 0.08, 0.12, and 0.16 V/nm. These electric fields are the net fields seen by an electron in the material under the screening of the valence electrons. Our results show that the two-fold degenerate conduction band at Q and valence band at K split because the applied electric field breaks the inversion symmetry of bilayer WSe_2. However, the valence band at Γ remains two-fold degenerate due to the time-reversal symmetry (Kramer's degeneracy).

In our consideration below, we will focus on the conduction band at the Q point, and the valence band at the K and Γ points. We denote the conduction band with lower (higher) energy at Q as c1 (c2) and the valence band with higher (lower) energy at K as v1 (v2). **Figure 1.6** displays the calculated interband transition energies of the $Q_{c1} - K_{v1}$, $Q_{c1} - \Gamma_{v1}$, and $Q_{c2} - \Gamma_{v2}$ transitions as a function of the screened electric field. The $Q_{c1} - \Gamma_{v1}$ and $Q_{c2} - \Gamma_{v2}$ transition energies are found to split with increasing electric field. Here we have not considered the excitonic effect, which should only produce a constant energy offset with insignificant influence on the field-dependent energy shift. In **Figure 1.6**, the Q-Γ transition energies are the interband transition energies obtained by DFT, whereas the Q-K transition energy is shifted to match the experimental separation between the QΓ and QK exciton emission lines at zero field in **Figure 4.4d.**

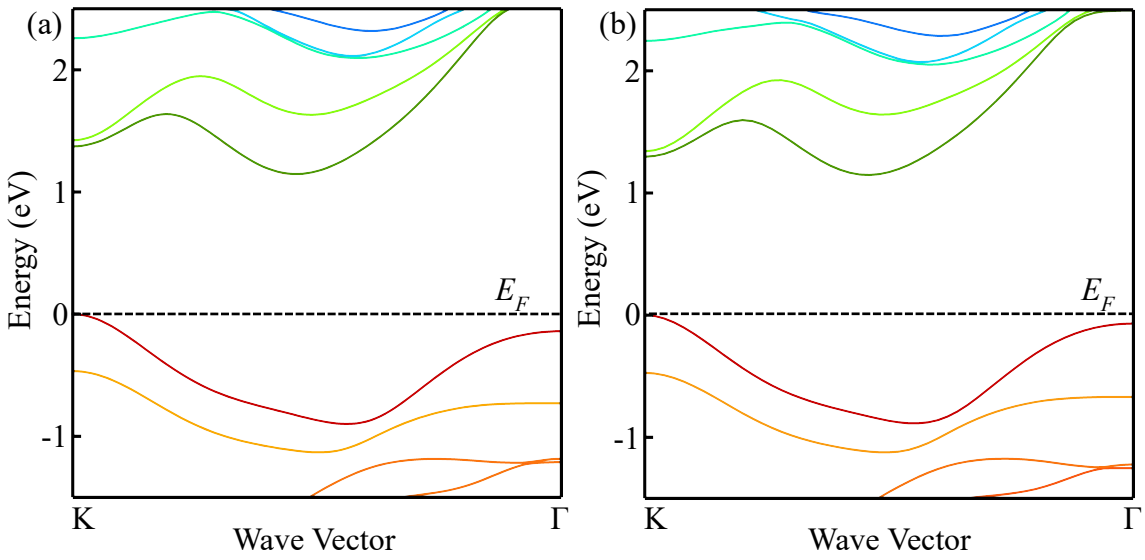

Figure 1.4. Theoretical band structure of bilayer WSe_2 with two different lattice constants: (a) a = 0.3279 nm, **(b)** a = 0.3313 nm, calculated by using the WIEN2K package with GGA. The electric field is zero.

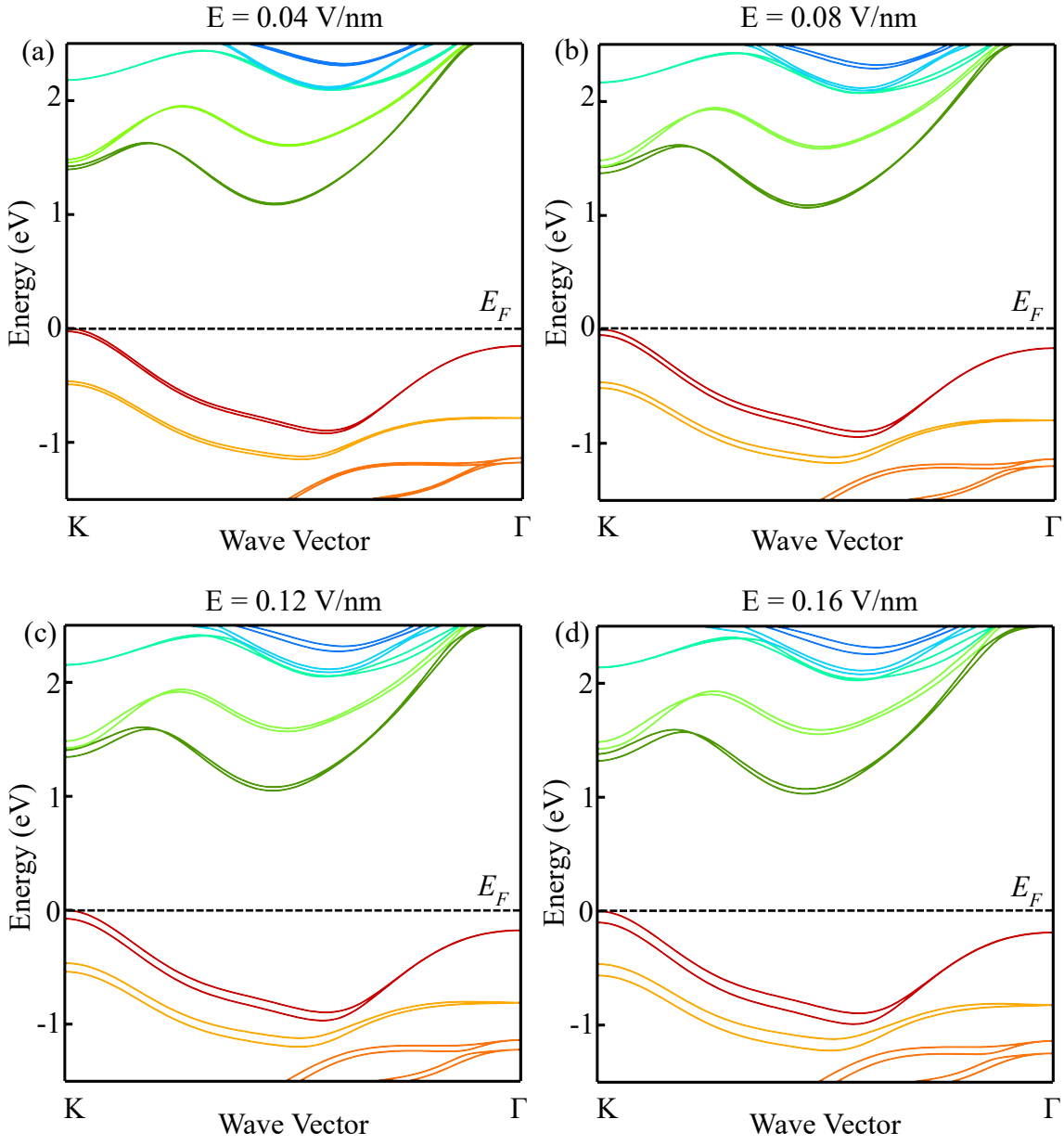

Figure 1.5. Band structure of bilayer WSe_2 with lattice constant, a = 0.3279 nm calculated using WIEN2k under four different vertical electric fields: (a) E = 0.04V/nm, **(b)** E = 0.08 V/nm, **(c)** E = 0.12 V/nm, and **(d)** E = 0.16 V/nm.

We have used two different approaches to calculate the band energy shift due to the electric field. In the first approach, we carry out a self-consistent calculation, which considers the response of valence electrons and the atomic relaxation under an external electric field (i.e. the screening effect); we obtain the band energy shift as a function of the external electric field. In the second approach, we carry out a non-self-consistent calculation, in which the applied electric field is taken as the net field after all the screening effects. Afterward, we compare the result of the two calculations and find that their electric-field dependence is off by a ratio of 5.51; this ratio is interpreted as the dielectric constant of bilayer WSe_2 (i.e., ε_{2L} = 5.51). **Figure 1.6** shows the calculated transition energy as a function of screened electric field for both calculations (solid and dashed lines). They appear to match each other well after we use the dielectric constant ε_{2L} = 5.51 to convert the applied field into the screened field in the self-consistent result.

We have used the self-consistent results to compare with our experimental data in **Figure 4.4d**. We find decent agreement on the field-dependent energy shift between experiment and theory. We note that the absolute transition energies in our calculation differ from the experimental emission energy because DFT cannot predict the band gap accurately and we have not considered the excitonic effect. But such deviation should have no significant influence on the field-dependent energy shift. Therefore, in our comparison, we shift the energies of the QΓ and QK excitons to match the experimental energies and focus our comparison on the field-dependent shift of the transition energy.

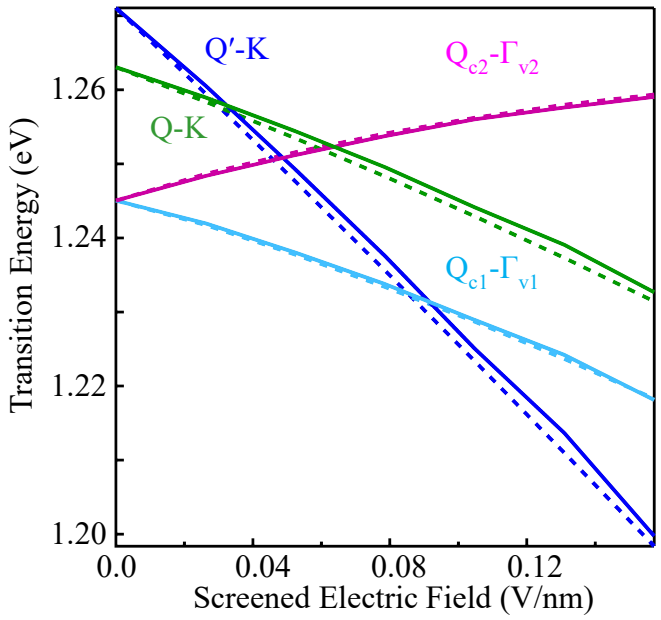

Figure 1.6. Calculated interband transition energy for the $Q_{c1} - K_{v1}$, $Q_{c1} - \Gamma_{v1}$, and $Q_{c2} - \Gamma_{v2}$ transitions as a function of screened electric field. The solid (dashed) curves are results of self-consistent (non-self-consistent) calculation as described in the text. Here the Q-Γ transition energies are the interband transition energies obtained by DFT, whereas the Q-K transition energy is shifted to match the experimental separation between the QΓ and QK excitons in Fig. 2d. Here we also show the Q'-K transition energy, offset artificially upward to illustrate its crossing with the Q-K transition energy.

In **Figure 1.6**, we also show the Stark shift of the Q'-K transition, which differs from the Stark shift of the Q-K transition (Q' is the time-reversal point of Q). The electron states at Q and Q' are energy-degenerate with opposite spins. Fig. 4.5a-b in Chapter4 show the calculated charge density of the Q electrons at the two split conduction bands (c2 and c1 bands) with spin up and down, respectively. The time-reversal states at the Q' electrons have the same density distribution but opposite spin. As optical transitions occur between bands with the same spin, the Q-K transition occurs between the upper split conduction

band and the v1 band, whereas the Q'-K transition occurs between the lower split conduction band and the v1 band. As the upper and lower split conduction bands have opposite z-dependent charge density, the Q and Q' electrons have opposite dipole moment. While the Q electron distributes more heavily on the same layer as the K hole, the Q' electrons distribute more heavily on the opposite layer from the K hole (**Figure 4.5**). As a result, the Q'K exciton has a larger vertical dipole moment and hence steeper Stark shift than the QK exciton. In addition, due to its larger interlayer electron-hole separation, the Q'K exciton has a lower binding energy than the QK exciton, leading to a slightly higher energy of the Q'-K transition at zero electric field. By combining its higher zero-field energy and steeper Stark redshift, the Q'-K transition energy is predicted to cross the Q-K transition energy at increasing electric field (**Figure 1.6**).

In **Figure 4.4d** of Chapter4, we compare the experimental data with both the Q'K and QK Stark shifts; each of them is offset separately to match the experimental energy. The experimental X_{QK} Stark shift is found to lie between the QK and Q'K Stark shifts. It suggests that both QK and Q'K transitions are involved in the X_{QK} Stark shift. In particular, the experimental X_{QK} shift shows a slight kink at E ~ 0.05 V/nm, with steeper shift at higher field than lower field. This suggests the crossing behavior between the Q-K and Q'-K transitions. It is likely that the Q'-K transition takes over the PL when its energy becomes lower than the Q-K energy at higher field. Further research, such as high-sensitivity optical absorption experiment, is merited to clarify this issue.

1.6 Electron-hole pairs in 2D transition metal dichalcogenides

Under photoexcitation, an electron promoted from the filled valence band to the empty conduction band leaves an empty electron state in the valence band. These are bound together by Coulomb interaction; such a bound quasiparticle is called an exciton. Excitons in monolayer TMDs have two distinguishable properties. First, strong spatial overlap between electron and hole in the perpendicular direction to the plane due to quantum confinement. Second, the absence of dielectric screening allows for an electric field between electrons and holes to penetrate beyond the material. The above explains the significant enhancement in Coulomb attraction and results in the considerable excitonic binding energies. The Coulomb electron-hole interaction has direct and exchange contributions, which include both long-range and short-range coupling. The long-range comprises the Coulomb interaction exerted at interparticle distances in real space larger than the interatomic bond length. Conversely, the short-range effect arises from the overlap of the electron and hole wave functions at a scale within one or several unit cells.

Exciton binding energy E_B can be determined directly by experiment. In order to measure the binding energy, we need to identify the absolute energy position of the exciton resonance E_x (optical gap) and the free particle bandgap E_g (electronic gap), where $E_B = E_g - E_x$.

The transition energy $E_X^{(n=1)}$ in monolayer TMDs can be obtained by optical means, where exciton resonance appears as a pronounced peak at a photon energy corresponding to $E_X^{(n=1)}$ in PL, photoluminescence excitation (PLE), optical absorption,

reflectance, and photocurrent (PC). In contrast, the free-particle bandgap requires precise measurement to be determined.

A large exciton binding energy, approximately estimated at hundreds of meV in monolayer TMDs, contributes to the difference between the measured free-particle and optical band gaps. In monolayer WX_2, the exciton binding energy is in the range of 0.3-0.7eV, inferred from spectral features in two-photon measurements, which probes excited excitonic states. In addition, the energy difference between neutral exciton and charged exciton is consistent with the binding energy of exciton and has been measured in the range of 20-40 meV [45]. All of the above manifest in exceptionally strong Coulomb interaction, which is attributed to the large effective masses of both electrons and holes and to the reduced dielectric screening in the limit of 2D. When electron-hole separation increases, the overall screening gets suppressed due to the significant electric field penetration outside the material. Such suppression results in an obvious deviation from the usual hydrogenic series of exciton energy levels.

In the formation of exciton in semiconductors, two primary processes are considered:

(i) direct hot exciton photogeneration with simultaneous emission of phonons, or (ii) biomolecular exciton that contains direct binding of electrons and holes. In monolayer TMDs, when the excitation energy is near-resonant, the exciton formation process involves simultaneous phonon emissions and can yield the formation of intravalley or intervalley excitons.

Chapter 2

Device Fabrication

2.1 Introduction

Since the successful isolation of graphene in 2004 [46], the applications of two-dimensional materials have been a great attraction to most researchers. In fact, the rapid improvements in the quality of two-dimensional (2D) devices fabrication have had a significant effect on the measurement and deeper understanding of these physical phenomena. Thin layers of 2D materials can be prepared via mechanical exfoliation, chemical vapor deposition, and molecule beam epitaxy. Since 2010, 2D material-based devices have rapidly enhanced both in quality and complexity of the devices' geometry. Most interestingly, the encapsulation of monolayer TMDs with hexagonal boron nitride, a layered 2D material with a bandgap in the UV range of the optical spectrum, has been shown to reduce defect formations and help to minimize disorders from surface roughness and charged dopants. As a result, research reported very narrow exciton linewidth [2,3]. In addition, using graphene as the contact between the electrodes and 2D materials has reduced contact resistance (R_c). In the work presented here we use only mechanical exfoliation tape-based production of atomically thin layers. We have produced high-quality devices encapsulated with clean hBN layers, using thin layers of graphite as contacts and gates. We open this chapter by introducing the mechanical exfoliation 'tape-based' production of monolayer 2D materials, then explicitly illustrate the mechanical transfer of

2D layers into atomically stack heterostructures. Finally, we briefly present the techniques for device fabrication.

2.2 Thin Layer exfoliation of 2D materials

We fabricate dual gated 2L WSe_2 heterostructures using the mechanical exfoliation tape-based method with WSe_2 bulk crystal on a suitable substrate. There are several kinds of substrate that can be used to deposit 2D flakes: SiO_2/Si, fused silica, and sapphire, among others. SiO_2/Si substrates are the most widely used. The coating layer of SiO_2 can optimize the contrast for a monolayer of TMDs under optical microscope investigation [49]. In addition, SiO_2/Si substrates are most compatible with microelectronics standers [50]. We have used two different types of tape to produce 2D flakes. Scotch tape, which is known to have strong adhesion, and silicone-free adhesive plastic film (blue tape), which is less adhesive than scotch tape. We use scotch tape to exfoliate TMDs and blue tape for graphite and hBN exfoliation.

There are several ways to exfoliate 2D materials using both types of tapes; here we review the most common procedure. In the case of TMDs, we start by taking a piece of the crystal and placing it gently at the centre of the tape, as shown in **Figure 2.1a.** Then, we lay one side of the tape on top of the crystal (**Figure 2.1b)**. We peel the tape off and repeat this step until we have a uniform distribution of flakes over the entire tape (**Figure 2.1c)**. Notice that for TMDs, one needs to take care not to overlap areas of an exfoliated flake when repeating the exfoliation process. Overlapping spots with exfoliated flakes would tear the flakes off and produce very tiny flakes. Then, we use a clean-cut SiO_2/Si wafer to

place them onto the tape. We cover the tape with SiO_2/Si wafers, and use glass slides to tape SiO_2/Si wafers down onto the tape of exfoliation. Thus, the sequence will be, from bottom to top: glass slide, Si wafers, and scotch tape. After that, the glass slide is heated at 60 - 70 ^{0}C for about 5 minutes **(Figure 2.1d)**. In the final step, we peel the scotch tape from the SiO_2/Si wafers, gently and very slowly to avoid bubbles. This conventional mechanical exfoliation randomly distributes different thicknesses of flakes over a large SiO_2/Si substrate surface. We find that heating the scotch tap enhances the production rate of monolayer TMDs. Optical images of monolayer and bilayer TMDs are shown in **Figure 2.2a and b**, respectively.

For graphene and hBN exfoliation, we perform a similar procedure to the above. However, we use blue tape instead of scotch tape, and omit the heating step. For ultra-clean hBN flakes, we perform the exfoliation and peeling very gently, trying not to exert any pressure on the surface of the tape after placing the SiO_2/Si. Our high-quality devices rely on using very clean hBN. We investigate the flakes under a dark field optical microscope. The dark-field microscopy technique collects only light scattered at angles larger than the central cone of the microscope objective. Thus, it provides suitable identification of surface roughness in a flake due to wrinkles, surface adsorbs, and inhomogeneities in the 2D surface. A comparison between bright field and darkfield imaging is shown in **Figure 2.3**.

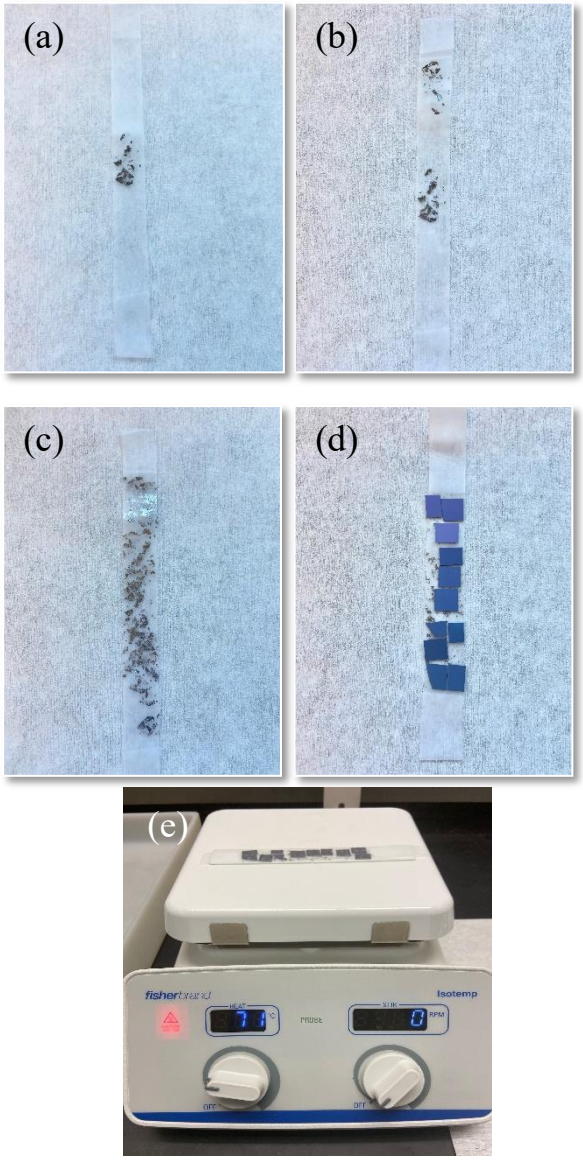

Figure 2.1. Mechanical exfoliation, 'tape-based': (a-d) Sequence of tap exfoliation procedure; **(e)** heating process before peeling tape off the substrate.

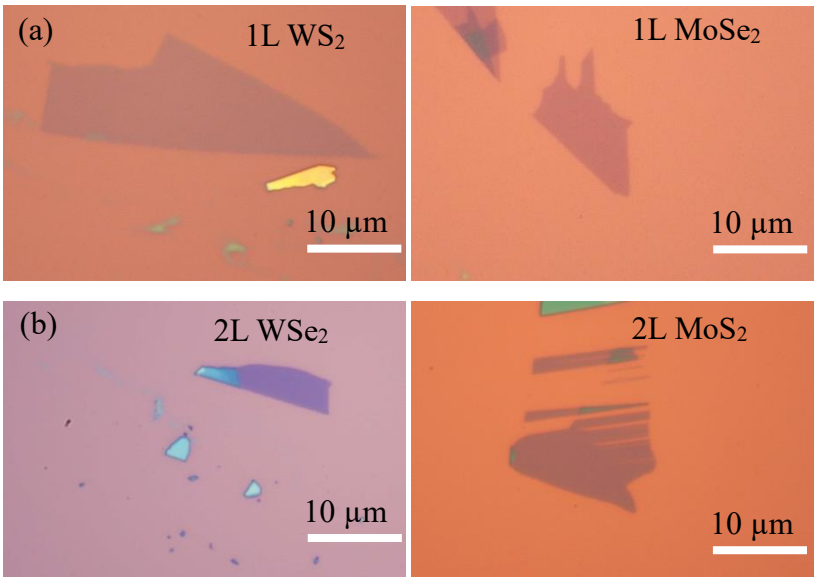

Figure 2.2. Optical images of atomically thin layers of TMDs: (a) Monolayer of WS_2 and $MoSe_2$; **(b)** Bilayer of WSe_2 and MoS_2.

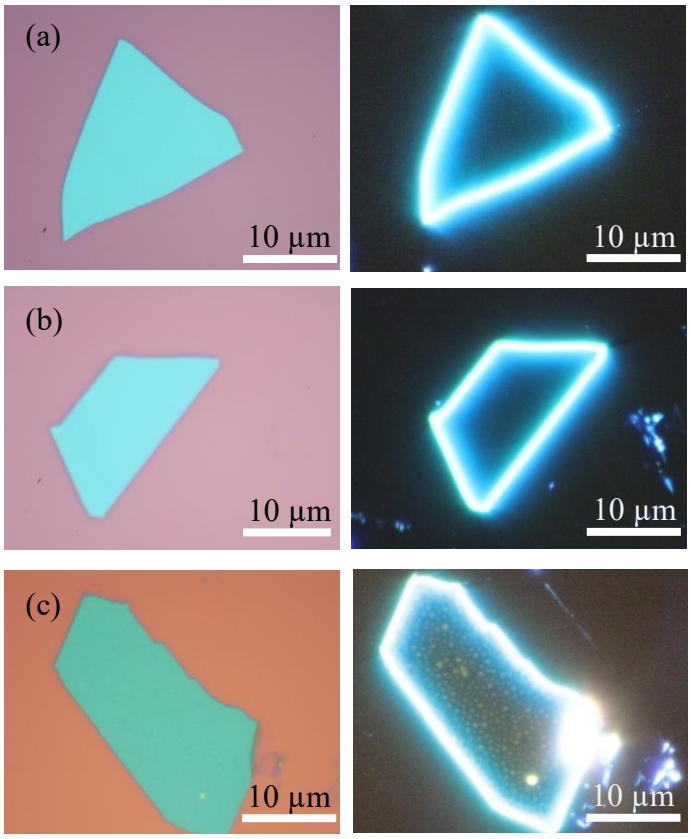

Figure 2.3. Optical Images of a few layers hBN in bright-field and dark-field modes: (a) and **(b)** are clean hBN flakes with bubbles free; **(c)** hBN flake with bubbles and adsorbs into surface

2.3 Transfer of 2D flakes into stacking atomic layers

2.3.1 High standard optical transfer microscope

We fabricate our high-quality devices using a state-of-the-art transfer optical microscope, in this section we discuss the design of our microscope. **Figure 2.4** shows a photograph and a corresponding schematic illustration. The optical transfer microscope consists of three major parts: Imaging system, Base stage, and Transfer arm stage. Our imaging system is composed of an optical microscope assembly with an interchangeable long-working distance objective lens (50x and 10x magnification) that allows imaging of the plane parallel to the Base surface. The Si/SiO_2 onto which the desired 2D flakes have been exfoliated is placed on top of the Base's surface. We fix the substrate onto the surface via vacuum connection, where the vacuum line is connected through a small hole in the centre of the Base surface. Two DC resistive cartridge heaters and a thermocouple are embedded within the Base and sit close to the top of the surface. Both heaters and a thermocouple are coupled to a DC voltage source with a high-power and a temperature PID controller. Using the PID controller helps regulate the DC voltage output to an input target temperature and ensures sufficiently slow heating that the surface has a uniform temperature. We mount the Base on a ceramic standoff to thermally isolate it from the rest of the Transfer assembly. The entire Base stage can be rotated 360° and translated into the x, y plane. The Transfer arm locates in between the imaging system and the Base stage. The Transfer arm holds the polymer stamp and must be translucent so that the Base imaging through the Transfer arm is precise. The material conventionally used for the transfer arm is a standard glass microscope slide. However, we instead use a thin aluminum Transfer

arm with a small hole covered by a microscope coverslip. Since the coverslip is about 10 times lighter than a glass slide, the microscope coverslip significantly reduces the aberrations present when using a standard glass microscope slide. The Transfer arm is placed and held together with the entire Transfer arm assembly by vacuum. To allow precise alignment between the surface of the polymer stamp and the surface of 2D flakes in the sample on top of the Base stage, the Transfer arm assembly has a 3D linear translation stage and tip-tilt stage. The entire assembly allows ≈ 1μm x, y alignment, z-direction translation to bring the stamp into contact with the Base, rotational alignment, and in the plane controllable tilt of the arm relative to the Base surface.

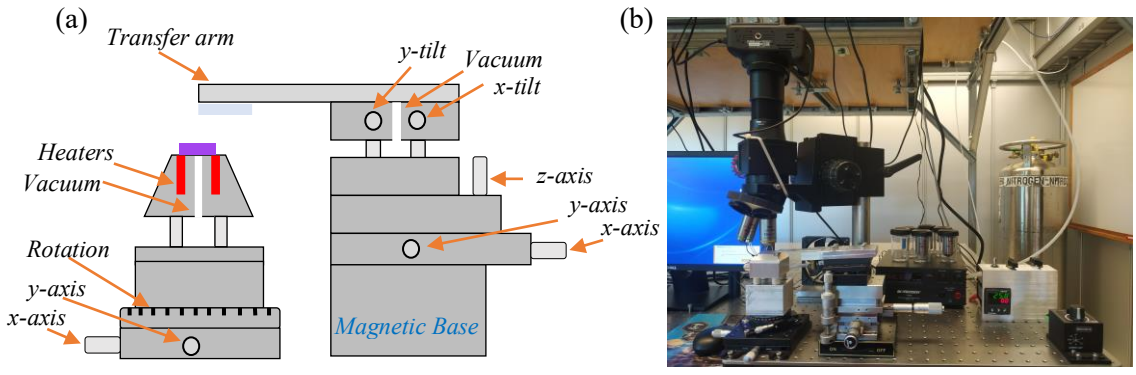

Figure 2.4. Photographic image of transfer microscope and corresponding schematic illustration.

2.3.2 Polymer film preparation

Van der Waal material transfer techniques have significantly improved over last decade. Here I will review the dry transfer method we developed and used to assemble the heterostructure measured in this dissertation. The first step is fabricating the polymer stamp, which we use to pick up and manipulate the 2D flakes. Usually, the polymer stamp

consists of two layers: the polymer base that must be of viscoelastic material e.g., polydimethylsiloxane (PDMS), and the top layer of poly (bisphenol A carbonate) (PC), a translucent and thermoplastic polymer that is soluble in a chloroform solvent. Another common stamp material is polypropylene carbonate (PPC) which is soluble in acetone [51]. PC is found to be perfect in most transfer techniques and requires high temperature throughout the process.

On the other hand, the PPC is more suitable for heat-sensitive materials since it requires a lower temperature than PC. A thin film of PC is prepared by dissolving poly (Bisphenol A carbonate) (Sigma Aldrich analytical standard 181641) in chloroform, 6% solution by weight. Then, we use drops of the PC solution to cover the center of a cleaned standard glass slide. Another glass slide is placed over the previous one and quickly removed with minimal downward pressure so that a homogenous PC film remains on the bottom. The PC film dries for ~10 minutes, then we use a razor blade to cut the film and stack it with a commercial PDMS layer. The final polymer stamp comprises a fresh cleaned PDMS as a bottom layer stacking with a small square PC film on top. Lastly, we place the entire stamp onto the Transfer arm to be used.

2.3.3 Dry transfer procedure and van der Waals assembly

We fabricate and use dual gated devices with about six 2D layers in a stack for the work presented in this dissertation. In this section I will describe only the first, second, and final dry transfer steps. However, I will discuss the conditions of the procedure in particular detail. The first flake in our heterostructure is a few layers of graphite as the top gate.

Starting at room temperature, the substrate containing a few layers of graphite is affixed to the Base stage and the flake to be transferred is centered in the microscope field view.

Then when commencing the heating and cooling process, the Base is heated to a temperature just below the glass transition temperature of the PC polymer layer (≈150 ^{O}C for PC). The transfer arm is then lowered until very close to the substrate surface. During and after the heating process a thermal expansion occurs at the Base, and the flake may need to be repositioned. We then lower the focal plane of the microspore and bring it to a height at half distance between the flake and the surface of the PC stamp. Then, we adjust the distance of the transfer stamp until it intersects with the current focal plane. This entire process is then repeated until the transfer stamp is directly above the flake but not touching the surface.

Next, the PC stamp is slowly brought into contact with the substrate. Here, the engagement may be accomplished either by fine mechanical control or via the thermal expansion of the Base. The former is used mainly for isolating monolayer TMDs that are attached with bulk flake, i.e. where the initial temperature is to be fixed and relatively high before the engagement of the PC. The latter is accomplished by using a relatively low initial temperature of the base to allow thermal expansion without exceeding 150 ^{O}C, PC polymer glass transition temperature. In both cases, we attempt to allow PC polymer to cover only the area around the flake of interest and minimize contact elsewhere. In this way, we ensure good contact with the flake and a reduced total adhesion between the PC stamp and the Si/SiO_2 substrate. In addition, the initial contact between the PC stamp and the surface is

aimed to be along a single line, this is accomplished by tilting the transfer arm by $\approx 3^{o}$ relative to the Base. As the PC stamp is brought in touch with the substrate, the contact area will expand linearly and smoothly along a single direction. This also suppresses the accumulation of bubbles between interfaces. While in contact with the stamp, we start the cooling process by reducing the base temperature below 150 ^{o}C. Then, the PC stamp with attached flakes is lifted from the substrate via the Base's thermal compression. It is essential to perform the above process as smoothly and precisely as possible to minimize mechanical stress exerted on the flakes. Here we note that using a few layers BN for the first pick up, which is known to have strong vdW interaction with other 2D materials, enhances the success rate of pick-up and the functionality of the devices.

Subsequent 2D flakes are transferred by a similar procedure. However, we set the Base temperature to be lower than the first pick-up. The first pick-up relies only on adhesion to the PC polymer stamp, while pick-up of subsequent 2D flakes depends primarily on the interaction with the previous layer rather than the polymer. The heating process described in step one is repeated for the following flakes. However, an additional step of layer alignment is needed to ensure a perfectly aligned heterostructure. We repeatedly adjust the focal plane between the PC stamp and the flake's surface while the stamp is lowered to the substrate.

Finally, after all layers have been perfectly aligned and sequentially picked up in a stack, the heterostructure assembly is complete but still attached to the polymer stamp. Then, we carefully release the entire heterostructure onto a clean substrate. In contrast to

the first step, we maximize the contact area between the stamp and the SiO_2/ Si surface for the final release. In addition, the Base is heated to a temperature above the glass transition temperature to increase the adhesion between the polymer and substrate. Also, the transfer arm is lifted via fine mechanical control. Due to high temperature, the PC polymer adheres more strongly to Si/SiO_2 than PDMS, thus separating the transfer stamp and releasing the polymer and the heterostructure onto the substrate. The substrate is immersed in chloroform solvent to dissolve PC polymer and to leave behind the heterostructure.

2.4 Electron Beam Lithography and Metal Deposition

The second stage of device fabrication after completing the layers stacking is the electrical contact pattern. This is accomplished by using electron beam lithography or focus ion-beam lithography. First, we coat the samples with electron/ion-sensitive resist film (MMA/PMMA), then a focused beam of electrons or ions exposes areas of a design pattern with ultra-high resolution. Next, a thin layer of metals (5 nm Ti/ 100 nm Au) is deposited onto the e-beam exposed area via a high vacuum electron beam evaporator (**Figure 2.5).**

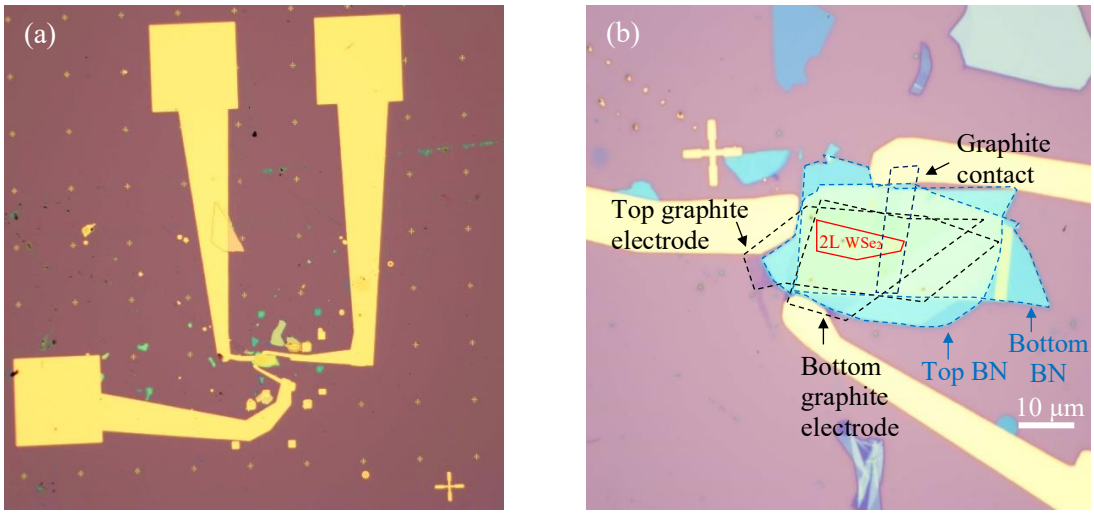

Figure 2.5. Optical images of hBN encapsulated bilayer WSe_2 dual gating device used for the experiments in Chapter 4: (a) 10x magnification showing entire device with gold contacts deposited via electron beam lithography and electron beam evaporation; **(b)** 100x magnification.

Chapter 3

Optical studies of transition metal dichalcogenides

3.1 Introduction

This chapter provides a brief introduction to optical spectroscopy of layered transition metal dichalcogenides (TMDs) as a powerful, non-invasive tool to investigate electronic band structure and crystal quality. Optical spectroscopy provides intrinsic information about materials, such as bandgap, exciton binding energy, absorption strength, lattice structure, and interlayer coupling. Applications in photonics and optoelectronics attest to the role of optical spectroscopy in understanding light matter-interaction on the atomic monolayer scale. Thus, optical spectroscopy represents one of the primary research directions of layered semiconductor TMDs. Many accessible optical techniques exist to explore the optical properties of materials, such as Raman spectroscopy, PL spectroscopy, and differential reflectance spectroscopy. Raman spectroscopy gives access to lattice structure by probing the vibrational and rotational modes in a system. Because the vibrational modes of crystalline lattice (phonon) are sensitive to layers number and structure phase, Raman studies have become a tool to determine sample thicknesses of exfoliated TMDs. PL spectroscopy probes the population of electronics states on the atomic scale to reveal information about emission energy and allow the optical transition of materials after photon absorption. This chapter presents Raman spectroscopy and discusses certain factors that can influence Raman vibrational modes in TMDs. It then explains PL

spectroscopy and presents monolayer and bilayer WSe_2 emission spectrums. Finally, the chapter discusses differential spectroscopy as a further optical technique.

3.2 Raman Spectroscopy

Characterizing stacked TMD layers is challenging due to the varying degrees of freedom exhibited by stacks. TMD stacks have a rotational and translation freedom with reference to an axis either perpendicular or along a 2D plane because the stack is not generally epitaxial or unique. In addition, unlike the outermost layer, the physical properties of inner constituent layers in 2D stacks are not selectively accessible.

Raman spectroscopy is one of the most powerful 2D material characterization tools. It provides a quick, non-destructive analysis technique that details information about chemical structure. In principle, Raman spectroscopy is based on the interaction of light with the crystal lattice and chemical bonds within a material. Raman measurements probe the lattice vibration modes within the crystal.

Raman is a macroscopic technique that involves an inelastic scattering of incident light in a material [52]. This inelastic scattering can occur in two ways. When the energy of the scattered light decreases by exciting a phonon (an elementary excitation of vibration motion in solid material), this situation is called Stokes scattering. The other mechanism is anti-Stokes scattering, where the energy of scattered light increases by absorbing a phonon, **Figure 3.1.**

Raman spectra measure the intensity of the scattered light as a function of the energy shift from the incident light, known as the Raman shift. The differences in energy between

the incident and scattered radiation depend on the molecule polarization and fall with the electromagnetic spectrum's infrared region. Thus, the scattered radiation has a quantized frequency due to the interaction of the molecule's vibrational level. The accuracy of Raman measurements is 1 cm^{-1}, or approximately 0.1meV; this scale is sufficient to probe the interlayer interaction. Raman spectroscopy and infrared absorption spectroscopy are complementary techniques for structure determination, but have different selection rules.

Various parameters influence TMDs Raman spectra, including the structural phase, number of layers, laser excitation energy, polarization, and phase transition. This section will discuss the first three parameters, which are most relevant to the dissertation [52] and present Raman spectra for WSe_2, the focus material for this dissertation.

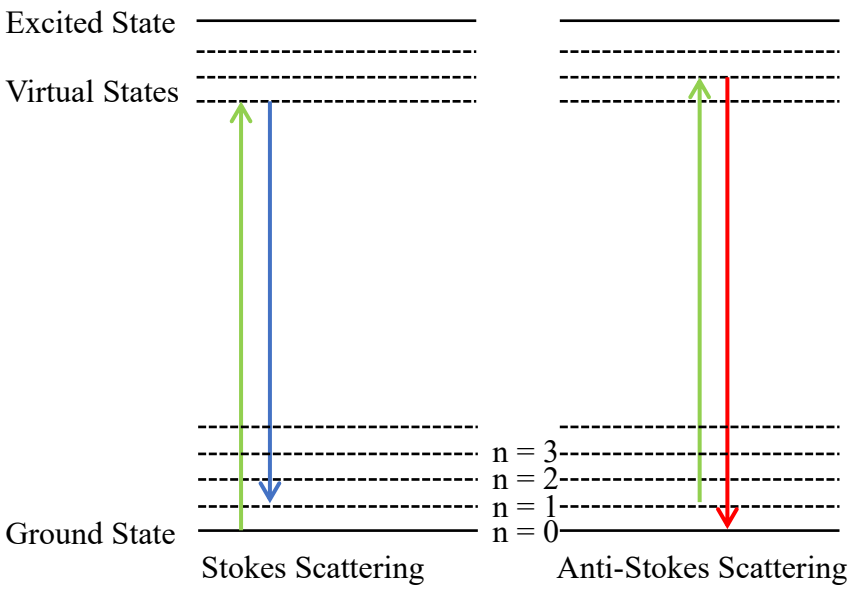

Figure 3.1. Stokes and anti-Stokes Raman Scattering.

3.2.1 Structure phase and different symmetries in TMDs

Among many TMDs materials with different crystal structures, Bulk 2H-MoS_2, WS_2, $MoSe_2$, WSe_2 have high symmetry with point group D_{6h}. When the bulk is thinned to a few layers, symmetry changes as a function of the number of the layers. For example, for its bulk structure, 2H-MoS_2 has space group D_{6h}, a non-symmorphic space group. However, the point of group gets reduced to D_{3h} and D_{3d} for odd or even number of layers, respectively. Further, the symmetry of the structure is influenced when the phase changes from 2H to 1T. Layered TMDs can be in three different structures: 2H, 3R, and 1T, as shown in **Figure 3.2(a)**, illustrating three different types. **Figure 3.2(b)** shows the 1T′ phase structure under particular conditions; it exhibits a lattice reconstruction from the 1T phase structure to lower symmetry and a more stable 1T′ structure, such as in $MoTe_2$ [53]. TMDs such as MoS_2, WS_2, $MoSe_2$, WSe_2 with point group D_{6h} are semiconductors in their 2H phase and more stable energetically than in their 1T and 1T′ phases.

There are two distinct categories of Raman vibrational modes in all layered materials. One, the intralayer Raman mode, occurs within layers and appears typically in the high-frequency region of the Raman spectra. The other corresponds to interlayer Raman mode which involves the relative motion of the layers and locates in the low-frequency region ($<100cm^{-1}$).

The number of Raman-active modes is related to the irreducible representation of the point groups with their two terms, quadratic (such as xy, $x^2 - y^2$) or linear (such as x, y, z), respectively. The bulk STMDs belonging to D_{6h} have four Raman-active and low inactive modes representing two different vibrational modes [54], shown in **Figure 3.3**

Three modes (E_{1g}, E_{2g}^{1}, E_{2g}^{2}) are in-plane and one out-of-plane (A_{1g}). In E_{1g} vibrational mode, two X atoms oscillate in opposite phases parallel to the atomic plane with a fixed M atom at the centre, where MX_2 (M = Mo, W, and X = Se, S). In $E_{2g}^{1}\left(E_{2g}^{2}\right)$ vibrational mode, two in-phase X atoms oscillate opposite (in a similar direction) to an M atom at each layer and the two layers oscillate laterally opposite to one another, while, in A_{1g} mode, X atoms oscillate in opposite phase, out of plane with respect to M atoms. TMD systems with an odd number of layers (L=1,3, 5,..) possess a D_{3h} point group, which has a centre of inversion and out-of-plane Raman-active modes corresponding to $A_1^{'}$ irreducible representation. TMD systems with an even number layer (L=2,4,6,..) belong to D_{3d} point group, which has a centre of inversion and out-of-plane Raman-active modes belonging to A_{1g} irreducible representation.

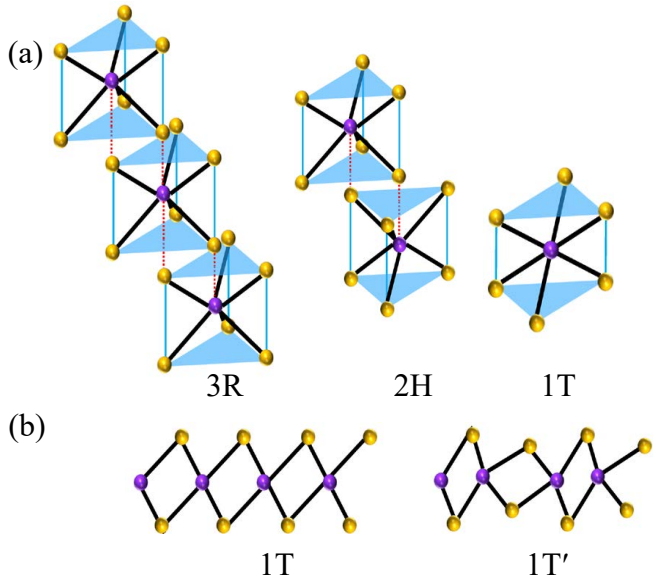

Figure 3.2. Different structures of 2D TMDs: **(a)** 3R, 2H, and 1T structure phases of TMDs; **(b)** top view of 1T and 1T′ phases. Adopted from (1).

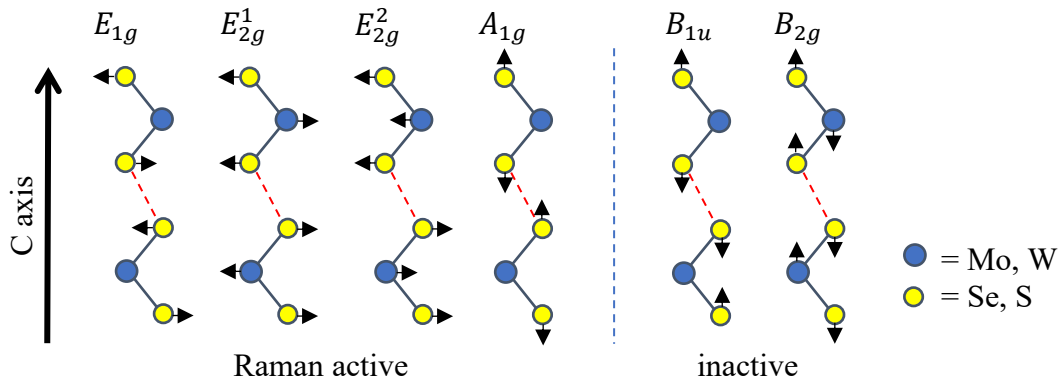

Figure 3.3. Raman-active and inactive vibrational modes. Adopted from (3).

3.2.2 Number of layer dependences

The Intralayer Raman vibrational modes with high frequency can be used to determine the number of layers *N* for few-layer TMDs. The in-plane vibration mode E_{2g} and out-of-plane A_{1g} exhibit red and blue shifts, respectively, with the increasing number of layers *N* for TMD. The experimental Raman spectrum of monolayer WSe_2 exhibits the presence of perpendicular vibrational mode $A_1^{'}$ at ~ 263 cm^{-1} and the parallel vibrational mode $E^{'}$ at ~ 250 cm^{-1}, **as shown in Figure 3.4a**. In the case of bilayer WSe_2, we report three Raman-active vibrations; the first two modes are E_g at ~ 251cm^{-1} and A_{1g} at ~ 260 cm^{-1} **(Figure 3.4b)**. The Raman-active mode at 308 cm^{-1} involves selenide and tungsten atoms' vibration and belongs to A_{1g} irreducible representations. This Raman mode is reported in the literature and proposed to be labeled as A^2_{1g} [55]. The differences between the two Raman modes are within 1 cm^{-1}, with the additional one-layer low-frequency interlayer Raman modes much more sensitive to the number of layers *N* than the high-frequency modes. Moreover, the number of Raman-active modes can be changed as

well with *N* number of layers. In principle, increasing *N* in a few layers of TMD increases the number of vibrational possibilities, enabling more interlayer, shear modes, and breathing modes to occur, whereas, for bulk TMDs, one interlayer shear mod and one interlayer breathing mode dominate the Raman spectrum.

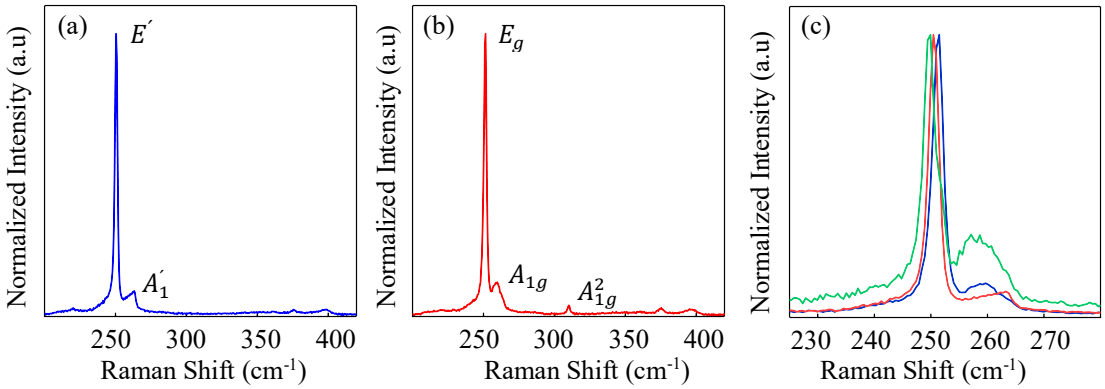

Figure 3.4. Raman spectra in few layer WSe_2: (a) monolayer WSe_2; **(b)** bilayer WSe_2; **(c)** monolayer, bilayer, bulk WSe_2 Raman spectrum.

3.2.3 Excitation-photon-energy dependence

The frequencies and intensities of the Raman modes of TMDs are strongly affected by the laser excitation energy. The intensity of specific Raman modes can be significantly enhanced when the laser energy resonances with the exciton energy. For example, a monolayer WSe_2 has a bright exciton with the lowest energy exciton state at 1.65eV at room temperature. However, a laser with 633 nm (1.96 eV) induces stronger Raman intensity modes than a 532 nm (2.33 eV) laser, which is associated with the resonance Raman effect.

3.3 Photoluminescence (PL) spectroscopy

Luminescence experiments are powerful techniques, and they are commonly used for studying the macroscopic optical properties of 2D materials and microscopic electronic excitation. PL measurements evaluate crystal quality (presence of defects) and give details about the behaviour of optoelectronics devices. PL is an electromagnetic emission of photons due to the radiative recombination of electron-hole pairs (excitons) by external excitation. Different methods can be used to generate an excited state in a material. PL and electroluminescence are widely used to study the intrinsic and extrinsic transitions. In electroluminescence, electrons are injected electrically into a material, where conversion of electrical energy into non-thermal emitted light occurs. By contrast, in PL the generation of excited electrons relies on light absorption, with energy exceeding the energy of recombination excitons. When semiconductor TMDs absorb a photon, hot excitons with non-zero kinetic energy are generated [56] (**Figure 3.5)**. The excess energy is distributed between both electrons in conduction bands and holes in valence bands. Dissipation of the kinetic energy of hot excitons occurs by phonon emission due to rapid thermalization with the lattice. The thermalization process occurs within a few to tens of *fs*. The phonon emission process is followed by photon emission. Because PL experiments probe the population of the electronic states, the emission spectrum in PL gives insight into the optical transitions [57]. Typically, PL probes the optical transitions at low energies because of the carriers' relaxation towards low energy states before their radiative recombination. Several parameters can impact the emission spectrum in PL measurements, including,

among others, sample temperature, excitation power, sample quality, dielectric environment, and interference effect.

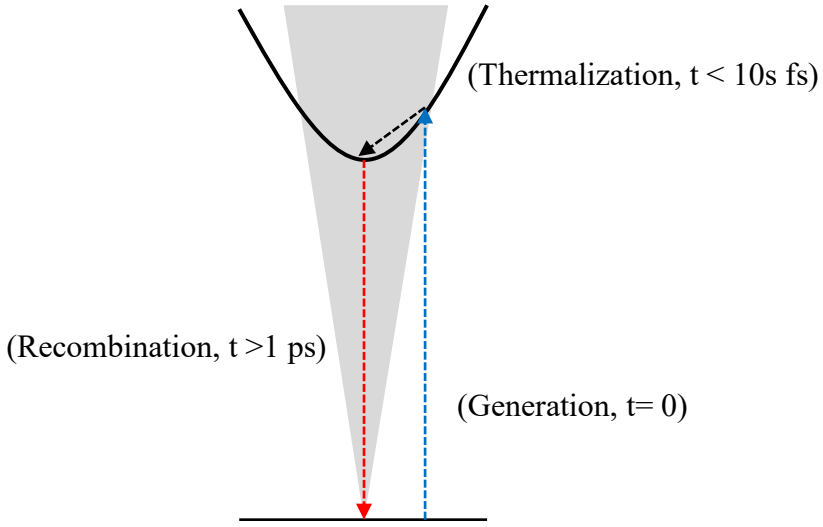

Figure 3.5. Generation an exciton in semiconductor TMDs by absorption a photon. Adopted from (5).

3.3.1 Sample temperature

PL measurements are mostly performed at cryogenic temperatures, e.g. liquid helium temperature (T ~ 4.2 K), because at room temperature the main transitions of A- and B-excitons in TMDs will be broadened due to scattering with phonons. At high temperature regimes, the defect potentials in the lattice will not be efficient enough to act as trapping sites. At low temperatures, phonon absorption is reduced. In addition, spectral linewidth and emission can change compared to the emission at high temperature (**Figure 3.5).**

3.3.2 Excitation power

Laser excitation power significantly impacts PL signal by controlling the number of photoexcited carriers. The average of power per unit area (power density) is related to the photoexcited density in layered TMDs. Carriers can be trapped at defect sites at low laser power, and PL signals will not be detectable. Increasing laser power allows filling of all the defects, so PL of free excitons can then be measured. Further increasing the power to tens of hundreds μW will lead the system towards high exciton concentrations, where phenomena such as biexciton formation and exciton-exciton annihilation can be investigated.

3.3.3 Quality and dielectric environment

The sample's quality and its dielectric environment can drastically impact PL characteristics. Recently, experiments have revealed the critical role of high-quality hBN with low defects as an encapsulated substrate for layered TMDs [58]. The bulk hBN bandgap of 6 eV is high enough to use as an encapsulation layer for monolayer TMDs, providing atomic flatness and very clean, homogeneous dielectric environments. Homogeneous (below 1 meV linewidth) and inhomogeneous (due to sample imperfections such as impurities, defects, interface, substrate, etc.) broadening both contribute to the total line broadening. Because the in-homogenous broadening is significantly suppressed in high-quality encapsulated TMDs monolayers, the linewidth can directly indicate the exciton lifetime (homogeneous broadening). In general, the dielectric environment, surface quality, and flatness have a very significant impact on the intrinsic optical properties of 2D-TMDs and other nanostructures.

3.4 Reflectance Contrast Spectroscopy

The interaction between electromagnetic radiation and various types of oscillators in a material significantly contribute to its optical properties. Optical transitions with large oscillator strength and a high density of states dominate the absorption spectra. For example, in TMD monolayers, exciton resonance is the dominant oscillator. The absorption is not an experimentally measurable quantity, and it is related to the two experimentally observable quantities: optical transmission and reflectance. In our measurements, we prefer to use optical reflectance spectrum alone to characterize the absorption. The transmitted spectrum measurement is difficult due to experimental constraints (e.g. transparent substrate, excitation, and detection path configuration).

We comprise our dual gated bilayer WSe_2 device composites of multilayer thin 2D film (BN, FLG, WSe_2) on SiO_2/Si substrate. Therefore, the interference effects of multilayers can highly complicate the reflection spectrum. In addition, the shape and intensity of the reflection spectrum are strongly dependent on the dielectric function and thickness of each material in the device composite. We perform the reflection measurements by illuminating the sample with broadband light and simultaneously measuring the reflection spectrum from the sample by using the spectrometer and CCD array. We measure the reflection at two locations on the sample: the first includes the entire heterostructure device, and the second contains the heterostructure as the whole minus the TMD layer. This is commonly known as *reflection contrast* spectroscopy, and the reflection contrast is found by $(R_{TMD} - R_{sub})/\, R_{sub}$ (**Figure 3.6).**

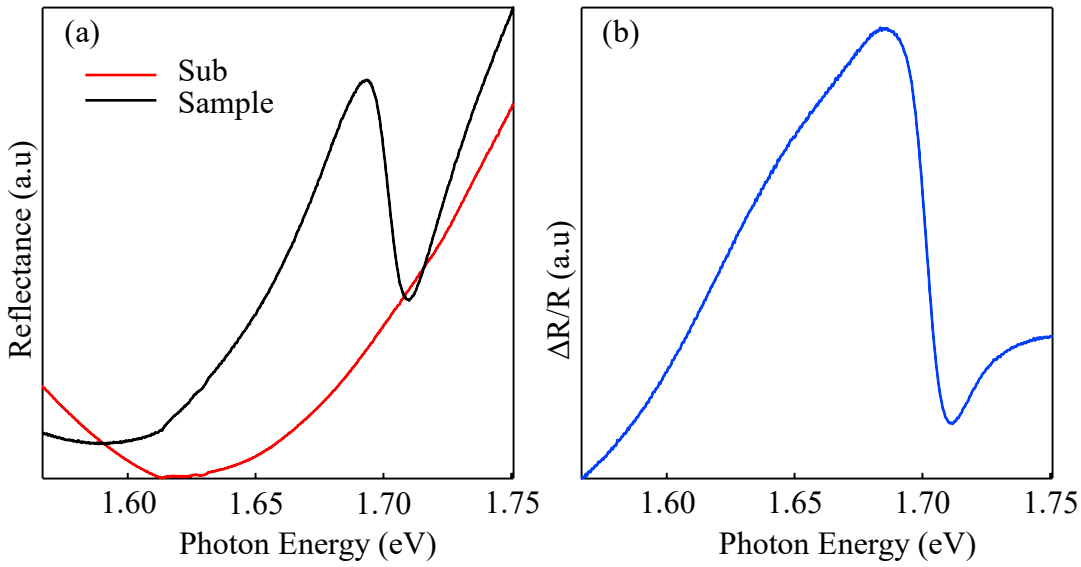

Figure 3.6. Reflection spectra of bilayer WSe_2 heterostructure device: (a) Reflection spectra of a complete heterostructure (black line) and reference spectra (red line) without bilayer WSe_2; **(b)** Reflection contrast spectrum after subtraction the reference spectra.

Chapter 4

Electrically switchable intervalley excitons with strong two-phonon scattering in bilayer WSe_2

4.1 Introduction

When a system hosts multiple competing states, intriguing and complex physics can emerge. Prominent examples include the competing optical modes in a laser, bistable modes in electronics and optics, and competing spin orders in magnets; the properties of these systems can be switched sensitively by the external conditions. For semiconductors, if a material hosts two tunable and competing low-lying states, their interplay can produce intricate optical spectra and enable versatile material engineering. For instance, one may tune the luminescent spectrum of the material by switching the energy order of the states [59]. Also, resonant phonon scattering may occur between two nearly degenerate states, leading to strong electron-phonon coupling [60]. As a result, the material can exhibit a highly tunable spectrum with possibly strong phonon-assisted emission. 2H-stacked bilayer WSe_2 (**Figure 4.1a-b)** is a distinctive material to realize such a novel tunable electron-phonon system. First, it hosts two competing low-lying excitons, namely the QK and QΓ intervalley excitons (X_{QK}, $X_{Q\Gamma}$), which associated with one Γ valence valley at the zone center, two K valence valleys (K, K') at the zone corners, and six Q conduction valleys (Q, Q') in the Brillouin zone (**Figure. 4.1c-d)** [36,61–69]. Although the electronic structure suggests the QK exciton as the lowest-lying exciton, recent theoretical research shows that the QΓ exciton may have similar energy due to the large effective mass of the

Γ valley [68]. Such competing intervalley excitons can hardly be found in other transition metal dichalcogenides (TMDs), such as MoS_2, $MoSe_2$ and WS_2. Second, the QK and QΓ exciton energies can be significantly tuned by electric field. As the QK and QΓ excitons possess different interlayer electric dipole, by applying an out-of-plane electric field, we can adjust their energy separation through the Stark effect [61,69] (**Figure 4.1e)**. Such field-tunability of excitons can hardly be realized in monolayer semiconductors. Third, WSe_2 is known to exhibit strong exciton-phonon interactions, signified by the pronounced phonon replicas in the optical spectra [65]. The above three distinctive characteristics constitute bilayer WSe_2 as a unique tunable exciton-phonon system with potential valleytronic applications.

Experimental research of bilayer WSe_2 has, however, been much hindered by the poor sample quality and the broad and weak optical spectra. For instance, although prior research has shown some theoretical and experimental evidence of QΓ exciton (*e.g.* in quantum-dot emission) [68], direct observation of the QΓ exciton in pristine bilayer TMDs has never been reported. Prior research also studied the Stark effect of QK excitons [61,69], but the related studies of the QΓ Stark effect and the QK and QΓ phonon replicas are still lacking.

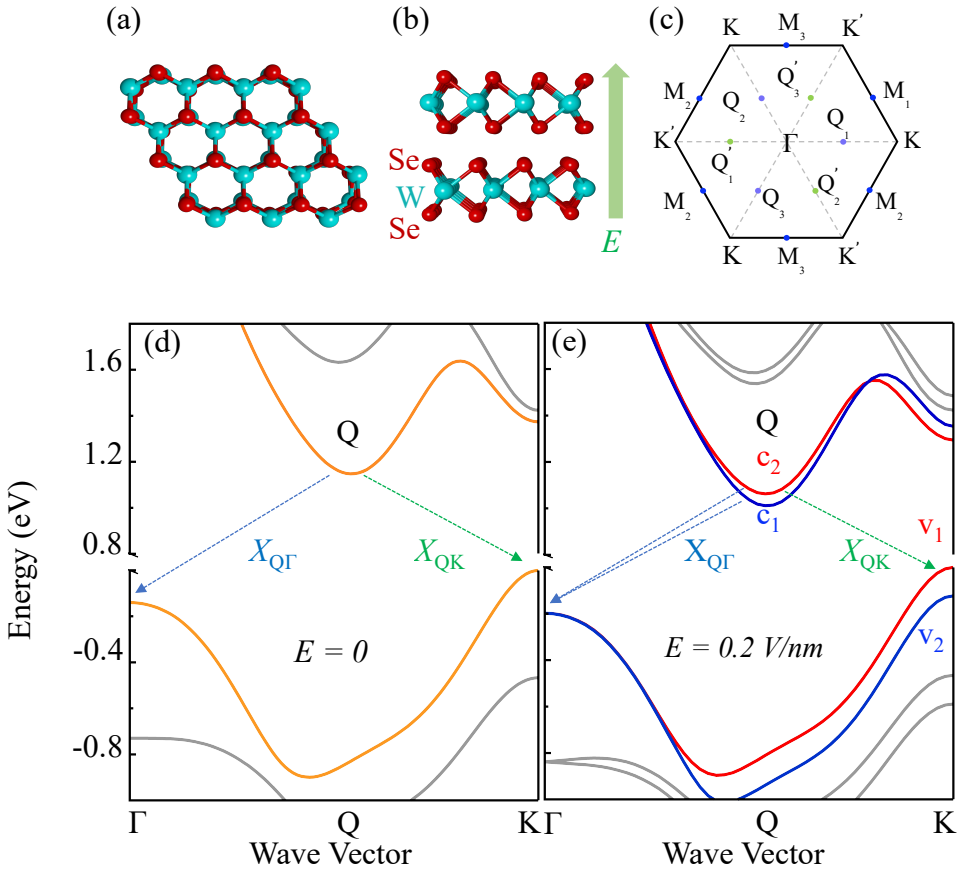

Figure 4.1. Electronic band structure of bilayer WSe_2. **(a)** Top view and **(b)** side view of the crystal structure of 2H-stacked bilayer WSe_2. **(c)** The first Brillouin zone of bilayer WSe_2. **(d-e)** Calculated electronic band structure along the K-Γ line at zero **(d)** and 0.2 V/nm **(e)** vertical electric field. Each band is doubly degenerate at zero field but split at finite field (except at the Γ point). We denote the $X_{Q\Gamma}$ and X_{QK} emission and the dominant spin-up (spin-down) polarization by red (blue) color. The Q and Q' states are energy-degenerate with opposite spins due to the time-reversal symmetry.

4.2 Device fabrication and characterization

We fabricate dual-gated bilayer WSe_2 devices with hexagonal boron nitride (BN) encapsulation by micro-mechanical exfoliation and co-lamination of thin crystals. We use bulk WSe_2 from HQ Graphene Inc. We first exfoliate bilayer WSe_2, thin graphite flakes, and thin BN flakes from their bulk crystals onto silicon substrates with 285-nm-thick SiO_2

epilayer. Afterward, we apply a dry-transfer technique to stack the different thin crystals together. We use a polycarbonate stamp to sequentially pick up the top-gate electrode (thin graphite), top-gate dielectric (thin BN), bilayer WSe_2, contact electrode (thin graphite), bottom-gate dielectric (thin BN), and bottom-gate electrode (thin graphite). Afterward, we transfer the stack of materials onto a Si/SiO_2 substrate and apply the standard electron beam lithography to deposit 100-nm-thick gold electrodes. Finally, the devices are annealed at 360 ℃ for six hours in an argon environment to cleanse the interfaces.

Figure 4.2a displays the optical image of Device #1. The thickness of the BN flake for the top (bottom) gate of Device #1 is determined to be 26 nm (23.7 nm) by atomic force microscope (AFM). **Figure 4.2b** displays the bottom-gate-dependent photoluminescence (PL) map of bilayer WSe_2 with the top gate grounded. We observe the emission of trions (or exciton polarons) on the electron and hole sides. We focus on the exciton PL spectra at the charge neutrality at varying vertical electric field.

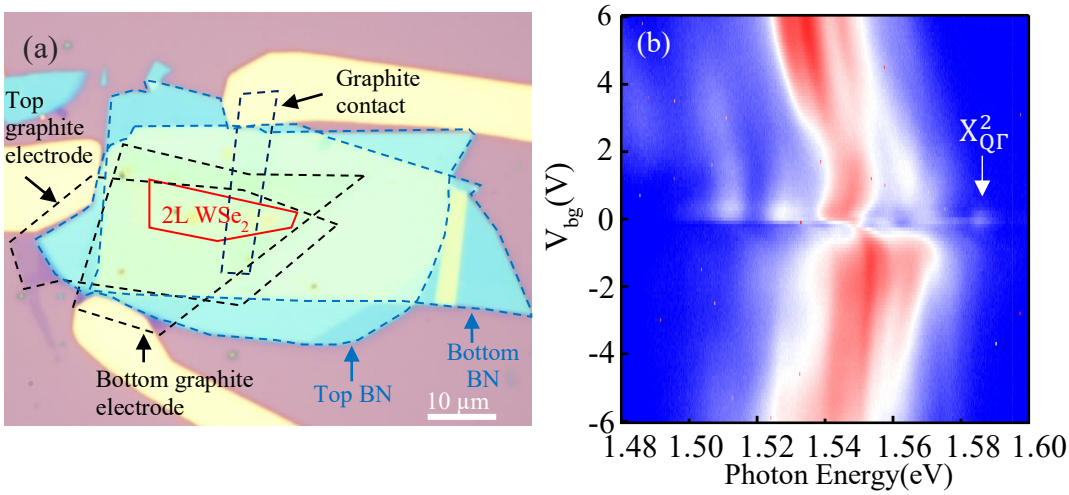

Figure 4.2. Dual gated BN encapsulated bilayer WSe_2 device (a) Optical image of BN-encapsulated bilayer used in the main experiments **(b)** The bottom-gate-dependent photoluminescence (PL) map of the device at sample temperature $T \sim 15$ K under 633-nm continuous laser excitation with incident power of 100 μW. The top gate is grounded in the measurement.

The BN encapsulation significantly improves the sample quality and allows for the observation of QΓ exciton. Thin graphite flakes are used as the contact and gate electrodes to further enhance the device performance. By applying voltages of opposite signs and appropriate ratio on the top gate (V_{tg}) and bottom gate (V_{bg}), we can generate a vertical electric field across bilayer WSe_2 while keeping the sample charge neutral. The V_{tg}:V_{bg} ratio depends on the gating-efficiency ratio of the top and bottom gates, which is affected by their different BN thickness, interfacial and dielectric environment.

4.3 Experimental methods

The photoluminescence (PL) experiments were performed at $T \sim 15$ K in an optical cryostat (Montana) with 532-nm or 730-nm continuous laser excitation. The laser beam was focused by an objective lens (NA = 0.67) onto the sample. The PL was collected through the same objective, passing through a beam splitter, and analyzed by a spectrometer with a CCD camera (Princeton Instruments). The magneto-optical experiment was performed with 17.5 T DC magnet (SCM3) in the National High Magnetic Field Laboratory in Tallahassee, Florida, United States.

4.4 Determination of the vertical electric field across bilayer WSe_2

In our experiment, we have applied gate voltages of opposite signs on the bottom gate (V_{bg}) and top gate (V_{tg}) to induce a vertical electric field across bilayer WSe_2. We adjust the ratio between V_{tg} and V_{bg} so that the sample remains charge neutral in the experiment. We solve the electrostatic problem in our devices to determine the strength of the electric field (E) across bilayer WSe_2 from $\Delta V = V_{tg} - V_{bg}$.

Figure 4.3 displays the electrostatic geometry of our BN-encapsulated devices, which consists of a WSe_2 bilayer with thickness d sandwiched between two BN layers with thickness d_1 and d_2. The static dielectric constant of bilayer WSe_2 and BN along the vertical direction are denoted as ε_{2L} and ε_{BN}, respectively. The electric fields across the top BN, bilayer WSe_2, and bottom BN are denoted as E_1, E, E_2, respectively. The voltage difference (ΔV) between the top and bottom gates is related to the electric fields as

$$\Delta V = d_1 E_1 + dE + d_2 E_2 \quad (1)$$

As the electrostatic gating injects no net charge into the WSe_2 bilayer, the boundary conditions at the two interfaces are

$$\varepsilon_{BN} E_1 = \varepsilon_{2L} E = \varepsilon_{BN} E_2 \quad (2)$$

Combining Eq. (1) and (2), we obtain

$$E = \frac{\Delta V}{\frac{\varepsilon_{2L}}{\varepsilon_{BN}}(d_1 + d_2) + d} \quad (3)$$

In our calculation, we use d = 1.3 nm for the WSe_2 bilayer, d_1 = 26 nm and d_2 = 23.7 nm for the top and bottom BN, respectively, for Device #1. We use dielectric constant ε_{2L} = 5.51 for bilayer WSe_2, which is obtained from our theoretical calculation in Section 1.5 above. We use dielectric constant ε_{BN} = 2.69 for BN, which is consistent with the literature [61,70,71]. The calculated electric field for varying ΔV is shown in **Figure 4.4d.**

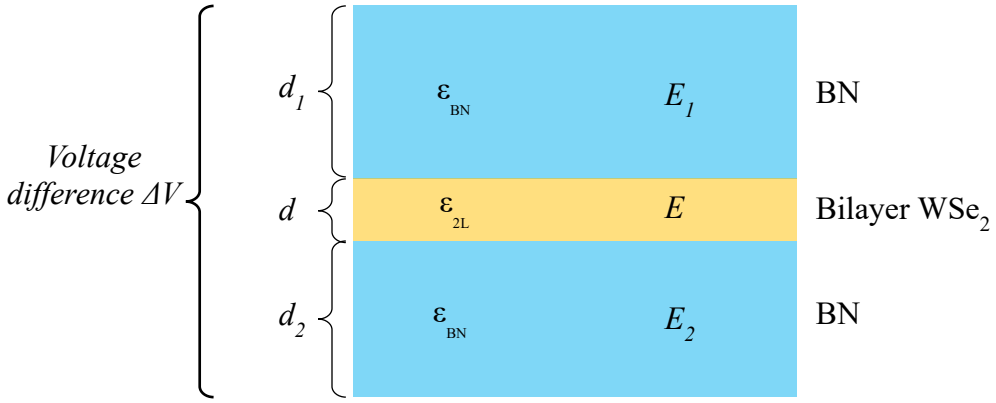

Figure 4.3. Electrostatic geometry of our BN-encapsulated bilayer WSe_2 devices

4.5 Experimental results

By using ultraclean bilayer WSe_2 devices encapsulated by boron nitride (BN), we directly resolve the QΓ exciton emission and conduct comparative electric-field-dependent studies between the QΓ and QK excitons and phonon replicas. In contrary to the suggestion of the free-particle band structure **Figure 4.1d,** we observe that the QΓ exciton lies at ~18 meV below the QK exciton; this reveals considerably stronger binding of the QΓ exciton than the QK exciton. We also observe strong Stark effect in both excitons under an out-of-plane electric field, but the QΓ Stark shift is considerably weaker than the QK shift. By tuning the electric field strength between 0 and 0.11V/nm, we can switch the energy order of the QΓ and QK excitons and control which exciton dominates the emission spectra. Notably, both excitons exhibit strong two-phonon replicas, which are comparable to or even brighter than the one-phonon replicas and outshine the primary emission. We can simulate the replica spectra by comprehensive theoretical calculation. Our results reveal the existence of numerous two-phonon scattering processes with (nearly) resonant exciton-

phonon scattering, which lead to unusually strong two-phonon replicas in bilayer WSe_2. Overall, our research demonstrates bilayer WSe_2 as a unique valleytronics material with switchable intervalley excitons and strong two-phonon scattering, which can hardly be found in other atomically thin semiconductors.

Figure 4.4b displays the photoluminescence (PL) map at varying voltage difference ($\Delta V = V_{tg} - V_{bg}$) between the top and bottom gates at temperature $T \sim 15$ K. At low ΔV, we observe multiple X-shape emission features; such field-dependent X-shape features have never been reported in bilayer WSe_2. At large ΔV, several redshifting lines appear; they should be associated with the QK exciton according to prior research [61]. We further perform second-order energy derivative on the PL map to resolve the fine features, **Figure 4.4c.** From the map of the second-order derivative, we extract the energies of different emission features and plot them as a function of electric field in **Figure 4.4d.** We first consider the two sets of highest-energy features, which consist of one X-shape feature and two redshifting lines in 1.60 – 1.63 eV (**Fig 4.4b-d**). They are significantly weaker than the replica features at lower energy. We tentatively assign them as the primary $X_{Q\Gamma}$ and X_{QK} emission assisted by defect scattering (here "Q" includes all six Q and Q' valleys). Defect scattering is considered because direct optical recombination of intervalley excitons is forbidden by the momentum conservation [72,73]. To confirm our assignment, we conduct first-principles calculations on the band structure of bilayer WSe_2 under different vertical electric fields (**Figure 4.1d-e).** At zero field, each band is doubly degenerate due to the inversion and time-reversal symmetry of 2H-stacked bilayer WSe_2 [62,69,74] **Figure. 4.1d.**

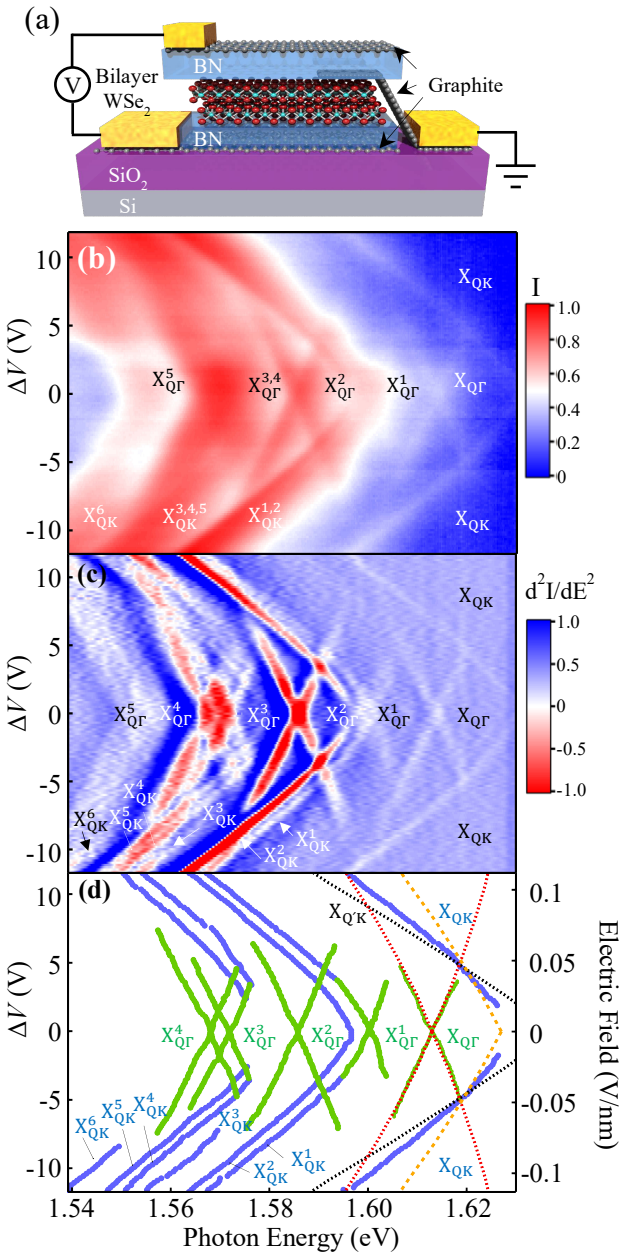

Figure 4.4. Electric-field-dependent photoluminescence (PL) of a bilayer WSe_2 device. (a) Schematic of our dual-gate BN-encapsulated bilayer WSe_2 devices. **(b)** PL map of a bilayer WSe_2 device at varying voltage difference $\Delta V = V_{tg} - V_{bg}$ between the top and bottom gates while keeping the sample charge neutral. The measurements were conducted at temperature $T \sim 15$ K under 730-nm continuous laser excitation with incident power ~15 μW. **(c)** Second-order energy derivative of panel b. **(d)** Extracted energy of emission features in panel c. The primary QΓ and QK exciton emission ($X_{Q\Gamma}$, X_{QK}) and phonon replicas ($X_{Q\Gamma}^{1-5}$, X_{QK}^{1-6}) are denoted. The dashed lines are the calculated Stark shifts of the QΓ (red), QK (orange), and Q'K (black) spin-allowed optical transitions.

At the finite electric field, the inversion symmetry is broken, and each band is split into two bands with opposite spin and layer polarizations (except at the Γ point), **Figure. 4.1e.** Consequently, the $X_{Q\Gamma}$ and X_{QK} emission lines are split and exhibit different Stark shifts. We have calculated the energies of spin allowed QΓ, QK and Q'K optical transitions at different electric fields via the density functional theory (DFT). The spin-allowed QK and Q'K transitions involve the upper and lower split conduction bands, respectively, because the Q and Q' states have opposite spins; hence they have somewhat different Stark shifts. We neglect the influence of excitonic effect on the Stark shift, offset each theoretical transition energy to match the corresponding experimental energy, and focus our comparison only on the Stark shifts. The theoretical Stark shifts (dashed lines in **Figure 4.4d**) agree decently with our data and hence supports the assignment of QΓ and QK excitons.

The QΓ exciton exhibit two remarkable characteristics. First, $X_{Q\Gamma}$ is ~18 meV lower than X_{QK} and is significantly brighter than X_{QK}. This result is surprising because the Γ valence valley is ~140 meV lower than the K valence valley in the electronic band structure (**Figure. 4.1d)** [36,44,75,76]; one would naturally expect that the QΓ transition has higher energy than the QK transition. However, further examination of the band structure reveals that the Γ valley has a much larger hole effective mass (~1.48m_0) than the K valence valley (~0.43m_0; m_0 is the free electron mass) [75] (**Table 4.1** in the section 4.7 below). Hence, the QΓ exciton binds more strongly than the QK exciton. The larger exciton binding energy causes $X_{Q\Gamma}$ to have lower energy than X_{QK}.

This result is significant because the lowest excitonic state plays a paramount role in the excitonic dynamics and luminescence.

Second, the $X_{Q\Gamma}$ Stark shift (~135 meV per 1 V/nm field) is about 1.9 ~ 2.7 times weaker than the X_{QK} Stark shift (265 ~ 360 meV per 1 V/nm field). This can be qualitatively understood from their different charge density distribution. **Figure 4.5** shows our calculated spin-dependent charge density along the vertical direction for electron states at the Q, K, and Γ points (the Q' states have the same density distribution as the Q states but opposite spin). We consider an infinitesimal electric field to break the inversion symmetry. The separated states show strong spin polarization – the electric field essentially splits them into spin-up and spin-down states.

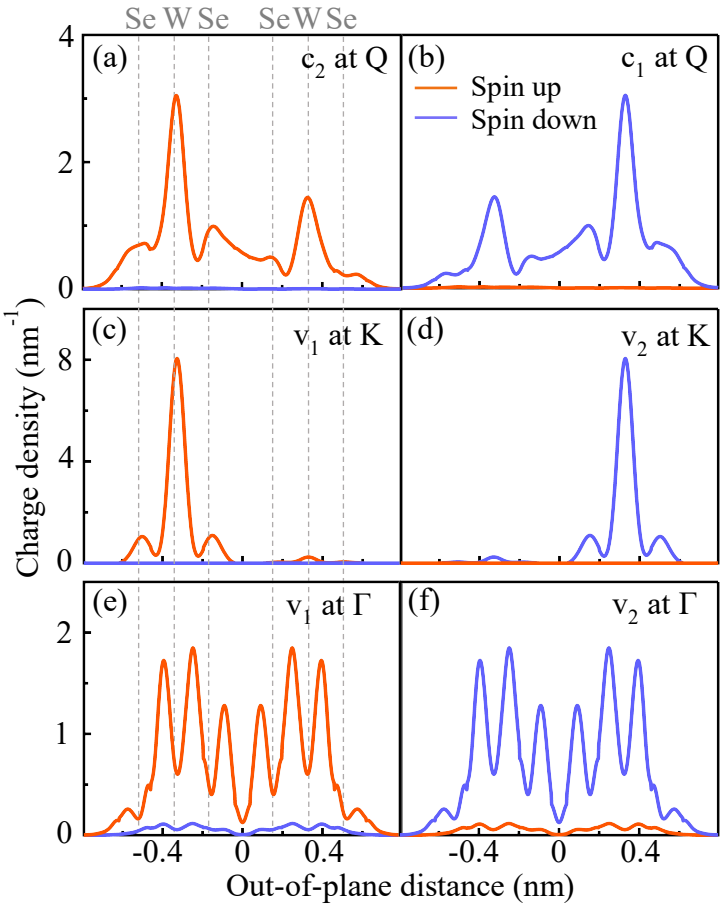

Figure 4.5. Calculated spin-dependent in-plane-averaged charge density along the out-of-plane direction. **(a-b)** Density for the electron states at the Q point of the conduction bands c_1 and c_2. The time-reversal states at the Q' point have the same density distribution but opposite spin. **(c-f)** Density for the states at the K and Γ points of the valence bands v_1 and v_2. An infinitesimal vertical electric field is considered to separate the states. The states at c_1 (v_1) and c_2 (v_2) have opposite spin and layer polarization. The vertical dashed lines denote the central position of the atoms. We note that the density maxima of the Γ-point electrons are not at the center of the atoms due to their specific orbitals.

The K, Q, and Γ states show different layer polarization. The Q conduction states show medium layer polarization with an electric dipole moment $p_Q = 0.107\ e \cdot nm$, where $e = 1.6 \times 10^{-19} C$ is the elementary electric charge **Figure 4.5a, b.** In contrast, the K valence states are strongly localized in opposite layers, giving rise to a large dipole moment $p_K = 0.307\ e \cdot nm$ **Figure 4.5c, d.** In the other extreme, the two Γ valence states show

symmetric distribution on the two layers, which produces no layer polarization and zero electric dipole moment ($p_\Gamma = 0$), **Figure 4.5e, f.**

By combining these dipole moments, we estimate that a QΓ electron-hole pair has a dipole moment of $p_{Q\Gamma} = p_Q - p_\Gamma = 0.107\, e \cdot nm$, and an optically active QK (Q'K) electron-hole pair has a dipole moment of $p_{QK} = p_K - p_Q = 0.200\, e \cdot nm$ ($p_{Q'K} = p_K + p_Q = 0.417\, e \cdot nm$). The average of p_{QK} and $p_{Q'K}$ (~0.3 $e \cdot nm$) is about three times of $p_{Q\Gamma}$. This roughly account for the difference between the $X_{Q\Gamma}$ and X_{QK} Stark shift.

The different Stark shifts between $X_{Q\Gamma}$ and X_{QK} have an interesting consequence – they allow us to use the electric field to switch the energy order and dominant luminescence between $X_{Q\Gamma}$ and X_{QK}(**Figure 4.4b; Figure**)When the electric field is weak (*e.g.,* $E < 0.02$ V/nm), $X_{Q\Gamma}$ lies well below X_{QK} and dominates the emission due to its higher population. As the field increases, X_{QK} gradually redshifts to become lower than $X_{Q\Gamma}$, and the exciton population transfers from $X_{Q\Gamma}$ to X_{QK}; this brightens X_{QK} and suppresses $X_{Q\Gamma}$. At strong electric field (*e.g.,* $E > 0.08$ V/nm), X_{QK} dominates the luminescence. Such electric-field-switchable excitons are not found in monolayer TMDs and may find novel applications for bilayer TMDs.

After we address the primary $X_{Q\Gamma}$ and X_{QK} emission, we turn to their replica emission at lower energy. **Figure 4.4** shows five $X_{Q\Gamma}$ replicas ($X^1_{Q\Gamma} - X^5_{Q\Gamma}$) with respective redshift energies 13.0, 27.6, 41.7, 45.7, and 57.7 meV from $X_{Q\Gamma}$ and six X_{QK} replicas ($X^1_{QK} - X^6_{QK}$) with respective redshift energies 28.8, 32.4, 41.9, 46.2, 49.1, and 58.3 meV from X_{QK} (the uncertainty of these energies is from $\pm$ 1 to $\pm$2; **Table 4.6**). The replicas exhibit identical

Stark shifts to the primary emission lines. We tentatively attribute them to excitonic luminescence assisted by phonon emission, as phonon replicas have been reported in monolayer WSe_2 [72,73,77–79] and bilayer WSe_2 [8]. In our results, the replicas are considerably brighter than the primary emission, indicating that phonon-assisted emission is more efficient than defect-assisted emission in our system.

To identify the phonon replicas, we have calculated the phonon band structure of bilayer WSe_2 with a rigid-ion model **Figure 4.8**. Afterward, we calculate the one-phonon replicas for $X_{Q\Gamma}$ and X_{QK} by the perturbation theory. All of these calculations are done with zero external electric field. In our theory, the initial excitonic state is scattered to a second excitonic state by emitting a phonon, then the second state decays to emit a photon. The second state is not necessarily a bound exciton, but it must be a momentum-direct exciton in order to emit the photon. Momentum conservation restricts the one-phonon scattering processes to occur only through two paths. For $X_{Q\Gamma}$, the electron may be scattered from Q to Γ by emitting a phonon ($X_{Q\Gamma} \rightarrow X_{\Gamma\Gamma}$), or the hole may be scattered from Γ to Q by emitting a phonon ($X_{Q\Gamma} \rightarrow X_{QQ}$). Similarly, for X_{QK}, the electron can be scattered from Q to K ($X_{QK} \rightarrow X_{KK}$), or the hole from K to Q ($X_{QK} \rightarrow X_{QQ}$). As the initial $X_{Q\Gamma}$ and X_{QK} excitons can be associated with any of the six Q valleys and two K valleys, the momentum of the emitted phonons will be near one of the six Q points for $X_{Q\Gamma}$ and near one of the Q or M points for X_{QK}. The emitted phonon can come from any phonon branch, so the one-phonon replica spectra can exhibit multiple peaks (see **Table 4.3** and **Figure 4.10** below)

These one-phonon scattering processes are all non-resonant, so the one-phonon replicas are generally weak.

Figure 4.6 compares our calculated one-phonon spectra for $X_{Q\Gamma}$ and X_{QK} with the experimental spectra. We phenomenologically broaden the theoretical spectra by 2 meV to match the experimental peak width. The theoretical one-phonon spectra can account for the $X^1_{Q\Gamma}$ peak, which is contributed dominantly by the LA and TA acoustic phonons near the Q points. It can also partially explain $X^2_{Q\Gamma}$ and $X^{1,2}_{QK}$. But other replicas ($X^{3-5}_{Q\Gamma}$ and X^{3-6}_{QK}) exceed the range of single phonon energy (~37 meV) in WSe_2. We would need to consider higher-order scattering processes to explain these replicas.

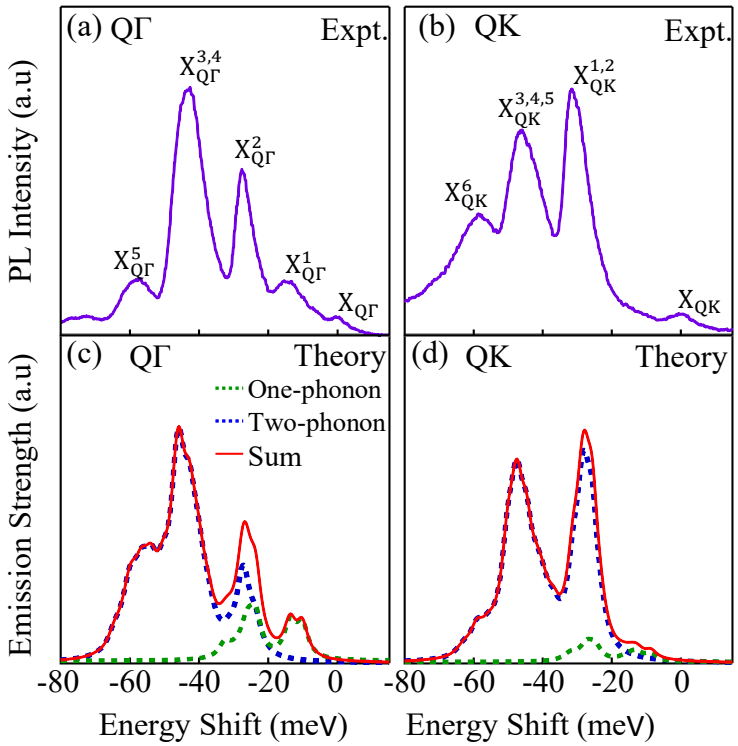

Figure 4.6. Theoretical simulation of the phonon-replica spectra. (a) Experimental QΓ emission spectrum at $\Delta V = 0$ in Fig. 2b, offset by the $X_{Q\Gamma}$ energy. **(b)** Experimental QK emission spectrum at ΔV = -10 V in Fig. 4.3b, offset by the X_{QK} energy. **(c-d)** Simulated spectra of one-phonon and two-phonon replicas for $X_{Q\Gamma}$ **(c)** and X_{QK} **(d)**. Both theoretical spectra are broadened for 2 meV to match the experimental peak widths.

We have conducted comprehensive calculations on the two-phonon replicas of $X_{Q\Gamma}$ and X_{QK} with zero external electric field. In our theory, the initial exciton is scattered to a second excitonic state by emitting a phonon, and afterward scattered to a third excitonic state by emitting another phonon, and the third state decays to emit a photon. The second and third states are not necessarily bound excitons, but the third state may be a momentum-direct exciton in order to emit the photon. In contrast to the one-phonon processes with only two scattering paths, the two-phonon processes have numerous scattering paths. In

our calculation, we only consider those scattering paths involving a resonant or nearly resonant exciton-phonon scattering process. In bilayer WSe_2, the six Q conduction valleys are energy-degenerate, and $X_{Q\Gamma}$ and X_{QK} are close in energy (~18 meV). So, carrier-phonon scattering between different Q valleys, between the Γ and K valence valleys, or within the same valley, is resonant or nearly resonant. Two-phonon processes involving such (nearly) resonant scattering are expected to contribute dominantly to the replica spectra.

In our survey, there are totally 16 two-phonon scattering paths with a (nearly) resonant component for QΓ exciton. They can be separated into four groups: $X_{Q\Gamma} \rightarrow X_{Q'\Gamma} \rightarrow X_{Q'Q'}$; $X_{Q\Gamma} \rightarrow X_{Q'\Gamma} \rightarrow X_{\Gamma\Gamma}$; $X_{Q\Gamma} \rightarrow X_{QK} \rightarrow X_{KK}$; $X_{Q\Gamma} \rightarrow X_{QK} \rightarrow X_{QQ}$ (here Q′ denotes any of the six Q valleys). Similarly, there are 14 dominant paths for the QK exciton, separated into four groups: $X_{QK} \rightarrow X_{Q'K} \rightarrow X_{KK}$; $X_{QK} \rightarrow X_{Q'K} \rightarrow X_{Q'Q'}$; $X_{QK} \rightarrow X_{Q\Gamma} \rightarrow X_{QQ}$; $X_{QK} \rightarrow X_{Q\Gamma} \rightarrow X_{\Gamma\Gamma}$, theoretical calculation in Section 4.11 below have the explanation of these paths. Momentum conservation restricts the emitted phonons to be near the Γ, K, Q, and M points. The emitted phonons can come from any phonon branch, so the two-phonon replica spectra are rather complicated (**Tables 4.3, 4.5**).

Fig. 4.6c-d display our calculated and broadened two-phonon replica spectra, which include contributions from all the above-mentioned scattering paths and all phonon branches. By summing the one-phonon and two-phonon spectra, our total theoretical spectra match decently the experimental spectra, including the energy and relative intensity

of different replica peaks. From the theoretical results, we can attribute $X_{Q\Gamma}^{1}$ to the one-phonon replica of Q-point acoustic phonons, $X_{Q\Gamma}^{2}$ to a superposition of one-phonon and two-phonon replicas, $X_{Q\Gamma}^{2-5}$ and X_{QK}^{1-6} to two-phonon replicas (**Table 4.6** below for detailed assignments of each replica peak). In particular, X_{QK}^{1-5} are dominantly contributed by two-phonon paths involving the $X_{QK} \rightarrow X_{Q\Gamma}$ transition with acoustic phonon emission, because this transition is strongly resonant when the emitted phonon energy is close to the 18-meV difference between X_{QK} and $X_{Q\Gamma}$ (**Table 4.5).**

We remark that the two-phonon replicas are considerably stronger than the one-phonon replicas. This characteristic is counter-intuitive because second-order processes are usually much weaker than first-order processes. There are two reasons for this unusual phenomenon. First, one of the scattering components in the two-phonon processes is (nearly) resonant. This makes each considered two-phonon process as strong as a non-resonant one-phonon process. Second, the number of (nearly) resonant two-phonon scattering paths ($\geq$14) considerably exceeds the number of one-phonon scattering paths (only 2). After summing the contributions of these two-phonon paths, the total two-phonon spectra become considerably stronger than the one-phonon spectra.

We also note that the numerous resonant scattering channels are related to the existence of six degenerate Q valleys and two degenerate K valleys in bilayer WSe_2 and are hence rare in condensed matter systems. They are not found in monolayer WSe_2 or other TMDs

due to the large energy separation between the QK and QΓ excitons in these systems. Therefore, bilayer WSe_2 is a quite distinctive system to study novel exciton-phonon phenomena.

4.6 Zeeman splitting of the QΓ exciton emission in bilayer WSe_2

The QΓ exciton state is formed by the hole states in the Γ valley and the electron states in six energy-degenerate Q valleys. The six Q valleys can be separated into two groups – the Q_1, Q_2, Q_3 valleys and the Q_1', Q_2', Q_3' valleys, **Figure 4.1e.** The three valleys in each group are related to each other by three-fold rotational symmetry. The two groups of valleys are related to each other by time-reversal symmetry.

The application of a vertical magnetic field preserves the three-fold rotational symmetry but breaks the time-reversal symmetry. As a result, the degeneracy between the Q_1, Q_2, Q_3 valleys and the Q_1', Q_2', Q_3' valleys are lifted. Correspondingly, the QΓ exciton state will be split into two states, each associated with either the Q_1, Q_2, Q_3 valleys or the Q_1', Q_2', Q_3' valleys. Moreover, the two-fold generate states at the Γ point will also be split under magnetic field and contribute to the splitting of the QΓ exciton. Similar valley Zeeman splitting effect has been studied extensively for the K-valley excitons in monolayer TMDs [80–83].

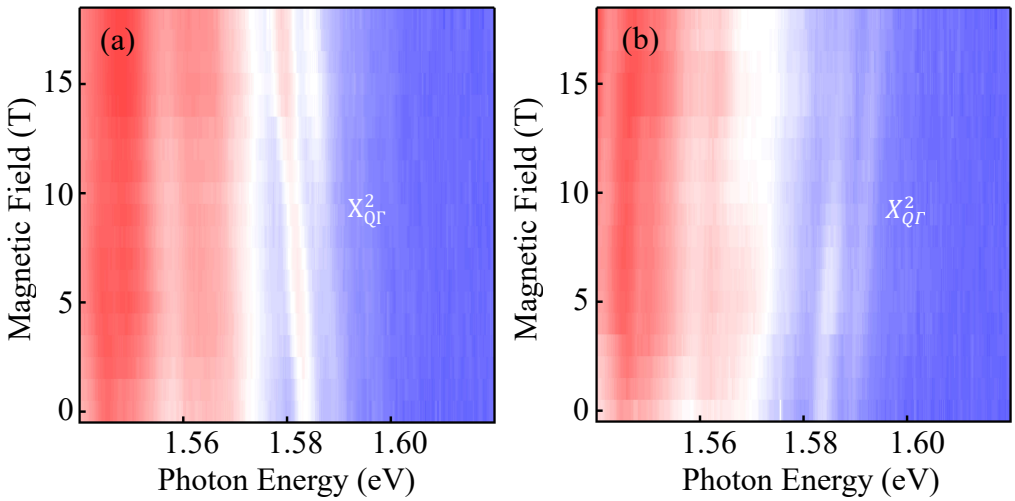

Figure 4.7. **Zeeman splitting of the QΓ exciton. (a-b)** Magnetic-field-dependent PL maps of bilayer WSe_2 at right-handed **(a)** and left-handed **(b)** circular polarization at ΔV = -1 V under linearly polarized 532-nm laser excitation. The $X^2_{QΓ}$ replica is split into two lines by the Stark effect at finite ΔV. Each line is further split into two lines with opposite helicity and exhibits linear Zeeman shift under magnetic field.

We have measured the PL spectra of QΓ exciton and replicas under finite vertical magnetic field and electric field **Figure 4.7.** We cannot see clearly the primary $X_{QΓ}$ line due to its weak signal, but we can observe the $X^2_{QΓ}$ replica, which are split into two lines by the Stark effect under electric field. The $X^2_{QΓ}$ replica is further split into four lines under magnetic field. Two lines show right-handed circular polarization and redshift with increasing magnetic field; the other two lines show left-handed circular polarization and blueshift with increasing magnetic field. We attribute such magnetic-field-dependent splitting to the valley Zeeman effect, in which emission with opposite helicity comes from excitons associated with the Q_1, Q_2, Q_3 valleys and the Q_1', Q_2', Q_3' valleys.

The energy separation (ΔE) between $X^2_{Q\Gamma}$ lines with opposite helicity exhibit linear dependence on the magnetic field, which can be described by $\Delta E = g\mu_B B$, where μ_B is the Bohr. magneton, B is the magnetic field, and g is the effective g-factor. From our data, we extract a g-factor of ~9. This value is consistent with the g-factor (g = 9.5) obtained by a prior experiment that measured quantum-dot emission associated with the QΓ exciton in bilayer WSe_2 [68]. Further research is merited to understand the optical selection rules and g-factor of $X^2_{Q\Gamma}$.

4.7 Comparison of QΓ and QK exciton emission energies

From the theory-experiment comparison of the electric-field-dependent energy shift **Figure 4.4d,** we can identify the higher-energy emission lines at 1.62 – 1.63 eV as the QK exciton and the lower-energy emission lines at 1.605 – 1.62 eV as the QΓ exciton. However, in the band structure obtained by DFT, the valence band is 70 – 140 meV higher at the K point than at the Γ point. That is, the Q-Γ transition energy exceeds the Q-K transition energy by 70 – 140 meV. This apparently contradicts against our result that QΓ exciton lies below the QK exciton. This implies that the QΓ exciton has much larger binding energy than the QK exciton. There are three factors that contribute to the stronger binding of the QΓ exciton.

First, the QΓ exciton has larger effective mass than the QK exciton. Table 4.1 lists the effective carrier mass at the K, Γ, and Q points calculated with WIEN2k. From the orientation-averaged effective mass at the K, Γ, and Q points, we deduce the reduced mass (μ_X) for the QK and QΓ excitons to be $0.247m_0$ and $0.417m_0$ respectively, where m_0 is the free electron mass. By using the effective-mass approximation and a Keldysh potential

fitted to the DFT results, we have calculated the QK exciton binding energy, which lies between 100 and 140 meV for an effective dielectric constant between 4 and 5.5. By considering the ratio of the effective mass between the K and Γ points, we can deduce that the QΓ exciton binding energy can reach 170 – 240 meV. Such enhanced binding energy can partially counter the 70 – 140 meV difference in the QΓ ad QK interband transition energies.

Second, in the Brillouin zone of bilayer WSe_2, there are six inequivalent Q valleys, all of which contribute equally to the formation of QΓ exciton. In contrast, only three of the six Q valleys contribute significantly to the QK exciton formation, whereas the other three are further away and have negligible contribution. The double number of Q valleys in the QΓ exciton formation can significantly enhance its binding energy compared to the QK exciton.

Third, the larger effective mass of QΓ exciton can cause a larger spread of the exciton envelop function in the k-space, which can lead to significant intervalley mixing and further enhancement of the excitonic binding. For instance, previous studies of donor states in silicon shows that the intervalley mixing effect can increase the donor binding energy by 50% [84]. Similar effect is expected in the QΓ intervalley exciton here.

By combining the three factors above, it is reasonable that the QΓ exciton binding energy can exceed the QK exciton binding energy by more than the difference in the QΓ ad QK interband transition energies, thus making the QΓ exciton emission energy lower than the QK exciton energy.

	K_{v1}	Γ_{v1}	Q_{v1}	Q_{c1}	K_{c1}	K_{c2}
$m_{\|\|}$	0.42	1.47	∞	0.49	0.44	0.34
$m_{\perp}$	0.44	1.49	1.47	0.72	0.43	0.32

Table 4.1. Band-edge effective masses (in unit of m_0) at K, Γ, and Q points. We note that the Q_{v1} band has a linear dispersion along the Γ-K axis at the Q point; thus, we take $1/m_{||} = 0$.

4.8 Density distribution and electric dipole of band-edge states in bilayer WSe_2

To understand the physical mechanism for the electric-field-induced energy splitting, we calculate the *z*-dependent charge density averaged over the *x*-*y* plane for the Bloch states in the bottom conduction band (c1) at Q and the top valence band (v1) at K and Γ in bilayer WSe_2 via DFT by using the relation

$$\rho_{\mu}(z_e) = \left\langle \psi_{\mu,K} \left| \frac{1}{L_c} \sum_{g_z} e^{ig_z(z-z_e)} \right| \psi_{\mu,K} \right\rangle, \quad (4)$$

where μ labels the Bloch states (K_{v1}, Γ_{v1}, Q_{c1}, and Q_{c2}) of concern. Since ρ_{μ} is not provided by the WIEN2k package [85–87], we use the wave functions obtained from the LASTO (linear augmented Slater-type orbitals) package to calculate the in-plane averaged charge density according to Eq. (4). Here the Bloch states are calculated via a supercell method and L_c is the length of the supercell used. The band structures obtained by LASTO package are nearly the same as those by WIEN2k with suitable choice of LASTO basis functions. Both approaches are based on all-electron (both core and valence electrons) DFT with augmented basis functions. The LASTO basis functions are properly selected linear combinations of the augmented plane waves (APWs).

Figure 4.5 above displays our calculated charge densities $\rho_\mu(z)$ for the K_{v1}, Γ_{v1}, Q_{c1}, and Q_{c2} states in bilayer WSe_2 under a small electric field (E = 0.001 V/nm). The purpose of using a small electric field is to break the inversion symmetry so that we can see the spin and layer dependence of the wavefunctions when their degeneracy is lifted. The results allow us to calculate the dipole moment and the spin angular momentum of each state. The calculated dipole moment for the K_{v1}, Γ_{v1}, and Q_{c1} states are 0.307, 0, and 0.107 $e \cdot nm$, respectively.

4.9 Calculation of phonon modes by a rigid-ion model for bilayer WSe_2

Besides the field-dependent emission energy shift discussed above, our experiment also reveals phonon replicas of the QΓ and QK excitons. We have carried out comprehensive theoretical calculations on the phonon replica spectra. In this section, we will first describe our calculation of the phonon band structure and phonon polarization vectors of bilayer WSe_2. In the following sections, we will present our theory to calculate the phonon replica spectra.

We adopt a rigid-ion model (RIM) [88] to obtain the phonon polarization vectors. In this model, we consider only the short-range ion-ion Coulomb interaction. We neglect the long-range ion-ion Coulomb interaction (due to charge transfer between W and Se atoms), which should be insignificant given the very small energy splitting between the LO and TO phonon modes at the zone center [89]. The weak long-range ion-ion interaction indicates that WSe_2 is a highly covalent material with little inter-atomic charge transfer.

Figure 4.8 displays the configuration and labels of the atoms in the bilayer WSe_2 unit cell, which includes one W atom and two Se atoms in both the bottom and top WSe_2

monolayer. In the unit cell, we define the position of the W atom in the bottom WSe_2 monolayer as the origin of our coordinate system. The two nearby Se atoms are located at $(a/\sqrt{3}, 0, \pm d/2)$, where a is the in-plane lattice constant and d is the vertical distance between the lower and upper Se atoms in the bottom WSe_2 monolayer. Below we will define a set of dynamic matrices to obtain the phonon dispersion. The form of these matrices is determined by symmetry analysis.

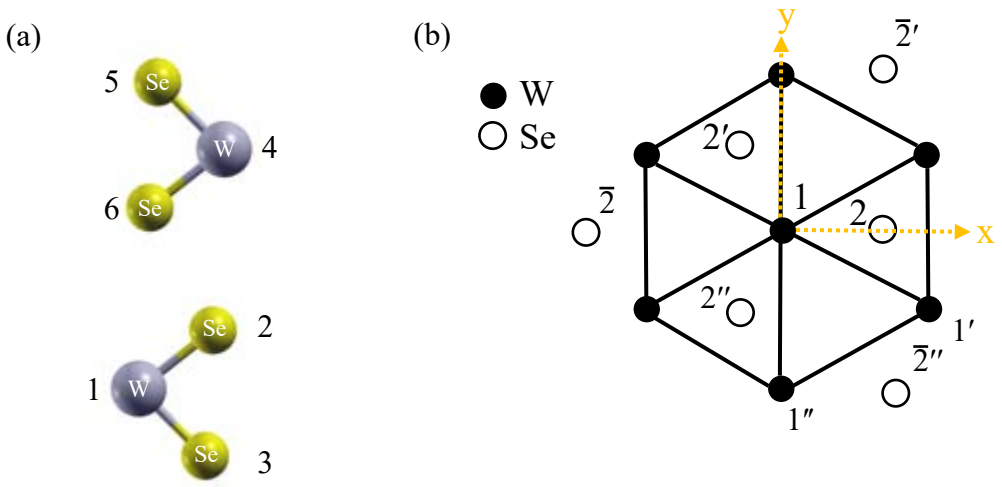

Figure 4.8. Configuration and labels of the ats in the bilayer WSe_2 unit cell (a) The side view of the unit cell of bilayer WSe_2. **(b)** The bottom view of the lower WSe_2 layer in the unit cell. The numerical labels for different atoms are shown.

The dynamic matrix for the nearest-neighbor interaction between the W atom at the origin (labeled as 1) and the Se atom at $(a/\sqrt{3}, 0, -d/2)$ (labeled as 2) has the form of

$$D^{12} = \begin{pmatrix} A_1 & 0 & D_1 \\ 0 & B_1 & 0 \\ E_1 & 0 & C_1 \end{pmatrix},$$

where $A_1 - E_1$ denote the interaction parameters for the nearest-neighbor interaction.

The dynamic matrix between the Se atom at $(a/\sqrt{3}, 0, -d/2)$ (labeled as 2) and the Se atom at $(-a/\sqrt{3}, -a, -d/2)$ (labeled as $2'$) has the form:

$$D^{22'} = \begin{pmatrix} A_2 & 0 & D_2 \\ 0 & B_2 & E_2 \\ D_2 & -E_2 & C_2 \end{pmatrix}.$$

The dynamic matrix between the W atom at the origin (labeled by 1) and the W atom at $(0, -a, 0)$ (labeled by $1'$) has the form:

$$D^{11'} = \begin{pmatrix} A_3 & 0 & 0 \\ 0 & B_3 & 0 \\ 0 & 0 & C_3 \end{pmatrix}.$$

The dynamic matrix for the next-neighbor interaction between the Se atom at $(a/\sqrt{3}, 0, -d/2)$ (labeled as 2) and the Se atom at $(a/\sqrt{3}, 0, d/2)$ has the form:

$$D^{23} = \begin{pmatrix} A_4 & 0 & 0 \\ 0 & A_4 & 0 \\ 0 & 0 & C_4 \end{pmatrix}.$$

The dynamic matrix for the second nearest-neighbor interaction between the W atom at the origin (labeled as 1) and the Se atom at $(-2a/\sqrt{3}, 0, -d/2)$ (labeled as $\bar{2}$) has the form:

$$\mathrm{D}^{1\bar{2}} = \begin{pmatrix} A_5 & 0 & D_5 \\ 0 & B_5 & 0 \\ E_5 & 0 & C_5 \end{pmatrix}.$$

The above five dynamic matrices describe the phonons of monolayer WSe_2. In bilayer WSe_2, a second WSe_2 layer sits on top of the bottom WSe_2 layer according to the 2H stacking order (Fig. S9a). In the top WSe_2 monolayer, we label the W atom as 4, the lower

(upper) Se atom as 6 (5) (Fig. S9a). The dynamic matric for the interlayer interaction between Se atom 6 and Se atom 2 has the form:

$$D^{26} = \begin{pmatrix} A_6 & 0 & 0 \\ 0 & B_6 & 0 \\ 0 & 0 & C_6 \end{pmatrix}.$$

The dynamic matrices between other atoms can be related to the above six matrices by symmetry. We have adjusted the interaction parameters in these dynamic matrices to fit the DFT results of phonon dispersion [89] and the phonon replica PL data of monolayer WSe_2 [73,78] The best-fit force constants are listed in Table S2. Afterward, we use these force constants to generate the bilayer phonon dispersion and polarization vector in our rigid-ion model. The calculated phonon band structure is presented in **Figure 4.9a**. The polarization vectors of several relevant phonon modes at the M, K, and Q points are shown in **Figure 4.9b**

A_1	B_1	C_1	D_1	E_1	A_2	B_2	C_2	D_2	E_2	A_3	B_3
-10.306	-1.276	-9.823	7.901	7.105	-0.207	-1.849	0.835	0.158	-0.152	-1.712	0.078
C_3	A_4	C_4	A_5	B_5	C_5	D_5	E_5	A_6	B_6	C_6	
1.375	0.520	-3.487	-0.238	-1.412	-0.330	1.019	0.160	-0.0758	-0.0758	-0.19	

Table 4.2. Interaction parameters (in unit of $2e^2/a^2d$) used in our rigid-ion model for bilayer WSe_2. a and d are defined in the text.

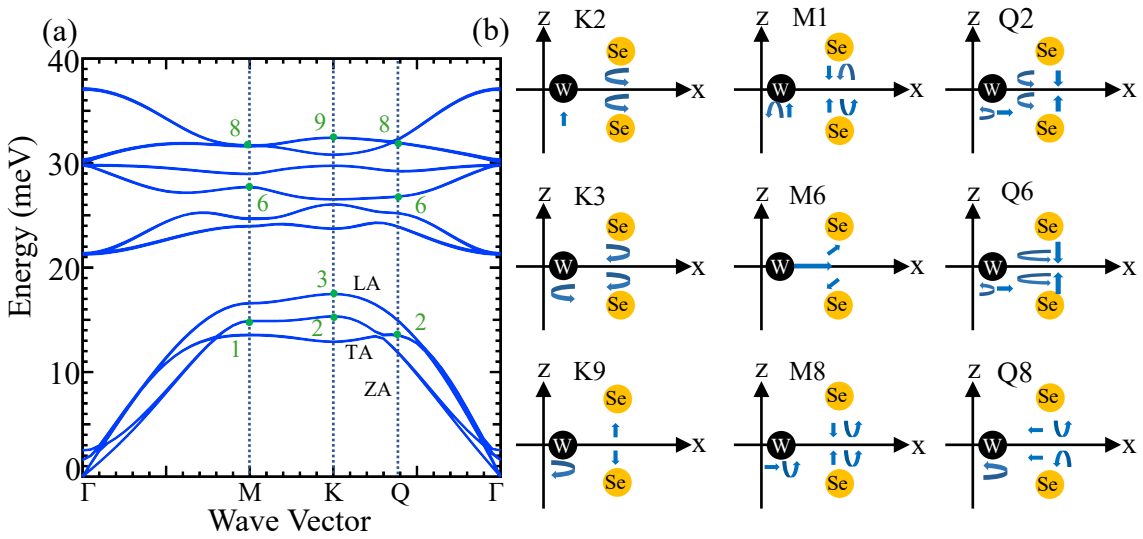

Figure 4.9. The calculated phonon band structure of bilayer WSe_2 (a) Phonon dispersion of bilayer WSe_2 calculated by our rigid-ion model. There are nine pairs of phonon branches (labeled as 1-9 from low to high energy); each pair is nearly degenerate except the interlayer shear and breathing modes. **(b)** Schematic polarization vectors of representative phonon modes at the K, M, Q points. Corresponding labels of the phonon modes are denoted in both panels **(a)** and **(b)**. The straight (curved) arrows denote linear (circular) polarization. The arrow size is proportional to the displacement magnitude. Some atoms at the M and Q points have both linear and chiral polarization components. For simplicity, we only show the polarization configurations of the lower WSe_2 layer, while the configurations of the upper layer are related by inversion symmetry.

4.10 Calculation of one-phonon replica spectra

Besides the field-dependent emission energy shift discussed above, our experiment also reveal phonon replica of the QΓ and QK excitons, which exhibit the same field dependence but are redshifted from the primary emission lines. Here we will present our theoretical calculation of the photon replica spectra.

The phonon replicas can come from one-phonon or multi-phonon emission processes. We first consider the one-phonon process. The emission strength of one-phonon-assisted intervalley exciton recomination is proportional to the transition rate ($P^{(1)}$) according to Fermi's golden rule and the perturbation theory:

$$P_{\mu}^{(1)}(\omega) = \frac{2\pi}{\hbar}\sum_{\alpha}\left|\sum_{\nu}\frac{\langle \omega;\ \Omega_{\alpha}|\widehat{H}_{el}|X_{\nu};\ \Omega_{\alpha}\rangle\langle X_{\nu};\Omega_{\alpha}|\widehat{H}_{ep}|X_{\mu}\rangle}{E_{\mu}-E_{\nu}-\hbar\Omega_{\alpha}+i\gamma}\right|^{2}\delta\left(E_{\mu}-\hbar\Omega_{\alpha}-\hbar\omega\right). \quad (5)$$

Here $\widehat{H}_{el}$ ($\widehat{H}_{ep}$) is the electron-light (electron-phonon) interaction Hamiltonian; ω denotes the frequency of emitted photon; Ω_{α} denotes the frequency of the emitted phonon in mode α; X_{μ} with μ = QΓ or QK denotes the initial intervalley exciton state with energy E_{μ}; X_{ν} denotes the mediating exciton state with energy E_{ν} after the emission of one phonon; γ = 2 meV is a phenomenological broadening energy due to finite carrier lifetime; The associated exciton-phonon scattering strength is defined as:

$$S_{\nu\mu}^{\alpha} = N\left|\frac{\langle X_{\nu};\Omega_{\alpha}|\widehat{H}_{ep}|X_{\mu}\rangle}{E_{\mu}-E_{\nu}-\hbar\Omega_{\alpha}+i\gamma}\right|^{2}. \quad (6)$$

Here N is the number of unit cells in the sample. For bilayer WSe_2, each electronic band is doubly degenerate at zero electric field; here we have summed over the contributions of

the two degenerate states associated with level ν. Moreover, bilayer WSe_2 shows nine pairs of phonon branches, which are here labeled by 1 – 9 from low to high energy; each pair is nearly degenerate (except the interlayer shear and breathing modes) due to the weak interlayer lattice coupling (Fig. S9a). We have summed over the contributions from the two nearly degenerate phonon modes in our results of $S_{\nu\mu}^{\alpha}$.

With $S_{\nu\mu}^{\alpha}$ defined in Eq. (6), the transition rate in Eq. (5) can be simplified as:

$$P_{\mu}^{(1)}(\omega) = \frac{2\pi}{N\hbar}\sum_{\alpha\nu}\left|\left\langle\omega\left|\widehat{H}_{el}\right|X_{\nu}\right\rangle\right|^{2} S_{\nu\mu}^{\alpha}\delta\left(E_{\mu} - \hbar\Omega_{\alpha} - \hbar\omega\right). \qquad (7)$$

To obtain $P_{\mu}^{(1)}$, we need to first calculate $S_{\mu\nu}^{\alpha}$ for the relevant mediating states. We note that the mediating X_{ν} states don't need to bound excitonic states, but they must be momentum-direct excitonic states to have finite optical transitions.

For the X_{QK} initial state, the possible mediating X_{ν} states include the direct excitonic states in the K valley or Q valley (denoted as X_{KK} and X_{QQ} here). For the $X_{Q\Gamma}$ initial state, the possible mediating states X_{ν} include X_{QQ} and $X_{\Gamma\Gamma}$. Here K and Q denote any of the two K points and six Q points; the former (latter) subscript refers to the electron (hole) state. We have calculated $S_{\mu\nu}^{\alpha}$ by DFT for different exciton-phonon scattering processes that emit a phonon. The results are presented in Table S3. The calculated $S_{\nu\mu}^{\alpha}$ values are overall quite small, because all of these one-phonon scattering processes are non-resonant. For all of the listed scattering processes for QΓ and QK initial excitons, the emitted phonons are near the Q, M, and K points (and their symmetry-related points).

Exction-phonon transitions	Phonon momentum	Phonon branch pairs from low to high energy								
		1	**2**	**3**	**4**	**5**	**6**	**7**	**8**	**9**
$X_{Q_1'\mathrm{K}} \rightarrow \mathrm{X}_{\mathrm{KK}}$ $X_{Q_2'\mathrm{K}} \rightarrow \mathrm{X}_{\mathrm{KK}}$ $X_{Q_3'\mathrm{K}} \rightarrow \mathrm{X}_{\mathrm{KK}}$	M	0.093 (13.7)	0. 080 (14.9)	0.053 (16.8)	0.021 (24.1)	**0.221 (24.7)**	**0.113 (27.7)**	0.033 (29.0)	0.087 (31.6)	0.078 (33.7)
$X_{Q_1\mathrm{K}} \rightarrow X_{KK}$ $X_{Q_2\mathrm{K}} \rightarrow X_{KK}$ $X_{Q_3\mathrm{K}} \rightarrow X_{KK}$	Q	**0.237 (8.57)**	0.151 (12.3)	0.082 (12.6)	0.028 (23.1)	**0.458 (25.0)**	**0.511 (26.8)**	0.045 (29.4)	0.015 (31.9)	0.052 (33.7)
$X_{Q_1\mathrm{K}} \rightarrow X_{Q_1\mathrm{Q}_1}$ $X_{Q_2\mathrm{K}} \rightarrow X_{Q_2\mathrm{Q}_2}$ $X_{Q_3\mathrm{K}} \rightarrow X_{Q_3\mathrm{Q}_3}$	Q	**0.172 (8.71)**	0.030 (12.5)	0.066 (12.8)	0.013 (23.1)	0.034 (25.0)	0.050 (26.8)	0.015 (29.4)	0.084 (31.9)	0.034 (33.7)
$X_{Q_1'\mathrm{K}} \rightarrow \mathrm{X}_{Q_1'Q_1'}$ $X_{Q_2'\mathrm{K}} \rightarrow \mathrm{X}_{Q_2'Q_2'}$ $X_{Q_3'\mathrm{K}} \rightarrow \mathrm{X}_{Q_3'Q_3'}$	M	**0.102 (13.7)**	0.062 (14.9)	0.060 (16.8)	0.025 (24.1)	0.036 (24.7)	**0.204 (27.7)**	0.021 (29.0)	0.048 (31.6)	0.034 (31.7)
$X_{Q\Gamma} \rightarrow \mathrm{X}_{\mathrm{QQ}}$ for any Q valley	Q	**0.157 (10.1)**	**0.312 (13.5)**	**0.294 (14.0)**	0.077 (23.5)	0.045 (25.5)	**0.301 (26.6)**	0.048 (29.3)	0.077 (32.0)	**0.128 (32.8)**
$X_{Q\Gamma} \rightarrow \mathrm{X}_{\Gamma\Gamma}$ for any Q valley	Q	**0.313 (10.1)**	0.012 (13.5)	0.010 (14.0)	**0.433 (23.5)**	**0.201 (25.5)**	0.039 (26.6)	0.029 (29.3)	0.021 (32.0)	0.030 (32.8)

Table 4.3. The $S_{\nu\mu}^{\alpha}$ values calculated by DFT for different exciton-phonon scattering processes that emits a phonon. These scattering processes are non-resonant with small $|S_{\nu\mu}^{\alpha}|$ values; the listed $|S_{\nu\mu}^{\alpha}|$ values are multiplied by a factor of 100. The approximate momentum of the emitted phonon is shown in the second column, where K, Q, M refer respectively to one of the K, Q, M (and symmetry-related) points. At each of these points, there are nine pairs of phonon modes, labeled by 1 – 9 from low to high energy; each pair is nearly degenerate. We have summed over the contributions of the two nearly degenerate phonon modes for the $S_{\nu\mu}^{\alpha}$ values listed here. The values for strong transitions are bolded. The number in the parenthese denote the energy of the emitted phonon (in unit of meV).

Our calculation of $S_{\nu\mu}^{\alpha}$ uses the electron-phonon interaction operator [90]:

$$\widehat{H}_{ep} = \sum_{nj\alpha\mathbf{q}} \sqrt{\frac{\hbar}{2NM_j\Omega_{\alpha\mathbf{q}}}} \nabla_j V\left(\mathbf{r} - \mathbf{R_n} - \mathbf{R_j}\right) \cdot \boldsymbol{\epsilon}_j^{\alpha} (a_{\alpha,-\mathbf{q}}^{+} + a_{\alpha\mathbf{q}}) e^{i\mathbf{q}\cdot\mathbf{R_n}} . \quad (8)$$

Here N denotes the number of unit cells in the sample; $\mathbf{R}_n$ denotes the position of a unit cell; $\mathbf{R}_j$ and M_j denote the position and mass of an atom at site j in a unit cell; $V\left(\mathbf{r} - \mathbf{R}_n - \mathbf{R}_j\right)$ denotes the electron-ion interaction potential (screened by valence electrons) centered at $\mathbf{R}_n + \mathbf{R}_j$; $a_{\alpha-\mathbf{q}}^{+}$ ($a_{\alpha\mathbf{q}}$) creates (annihilates) a phonon of mode α and wave-vector -**q** (**q**); $\boldsymbol{\epsilon}_j^{\alpha}$ is the corresponding phonon polarization vector (*i.e.* the displacement unit vector of the atom at site *j*).

By using Eq. (8), we obtain

$$\langle X_\nu; \Omega_\alpha | \widehat{H}_{ep} | X_\mu \rangle = O_{\nu\mu} \sum_j \sqrt{\frac{\hbar}{2NM_j\Omega_\sigma}} \boldsymbol{\Xi}_{\mathbf{q}}^{j} \cdot \boldsymbol{\epsilon}_j^{\alpha}(\mathbf{q}). \quad (9)$$

Here $O_{\nu\mu} = \sum_{\mathbf{k}} \varphi_\nu^*(\mathbf{k})\, \varphi_\mu(\mathbf{k})$ denotes the overlap between the initial and mediating exciton state with respective k-space envelope functions $\varphi_\mu(\mathbf{k})$ and $\varphi_\nu(\mathbf{k})$, which satisfy the normalization condition $\sum_{\mathbf{k}} |\varphi_{\mu,\nu}(\mathbf{k})|^2 = 1$. Using a trial wave function of the form $e^{-\zeta r}$ to describe the exciton real-space envelope function, we obtain $O_{\nu\mu} = 4\zeta_\nu\zeta_\mu / \left(\zeta_\nu + \zeta_\mu\right)^2$, where ζ_ν and ζ_μ are the exponents of the corresponding ν and μ excitons. Since the exciton binding energy is proportional to ζ in a hydrogenic model, we have $O_{\nu\mu} = 4r_{\nu\mu} / \left(1 + r_{\nu\mu}\right)^2$, where $r_{\nu\mu} = E_{b,\mu}/E_{b,\nu}$ is the ratio of binding energies between the μ and ν excitons. Based on this formula, we estimate the $O_{\nu\mu}$ values for various exciton transitions (**Table 4.4**).

In Eq. (9)

$$\Xi_{\mathbf{q}}^{j} = \sum_{n} \langle c_{1,\mathbf{Q}+\mathbf{q}} | \nabla_j V(\mathbf{r} - \mathbf{R}_n - \mathbf{R}_j) e^{i\mathbf{q}\cdot\mathbf{R}_n} | c_{1,\mathbf{Q}} \rangle = \sum_{\mathbf{G}} \mathbf{U}_{\mathbf{q}}^{j}(\mathbf{G}) \langle u_{c1,\mathbf{Q}+\mathbf{q}} | e^{i(\mathbf{q}+\mathbf{G})\cdot\mathbf{r}} | u_{c1,\mathbf{Q}} \rangle \quad (10)$$

is the deformation vector induced by an atomic displacement at site $\mathbf{R}_j$ in each unit cell for the case of electron scattering (c_1 is replaced by v_1 for hole scattering).

Here

$$\mathbf{U}_{\mathbf{q}}^{j}(\mathbf{G}) = \frac{1}{A_c L_c} \sum_{\mathbf{G}} i(\mathbf{q}+\mathbf{G})\, \tilde{V}(\mathbf{q}+\mathbf{G}) e^{-i\mathbf{G}\cdot\mathbf{R}_j}. \quad (11)$$

$\mathbf{G}$ denotes the reciprocal lattice vectors of the crystal; $\tilde{V}_j(\mathbf{q})$ is the Fourier transform of the crystal potential $V(\mathbf{r})$; $|u_{c1,\mathbf{Q}}\rangle$ denotes the periodic part of the Bloch state at $\mathbf{Q}$. In our semi-emipircal calculation, we approximate $\tilde{V}_j(\mathbf{q})$ as

$$\tilde{V}_j(\mathbf{q}) = -\frac{4\pi Z e^2}{q^2} \left[e^{-\left(sqR_{MT}^{j}\right)^2/4} - e^{-\left(s'qR_{MT}^{j}\right)^2/4} \right]. \quad (12)$$

Here Z denotes the valency number (6 for both W and Se); R_{MT}^{j} denotes the muffintin radius of the atom *j*; and *s* denotes an empirical parameter. The first term in Eq. (12) denotes the Coulomb potentential due to the ion with a gaussian charge distribution of radius sR_{MT}^{j}; the second term denotes the screening contribtion of valence electrons described by the same form but with radius $s'R_{MT}^{j}$. We determine the empirical parameters *s* and s' by fitting the deformation potential constant $D_0 = \sum_j \Xi_{\mathbf{0}}^{j} \cdot \boldsymbol{\epsilon}_j$ for electrons coupled to the Γ-point optical phonons. Prior DFT calculations have obtained $D_0 = 2.2\, eV/\text{Å}$ ($3.1\, eV/\text{Å}$) for the electrons in the top valence band at the Γ (K) point of monolayer WSe_2 [91] By fitting these prior results, we obtain $s = 0.41$ and s' = 1.1.

We have used the LASTO codes to compute the integrals in Eq. (10) to obtain the deformation vector $\boldsymbol{\Xi}_{\mathbf{q}}$. Afterward, by using the phonon polarization vectors $\boldsymbol{\epsilon}_j$ obtained by our rigid-ion model, we can calculate the exciton-phonon scattering strength $S_{\nu\mu}^{\alpha}$ according to Eqs. (6) and (9). The caluclated $S_{\nu\mu}^{\alpha}$ values for the relevant transitions are listed in **Table 4.3.**

After we obtain $S_{\nu\mu}^{\alpha}$, we move on to calculate the one-phonon replica spectra by Eq. (7). The calculation involes the electron-light interaction strength $\left|\langle\omega|\hat{H}_{el}|X_{\sigma}\rangle\right|^2$ for the three exciton states (X_{KK}, X_{QQ}, $X_{\Gamma\Gamma}$), averaged over their doubly energy-degenerate states **(as illustrated in Figure 4.5).** We assume that the interaction strength is proportional to the absorption strength of the corrsponding transitions measured by spectroscopic ellipsometry as reported in Ref [92]. The ratios of the X_{KK}, X_{QQ}, $X_{\Gamma\Gamma}$ oscillator strengths are estimated to be 1:2:4. By using these ratios of electron-light interaction strength, combined with the $S_{\nu\mu}^{\alpha}$ values, we obtain the spectra of the one-phonon replica **Figure 4.10.**

Transition	$X_{Q\Gamma} \rightarrow X_{Q'\Gamma}$ $X_{Q\mathrm{K}} \rightarrow X_{Q'\mathrm{K}}$	$X_{Q\mathrm{K}} \rightarrow X_{Q\Gamma}$	$X_{Q\mathrm{K}} \rightarrow X_{KK}$	$X_{Q\mathrm{K}} \rightarrow X_{QQ}$	$X_{Q\Gamma} \rightarrow X_{QQ}$	$X_{Q\Gamma} \rightarrow X_{\Gamma\Gamma}$
$\lvert O_{\nu\mu}\rvert$	1	0.89	0.99	0.83	0.99	0.83

Table 4.4. The absolute value of the overlap integral $O_{\nu\mu}$ for various transitions between two excition states (denoted by μ and ν).

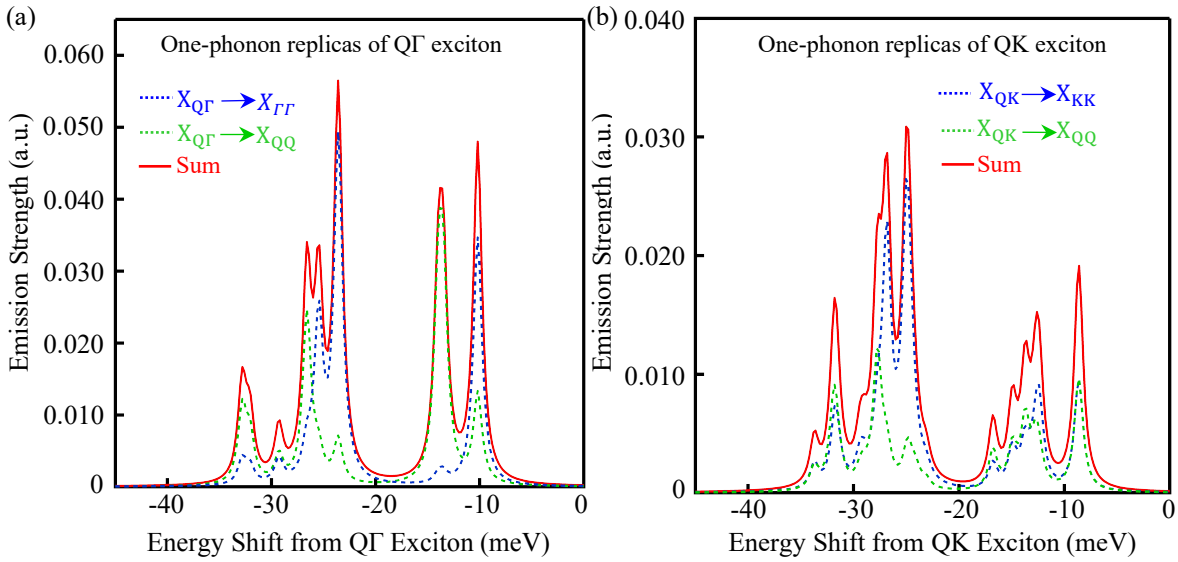

Figure 4.10. Calculated one-phonon replica emission spectra for bilayer WSe_2. (a) One-phonon replica of $X_{Q\Gamma}$. **(b)** One-phonon replica of X_{QK}. We broaden the spectral lines by replacing the delta function in Eq. (7) with a Lorentzian function with half width of 0.5 meV.

Figure 4.10a displays the calculated one-phonon replica spectrum of QΓ exciton. In our plot, we appropriately broaden the spectral lines by replacing the delta function in Eq. (7) with a Lorentizian function with half width of 0.5 meV. The spectrum is contributed by the $X_{Q\Gamma} \rightarrow X_{QQ}$ and $X_{Q\Gamma} \rightarrow X_{\Gamma\Gamma}$ transitions, whose constituent spectra are also shown for comparison. Four prominent peaks are found at ~10, ~14.0, 23.6, and 25.4 meV below the zero-phonon line. The two peaks at ~10 and ~14 meV are close to the broad $X^1_{Q\Gamma}$ replica at 13.0 meV in our experiment. The two peaks at 23.6 and 25.4 meV are close to the $X^2_{Q\Gamma}$ replica at 27.6 meV in experiment. **Figure 4.10b** displays the one-phonon replica spectrum of the QK exciton, which is contributed by the $X_{QK} \rightarrow X_{QQ}$ and $X_{QK} \rightarrow X_{KK}$ transitions.

4.11 Calculation of two-phonon replica spectra

In our calculated one-phonon replica spectra (**Figure 4.10**), the lowest energy peaks are only ~33 meV below the primrary exciton peak due to the limited energy range of single phonons in bilayer WSe_2. This cannot account for the replica peaks that reach redshift energies >40 meV in our expeirment. Therefore, we need to consider higher-order processes to explain our data. The emission strength of two-phonon-assisted intervalley exciton recomination is proportional to the transition rate ($P^{(2)}$) according to Fermi's golden rule in the perturbation theory:

$$P_{\mu}^{(2)}(\omega) = \frac{2\pi}{\hbar}\sum_{\mathbf{q},\alpha,\beta}\left|\sum_{\nu,\sigma}\frac{\langle \omega\,; \Omega_{\alpha\mathbf{q}}, \Omega_{\beta}|\hat{H}_{el}|X_{\sigma}; \Omega_{\alpha\mathbf{q}}, \Omega_{\beta}\rangle\langle X_{\sigma}; \Omega_{\alpha\mathbf{q}}, \Omega_{\beta}|\hat{H}_{ep}|X_{\nu}; \Omega_{\alpha\mathbf{q}}\rangle\langle X_{\nu}; \Omega_{\alpha\mathbf{q}}|\hat{H}_{ep}|X_{\mu}\rangle}{\left(E_{\nu} - E_{\sigma} - \hbar\Omega_{\beta} + i\gamma\right)\left(E_{\mu} - E_{\nu} - \hbar\Omega_{\alpha\mathbf{q}} + i\gamma\right)}\right|^2$$

$$\cdot\, \delta\left(E_{\mu} - \hbar\Omega_{\alpha\mathbf{q}} - \hbar\Omega_{\beta} - \hbar\omega\right). \qquad (13)$$

Here $\hat{H}_{el}$ ($\hat{H}_{ep}$) is the electron-light (electron-phonon) interaction Hamiltonian; ω denotes the frequency of emitted photon; X_{μ} with μ = QΓ or QK denotes the initial intervalley exciton state with energy E_{μ}; X_{ν} (X_{σ}) denotes the first (second) mediating exciton state with energy E_{ν} (E_{σ}); $\Omega_{\alpha\mathbf{q}}$ and Ω_{β} denotes the frequencies of the two emitted phonons in modes α and β; γ = 2 meV is a phenomenological broadening energy due to the finite carrier lifetime.

We note that, in the two-phonon process, the wave vector **q** of the first emitted phonon ($\Omega_{\alpha\mathbf{q}}$) can vary; therefore, we need to sum over states corresponding to different **q**. However, once the wave vector of the first phonon is given, the wave vector of the second phonon

(Ω_β) is determined by the conservation of momentum in the two-phonon scattering process. Therefore Eq. (13) does not contain the sum over the wave vector of the second phonon. For the dominant two-phonon processes, the first phonon is coupled (nearly) resonantly to the exciton states, hence the scattering strength is sensitive to a small variation of the phonon wave vector **q**; but the second phonon is coupled non-resonantly to the exciton states, hence the scattering strength is insensitive to a small variation of the phonon wave vector.

In Eq. (13), the $\widehat{H}_{ep}$ matrix elements in the numerator are insensitive to **q**, but the inverse energy factor in the denominator is sensitive to **q** for the (nearly) resonant process. Therefore, we can simplify the expression by approximating the numerator at a fixed **q** corresponding to the K, Q or Γ point, while suming over the inverse energy factor over **q**. By using this approach and summing over energy-degenerate excitonic transitions, Eq. (13) can be simplified as

$$P_\mu^{(2)}(\omega) = \frac{2\pi}{N\hbar}\sum_{\alpha,\beta}\sum_{\nu,\sigma} f_{\sigma\nu\mu}^{\alpha}\left|\langle\omega|\widehat{H}_{el}|X_\sigma\rangle\right|^2 S_{\sigma\nu}^{\beta} S_{\nu\mu}^{\alpha}\delta\left(E_\mu - \hbar\Omega_\alpha - \hbar\Omega_\beta - \hbar\omega\right). \quad (14)$$

Here $S_{\nu\mu}^{\alpha}$ and $S_{\sigma\nu}^{\beta}$ are the exciton-phonon scattering strengths defined by Eq. (6), evalulated at a fixed **q** that corresponds to the K, Q, or Γ point. The integral over **q** is included in the factor f^{α}, which is given as:

$$f_{\sigma\nu\mu}^{\alpha} \approx \frac{A_c g_{\sigma\nu\mu}^2}{(2\pi)^2}\int_0^\infty d^2q \left|\frac{\Delta_\alpha + i\gamma}{\Delta_\alpha - \frac{\hbar^2q^2}{2m_\nu} + i\gamma}\right|^2 = \frac{A_c g_{\sigma\nu\mu}^2 |\Delta_\alpha + i\gamma|^2 m_\nu}{2\pi\hbar^2\gamma}\left[\frac{\pi}{2} + \tan^{-1}\left(\frac{\Delta_\alpha}{\gamma}\right)\right] \quad (15)$$

Here $A_c = 32.75$ (in atomic unit) is the area of the primitive cell; m_ν is the effective mass of the exction state ν (in unit of free eletron mass); $\Delta_\alpha = E_\mu - E_\nu - \hbar\Omega_\alpha$; $g_{\sigma\nu\mu}$ is a degeneracy factor, which is the number of degenrate transitions emitting the same phonons.

In order to obtain $P_\mu^{(2)}$ in Eq. (14), we need to calculate S for different transitions. Below we will consider the dominant two-phonon transition processes. For both QΓ and QK initial exciton state, the second mediating state should be a momentum-direct exciton state that couples to light. The dominating direct exciton state should be at either K, Q, or Γ valley (or region) (denoted as X_{KK}, X_{QQ}, $X_{\Gamma\Gamma}$, respectively), because they are all strongly coupled to light.

For the QΓ initial exciton, there are four dominating groups of two-phonon pathsways to reach such a direct exciton state. These pathways dominante because they all invovle one nearly resonant mediating state. Below we will describe each group of pathways.

(1) $X_{Q\Gamma} \rightarrow X_{Q'\Gamma} \rightarrow \mathrm{X}_{\mathrm{Q'Q'}}$

In the first group of pathways, $X_{Q\Gamma}$ first transits to $X_{Q'\Gamma}$ through electron scattering from Q to Q′ valley (this is a nearly resonant transition because Q and Q′ valleys are energy degenerate); a phonon with momentum close to **Q** – **Q′** is emitted in this process (this phonon can be near the Q, K or M point, or their symmetry-related points). Afterward, $X_{Q'\Gamma}$ transits to $\mathrm{X}_{Q'Q'}$ through hole scattering from Γ valley to Q′ region; a second phonon with momentum close to –**Q′** is emitted in this process.

Here Q′ denotes any of the six inequivalent Q valleys; therefore this group of pathways includes six different paths via six different Q′ valleys. We note that when Q′ is Q, the $X_{Q\Gamma} \rightarrow X_{Q\Gamma}$ transition is an intravalley transition that emits a phonon near the Γ point.

(2) $X_{Q\Gamma} \rightarrow X_{Q'\Gamma} \rightarrow \mathrm{X}_{\Gamma\Gamma}$

In the second group of pathways, the $X_{Q\Gamma} \rightarrow X_{Q'\Gamma}$ transition is the same as in the first group. In the second transition, $X_{Q'\Gamma}$ transits to $\mathrm{X}_{\Gamma\Gamma}$ through electron scattering from Q′ valley to Γ region in the conduction band; a second phonon with momentum close to $\mathbf{Q'}$ is emitted in this process. This group includes six pathways via six different Q′ valleys.

(3) $X_{Q\Gamma} \rightarrow X_{Q\mathrm{K}} \rightarrow X_{KK}$

In the third group of pathways, $X_{Q\Gamma}$ first transits to X_{QK} through hole scattering from Γ to K valley; a phonon with momentum close to $-\mathbf{K}$ is emitted in this process (this is a resonant or nearly resonant transition because of the samll $X_{Q\Gamma} - X_{QK}$ energy separation). Afterward, X_{QK} transits to X_{KK} through electron scattering from Q to K valley; a second phonon with momentum close to $\mathbf{Q} - \mathbf{K} \approx -\mathbf{Q}$ is emitted. We note that there are two inquivalent K valleys (*i.e.* K and K′ valleys); so, this group includes two pathways via the K or K′ valley.

(4) $X_{Q\Gamma} \rightarrow X_{Q\mathrm{K}} \rightarrow X_{Q\mathrm{Q}}$

In the fourth group of pathways, the $X_{Q\Gamma} \rightarrow X_{Q\mathrm{K}}$ transition is the same as in the third group. In the second transition, $X_{Q\mathrm{K}}$ transits to X_{QQ} through hole scattering from K valley to Q region in the valence band; a second phonon with momentum close to $\mathbf{K} - \mathbf{Q} \approx \mathbf{Q}$ is

emitted in this process. This group includes two pathways via the K or K′ valley. By including all of the four types of pathways above, there are totally 16 (nearly) resonant pathways in the two-phonon process of $X_{Q\Gamma}$.

For the QK initial exciton, there are also four dominating groups of two-phonon pathways to reach a momentum-direct exciton state. These pathways dominante because they all invovle one (nearly) resonant mediating state. Below we will describe each group of pathways.

(1) $X_{Q\mathrm{K}} \rightarrow X_{Q'\mathrm{K}} \rightarrow \mathrm{X_{KK}}$

In the first group of pathways, $X_{Q\mathrm{K}}$ first transits to $X_{Q'\mathrm{K}}$ through electron scattering from Q to Q′ valley; a phonon with momentum close to **Q** – **Q′** is emitted in this process (this is a nearly resonant transition because Q and Q′ valleys are energy degenerate). Afterward, $X_{Q'\mathrm{K}}$ transits to $\mathrm{X_{KK}}$ through electron scattering from Q′ to K valley; a second phonon with momentum close to **Q′** – **K** is emitted in this process. This group includes six different paths via six different Q′ valleys. When Q′ is Q, the $X_{Q\mathrm{K}} \rightarrow X_{Q\mathrm{K}}$ transition is an intravalley transition that emits a phonon near the Γ point.

(2) $X_{Q\mathrm{K}} \rightarrow X_{Q'\mathrm{K}} \rightarrow \mathrm{X}_{Q'Q'}$

In the second group of pathways, the $X_{Q\mathrm{K}} \rightarrow X_{Q'\mathrm{K}}$ transition is the same as in the first group. In the second transition, $X_{Q'K}$ transits to $\mathrm{X}_{Q'Q'}$ through hole scattering from K valley to Q′ region in the valence band; a second phonon with momentum close to **K** – **Q′** is emitted in this process. This group includes six pathways via six different Q' valleys.

(3) $X_{Q\mathrm{K}} \rightarrow X_{Q\Gamma} \rightarrow X_{QQ}$

In the third group of pathways, $X_{Q\mathrm{K}}$ first transits to $X_{Q\Gamma}$ through hole scattering from K to Γ valley; a phonon with momentum close to **K** is emitted in this process (this is a resonant or nearly resonant transition because the $X_{Q\Gamma} - X_{QK}$ energy separation is close to the energy of a phonon). Afterward, $X_{Q\Gamma}$ transits to X_{QQ} through hole scattering from Γ to Q valley; a second phonon with momentum –**Q** is emitted. There is only one pathway in this group.

(4) $X_{QK} \rightarrow X_{Q\Gamma} \rightarrow X_{\Gamma\Gamma}$

In the fourth group of pathways, the $X_{Q\mathrm{K}} \rightarrow X_{Q\Gamma}$ transition is the same as in the third group. In the second transition, $X_{Q\Gamma}$ transits to $X_{\Gamma\Gamma}$ through electron scattering from Q valley to Γ region in the conduction band; a second phonon with momentum close to **Q** is emitted. This group includes only one pathway.

By including all of the four types of pathways above, there are totally 14 dominating pathways in the two-phonon process of X_{QK}.

We note that for all of the above pathways for QΓ and QK initial excitons, the emitted phonons are all near the Γ, Q, M, and K points (and their symmetry-related points). These faciliate our assignment of the phonon replicas.

Exction-phonon transitions	Phonon momentum	Phonon branches from low to high energy								
		1	**2**	**3**	**4**	**5**	**6**	**7**	**8**	**9**
$X_{Q_1\Gamma} \rightarrow X_{Q_1\Gamma}$	Γ	0 (0)	0 (0)	0 (0)	1.933 (21.4)	**5.677 (21.5)**	0.284 (29.9)	0.079 (29.9)	**12.97 (30.2)**	**2.550 (37.1)**
$X_{Q_1K} \rightarrow X_{Q_1K}$	Γ	0 (0)	0 (0)	0 (0)	1.931 (21.4)	**5.670 (21.5)**	0.284 (29.9)	0.078 (29.9)	**18.18 (30.2)**	0.230 (37.1)
$X_{Q_1\Gamma} \rightarrow X_{Q_1'\Gamma}$ $X_{Q_1K} \rightarrow X_{Q_1'K}$	K	**12.22 (13.1)**	0.597 (15.3)	**6.637 (17.6)**	0.156 (23.8)	0.304 (26.0)	**2.936** (26.6)	0.852 (29.7)	0.245 (30.9)	**1.586 (32.4)**
$X_{Q_1\Gamma} \rightarrow X_{Q_2'\Gamma}$ $X_{Q_1\Gamma} \rightarrow X_{Q_3'\Gamma}$ $X_{Q_1K} \rightarrow X_{Q_2'K}$ $X_{Q_1K} \rightarrow X_{Q_3'K}$	Q	**1.168 (10.1)**	**3.310 (13.5)**	0.628 (13.9)	**2.298 (23.6)**	0.204 (25.4)	0.603 (26.6)	0.134 (29.3)	0.321 (32.1)	0.086 (32.8)
$X_{Q_1\Gamma} \rightarrow X_{Q_2\Gamma}$ $X_{Q_1\Gamma} \rightarrow X_{Q_3\Gamma}$ $X_{Q_1K} \rightarrow X_{Q_2K}$ $X_{Q_1K} \rightarrow X_{Q_3K}$	M	**9.813 (13.7)**	**2.762 (14.6)**	0.057 (16.6)	0.007 (24.0)	1.694 (24.9)	**5.293 (27.7)**	0.025 (29.0)	0.830 (31.6)	0.345 (31.8)
$X_{QK} \rightarrow X_{Q\Gamma}$ for any Q valley	K	**20.55 (13.0)**	**124.5 (15.4)**	**106.4 (17.7)**	2.497 (23.7)	4.683 (26.1)	**19.66 (26.6)**	5.135 (29.7)	6.306 (30.8)	0.477 (32.4)
$X_{Q\Gamma} \rightarrow X_{QK}$ for any Q valley	K	0.585 (13.0)	**1.109 (15.4)**	0.338 (17.7)	0.056 (23.7)	0.178 (26.1)	0.811 (26.6)	0.333 (29.7)	0.463 (30.8)	0.041 (32.4)

Table 4.5. The $S_{\nu\mu}^{\alpha}$ values calculated by DFT for different exciton-phonon scattering processes that emit the first phonon in the two-phonon replica. These scattering processes are all (nearly) resonant. The approximate momentum of the emitted phonon is listed in the second column, where K denotes the K or K′ point, Q denotes any of the six Q points, and M denotes any of the three M points (M_1, M_2, M_3) in the Brillouin zone. At each of these points, there are nine pairs of phonon modes, labeled by 1 – 9 from low to high energy; each pair is nearly degenerate. We have summed over the contributions from the two nearly degenerate phonon modes for the $S_{\mu\nu}^{\alpha}$ values listed here. The values for strong transitions are bolded. The number in the parenthese denote the energy of the emitted phonon (in unit of meV).

All of the two-phonon pathways listed above, they consist of two transitions – the first transition emits the first phonon through a (nearly) resonant scattering process, and the second transition emits the second phonon through a non-resonant scattering process. We have calculated the exciton-phonon scattering strength for both transitions. The scattering strength of the first (resonant or nearly resonant) process is listed in **Table 4.5** for all the relevant pathways. The second (non-resonant) process is the same as those in the single-phonon replicas; the scattering strength has been listed in **Table 4.3**. By combining **Tables 4.3 and 4.5**, we can obtain the strength of the two-phonon processes as the product of the strengths of its two constituent one-phonon processes.

After we obtain the two-phonon scattering strength $S_{\sigma\nu}^{\beta}S_{\nu\mu}^{\alpha}$, we calculate the two-phonon replica spectra by using Eq. (14) and the 1:2:4 ratio of $\left|\langle\omega\left|\widehat{H}_{el}\right|X_{\sigma}\rangle\right|^{2}$ for X_{KK}, X_{QQ}, $X_{\Gamma\Gamma}$, similar to our calculation of single-phonon replica. The calculated two-phonon replica spectra for $X_{Q\Gamma}$ and X_{QK} are displayed in Fig. 4.11. In Fig. 4.11, we broaden the spectral lines by replacing the delta function in Eq. (14) with a Lorentizian function with half width of 0.5 meV.

Figure 4.11a displays our calculated two-phonon replica spectra of QΓ exciton. The figure includes the spectra associated with different types of two-phonon pathways as well as the total spectra as their sum. The total spectrum exhibits multiple peaks, which can somewhat account for $X_{Q\Gamma}^{1-5}$ observed in our experiment (see the labels in Fig. S13a). By examining the spectra associated with different types of pathways, we find that the two-phonon replicas of $X_{Q\Gamma}$ are mainly contributed by the $X_{Q\Gamma} \rightarrow X_{Q'\Gamma} \rightarrow X_{Q'Q'}$ and $X_{Q\Gamma} \rightarrow$

$X_{Q\prime\Gamma} \rightarrow X_{\Gamma\Gamma}$ pathways, while the other two types of pathways ($X_{Q\Gamma} \rightarrow X_{QK} \rightarrow X_{KK}$; $X_{Q\Gamma} \rightarrow X_{QK} \rightarrow X_{QQ}$) only contribute weakly. Notably, $X_{Q\Gamma}^{5}$ is contributed significantly by two-phonon paths involving the $X_{Q\Gamma} \rightarrow X_{Q\Gamma}$ intravalley transition, which emits an optical phonon near the Γ point.

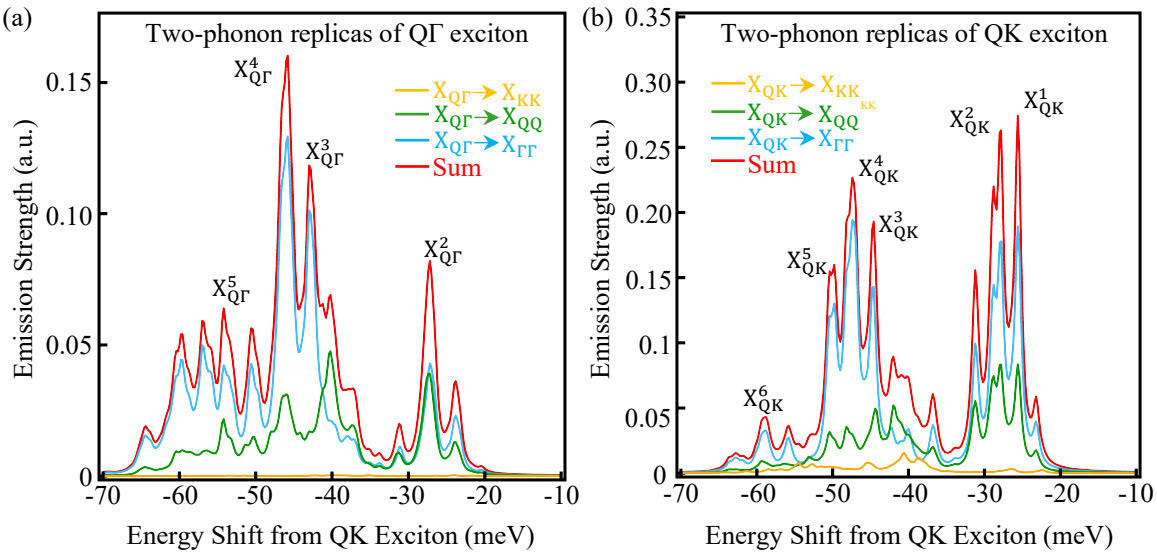

Figure 4.11. Calculated emission spectra of two-phonon replicas for (a) QΓ exciton and **(b)** QK exciton in bilayer WSe_2. The figure displays the spectra associated with different types of two-phonon pathways as well as the total spectra as their sum.

Figure 4.11b displays our calculated two-phonon replicas of QK exciton. The calculated spectrum shows multiple peaks, which can somewhat account for X_{QK}^{1-6} observed in our experiment (see the labels in **Figure 4.11b**). In our theoretical results, the two-phonon replicas for X_{QK} are mainly contributed by the $X_{QK} \rightarrow X_{Q\Gamma} \rightarrow X_{QQ}$ and $X_{QK} \rightarrow X_{Q\Gamma} \rightarrow X_{\Gamma\Gamma}$ pathways. Notably, the $X_{QK} \rightarrow X_{Q\Gamma}$ transition with acoustic phonon emission is strongly resonant when the emitted phonon energy is close to the 18-meV

difference between X_{QK} and $X_{Q\Gamma}$ (**Table 4.5**). Two-phonon processes involving such strongly resonant transitions contribute dominantly to X_{QK}^{1-5} in our result. X_{QK}^{6} is contributed significantly by two-phonon pathways involving the $X_{QK} \rightarrow X_{QK}$ intravalley transition, which emits an optical phonon near the Γ point.

Figure 4.12 displays our calculated total one-phonon and two-phonon replica spectra for both $X_{Q\Gamma}$ and X_{QK}. Remarkably, the calculated spectra show that the two-phonon replicas are overall stronger than the one-phonon replicas. There are two factors leading to this unusual behavior. First, the additional transition in the two-phonon process is a (nearly) resonant process, which has a transition rate close to 100%. Second, there are many more pathways in the two-phonon processes (≥14 paths) than in the one-phonon processes (only two paths); thus, the total transition rate is proprotionally larger in the two-phonon processes.

In **Figures 4.10-12**, we only mildly broaden the spectra by replacing the delta function in Eq. (7) and (14) with a Lorentizian function of half-width 0.5 meV. The theorectical spectra hence display sharp lines. In our experiment, however, the replica peaks are relatively broad. To compare with the experimental results, we plot the theorectial one-phonon, two-phonon, and total replica spectra by using a Lorentizian broadening function of half-width 2 meV. The results, displayed in Fig. 4 of the main paper, agree decently with our experimental spectra.

Our theoretical simulation enables us to give detailed assignments of the observed phonon replicas. In **Table 4.6,** we list the relevant exciton-phonon scattering processes and phonon modes for different replica peaks for both QΓ and QK excitons. Further research is merited to resolve replicas associated with individual scattering process and further understand the rich exciton-phonon coupling physics in bilayer WSe_2.

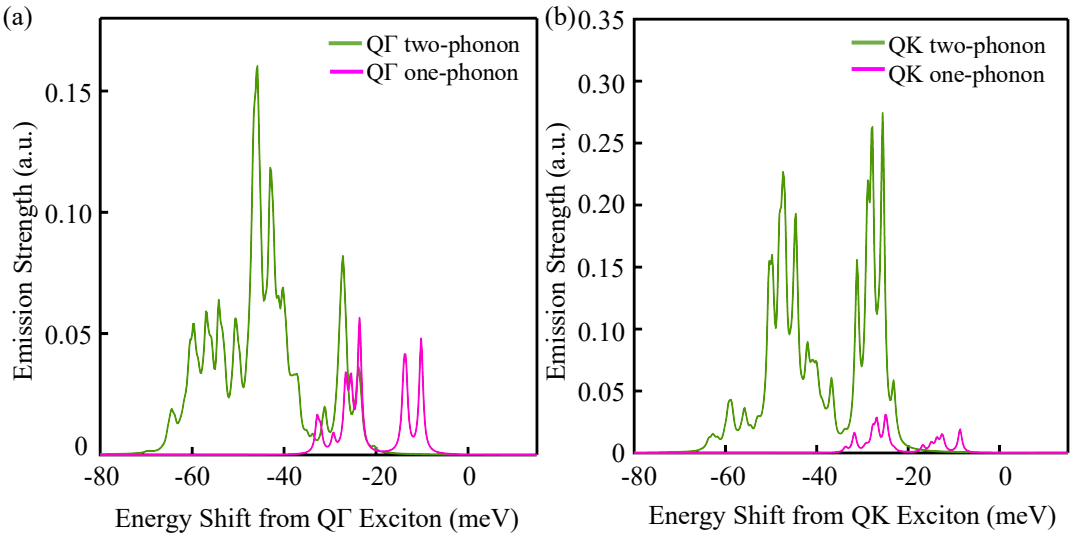

Figure 4.12. Comparison of relative emission strength of one-phonon replica and two-phonon replica for (a) QΓ exciton and **(b)** QK exciton in bilayer WSe_2.

Phonon replicas	Redshift (Expt.) (meV)	Redshift (Theory) (meV)	First transition		Second transition	
			Transition	Phonon mode (energy in meV)	Transition	Phonon mode (energy in meV)
$X^1_{Q\Gamma}$	13.0 ± 2.0	13.5	$X_{Q\Gamma} \rightarrow X_{QQ}$	Q2 (13.5) Q3 (14.0)	–	–
$X^2_{Q\Gamma}$	27.6 ± 1.0	24.0	$X_{Q\Gamma} \rightarrow X_{QK}$	K2 (15.4)	$X_{QK} \rightarrow X_{QQ}$	Q1 (8.57)
		26.3	$X_{Q\Gamma} \rightarrow X_{QK}$	K3 (17.7)	$X_{QK} \rightarrow X_{QQ}$	Q1 (8.57)
		27.2	$X_{Q_1\Gamma} \rightarrow X_{Q_2\Gamma}$ $X_{Q_1\Gamma} \rightarrow X_{Q_3\Gamma}$	M1 (13.8)	$X_{Q_2\Gamma} \rightarrow X_{Q_2Q_2}$ $X_{Q_3\Gamma} \rightarrow X_{Q_3Q_3}$ $X_{Q_2\Gamma} \rightarrow X_{\Gamma\Gamma}$ $X_{Q_3\Gamma} \rightarrow X_{\Gamma\Gamma}$	Q2 (13.5)
$X^3_{Q\Gamma}$	41.7 ± 2.0	40.3	$X_{Q_1\Gamma} \rightarrow X_{Q_2\Gamma}$ $X_{Q_1\Gamma} \rightarrow X_{Q_3\Gamma}$	M1 (13.8)	$X_{Q_2\Gamma} \rightarrow X_{Q_2Q_2}$ $X_{Q_3\Gamma} \rightarrow X_{Q_3Q_3}$ $X_{Q_2\Gamma} \rightarrow X_{\Gamma\Gamma}$ $X_{Q_3\Gamma} \rightarrow X_{\Gamma\Gamma}$	Q5 (26.6)
		40.4	$X_{Q\Gamma} \rightarrow X_{QK}$	K2 (15.4)	$X_{QK} \rightarrow X_{QQ}$	Q5 (25.0)
		42.2	$X_{Q\Gamma} \rightarrow X_{QK}$	K2 (15.4)	$X_{QK} \rightarrow X_{QQ}$	Q6 (26.8)
$X^4_{Q\Gamma}$	45.7 ± 1.2	44.5	$X_{Q\Gamma} \rightarrow X_{QK}$	K3 (17.7)	$X_{QK} \rightarrow X_{QQ}$	Q6 (26.8)
		45.9	$X_{Q_1\Gamma} \rightarrow X_{Q_1'\Gamma}$	K1 (13.1)	$X_{Q_1'\Gamma} \rightarrow X_{Q_1'Q_1'}$	Q9 (32.8)
		46.6	$X_{Q_1\Gamma} \rightarrow X_{Q_2\Gamma}$ $X_{Q_1\Gamma} \rightarrow X_{Q_3\Gamma}$	M1 (13.8)	$X_{Q_2\Gamma} \rightarrow X_{Q_2Q_2}$ $X_{Q_3\Gamma} \rightarrow X_{Q_3Q_3}$ $X_{Q_2\Gamma} \rightarrow X_{\Gamma\Gamma}$ $X_{Q_3\Gamma} \rightarrow X_{\Gamma\Gamma}$	Q9 (32.8)
$X^5_{Q\Gamma}$	57.7 ± 1.4	56.9 59.6	$X_{Q\Gamma} \rightarrow X_{Q\Gamma}$	Γ8 (30.3)	$X_{Q\Gamma} \rightarrow X_{QQ}$	Q6 (26.6) Q7(29.3)

Phonon replicas	Redshift (Expt.) (meV)	Redshift (Theory) (meV)	First transition		Second transition	
			Transition	Phonon mode (energy in meV)	Transition	Phonon mode (energy in meV)
X^1_{QK}	28.8 ± 1.8	25.6	$X_{QK} \rightarrow X_{Q\Gamma}$	K2 (15.4)	$X_{Q\Gamma} \rightarrow X_{\Gamma\Gamma}$	Q1 (10.2)
		27.9	$X_{QK} \rightarrow X_{Q\Gamma}$	K3 (17.7)	$X_{Q\Gamma} \rightarrow X_{\Gamma\Gamma}$	Q1 (10.2)
		28.9	$X_{QK} \rightarrow X_{Q\Gamma}$	K2 (15.4)	$X_{Q\Gamma} \rightarrow X_{QQ}$	Q2 (13.5)
X^2_{QK}	32.4 ± 1.2	31.2	$X_{QK} \rightarrow X_{Q\Gamma}$	K3 (17.7)	$X_{Q\Gamma} \rightarrow X_{\Gamma\Gamma}$	Q2 (13.5)
X^3_{QK}	41.9 ± 1.8	42.0	$X_{QK} \rightarrow X_{Q\Gamma}$	K2 (15.4)	$X_{Q\Gamma} \rightarrow X_{QQ}$	Q6(26.6)
X^4_{QK}	46.2 ± 1.8	47.4	$X_{QK} \rightarrow X_{Q\Gamma}$	K2 (15.4)	$X_{Q\Gamma} \rightarrow X_{\Gamma\Gamma}$	Q8 (32.0)
		44.3	$X_{QK} \rightarrow X_{Q\Gamma}$	K3 (17.7)	$X_{Q\Gamma} \rightarrow X_{\Gamma\Gamma}$	Q6 (26.6)
X^5_{QK}	49.1 ± 1.6	48.2	$X_{QK} \rightarrow X_{Q\Gamma}$	K2 (15.4)	$X_{Q\Gamma} \rightarrow X_{\Gamma\Gamma}$	Q9 (32.8)
		50.5	$X_{QK} \rightarrow X_{Q\Gamma}$	K3 (17.7)	$X_{Q\Gamma} \rightarrow X_{\Gamma\Gamma}$	Q9 (32.8)
X^6_{QK}	58.3 ± 2.0	59.4	$X_{QK} \rightarrow X_{QK}$ $X_{QK} \rightarrow X_{Q\Gamma}$	Γ8 (30.3) K6 (26.6)	$X_{QK} \rightarrow X_{KK}$ $X_{Q\Gamma} \rightarrow X_{QQ}$	M7 (29.0) Q9 (32.8)

Table 4.6. Dominant transitions and phonon modes involved in different replica features for QΓ and QK excitons in bilayer WSe_2. All the listed energies are in unit of meV. The errors of the experimental energies represent a confidence interval of about 9.

Chapter 5

Defect-mediated coherent excitons in bilayer WSe_2

5.1 Introduction

Coherent excitons, formed by quantum superposition of two or more different excitonic states, can exhibit novel properties that cannot be found in the component excitons. For example, in monolayer WSe_2, while the K-valley and K'-valley excitons are coupled to light with right-handed and left-handed circular polarization, respectively, their coherent excitons can also be coupled to linearly polarized light. In heterobilayers of transition metal dichalcogenides (TMDs, *e.g.,* MoS_2, WSe_2), the interaction between intralayer and interlayer excitons can form coherent excitons with hybridized layer configuration. By controlling the coherent coupling between excitons, one may finely tune the properties of coherent excitons for novel applications in quantum optics and quantum information.

Throughout the many decades of exciton research, different types of coherent excitons have been observed, but they all share one common feature – they are formed by excitons with the same center-of-mass (CM) momentum (momentum-matched excitons). Indeed, in a perfect crystal with no defect, where the crystal momentum is a good quantum number, it is impossible for excitons with different CM momenta (momentum-mismached excitons) to form a coherent eigen state with a well-defined momentum. For momentum-mismatched excitons to form coherent eigen states, one must break the crystal translation symmetry (i.e. introduce defects). While defect-related trapping and scattering of exctions are common in

semiconductors, defect-mediated coherent coupling of momentum-mismatched excitons has never been reported. As coherent excitons are usually delicate, we can perceive that defect-mediated coherent excitons are even more delicate with tiny signal and extremely fast decoherence. However, if defect-mediated coherent coupling of excitons can be realized, it can strongly enrich the physics and application of coherent excitons. For instance, by modulating the defect density and defect species, one may effectively control the properties of coherent excitons.

5.2 Experimental results

By using the second-order energy derivative of reflectanc contrast, we can resolve two weak features arising from defect-mediated optical coupling of the QK and Q'K intervalley excitons in bilayer WSe_2. Under the application of an out-of-plane electric field, the QK and Q'K excitons undergo Stark splitting, couple with each other and also with the nearby KK intravalley excitons. On the one hand, we observe similar Stark shift between the QK and Q'K excitons, which contradicts against their different dipole moment; this observation suggests level repulsion between them. On the other hand, we observe prominent level repulsion between the Q'K exciton and the KK excitons, signifying coherent coupling between these two types of excitons with different CM momenta. We can quantitatively simulate the results by a model that considers defect-mediated coherent coupling between the QK, Q'K, and KK excitons. The good agreement between experiment and theory strongly support the emergence of defect-mediated coherent states in bilayer WSe_2.

Bilayer WSe_2 crystals has the 2H-stacking order and exhibit a hexagonal Brilloune zone, **Figure 5.1a,b**. Both the conduction and valence bands exhibit valleys at two inequivalent corners (K, K'points) of the Brillouin zone. The conduction band also exhibits valleys at six interior points, including three Q points and three Q' points. The three Q (or Q') points are related to one another by three-fold rotational symmetry, and the two sets of Q and Q' points are related to each other by time-reversal symmetry. As we will show later, the presence of multiple valleys are crucial to produce strong excitonic coupling effect in the system.

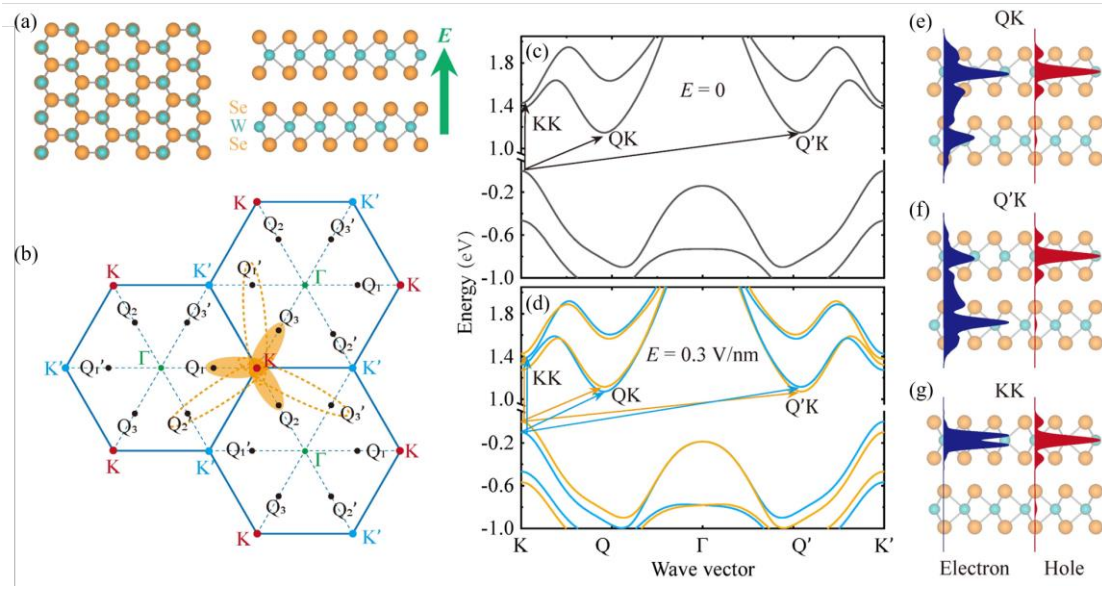

Figure 5.1 Intravalley and intervalley excitons in bilayer WSe_2. (a). Top and side views of bilayer WSe_2 crystal structure. **(b).** KQ and KQ' intervalley excitons in the Brillouin zone. **(c)** Band structure with no external electric field. **(d)** Band structure at a finite out-of-plane electric field. The dominant spin of the related bands is denoted by blue (red) color for the spin-up (spin-down) configuration. (**e-g)** electron and hole density distribution along the out-of-plane direction for the KQ, KQ', and KK exciton.

The multi-valley configuration give rise to different types of excitons, including three QK excitons, three Q'K excitons and one KK exciton; each of these seven excitons have different CM momentum with each other (the time-reversal Q'K', QK' and K'K'excitons can be handled trivially by including a two-fold energy degenercy). Although the QK and Q'K transitions appear to have the same energy in the electron band structure **Figure 5.1c,** their actual transition energies are different because the QK and Q'K excitons have different binding energies due to their different electron-hole distribution on the two WSe_2 layers **Figure 5.1e-f.** By applying an out-of-plane electric field to break the inversion symmetry of the crystal, each conduction and valence band is split into two subbands with dominant spin-up or spin-down configurations **Figure 5.1d.** By using the density functional theory (DFT), we have calculated the electron and hole density along the vertical direction for the QK, Q'K and KK excitons **Figure 5.1e-g.** From the density distribution, we obtain the interlayer dipole moment to be $p_{QK} = 0.200\ e \cdot nm$ for QK exciton, $p_{Q'K} = 0.417\ e \cdot nm$ for Q′K exciton, and $p_{KK} = 0$ for KK exciton. From the calculated dipole, we expect no Stark shift for the KK exciton, finite but markedly different Stark shifts for the QK and Q'K excitons.

To experimental exploring these different excitons, we have fabricated dual-gate bilayer WSe_2 devices encapsulated by boron nitride (BN). We use thin graphite as the gate and contact electrodes to enhance the device performance.

By adjusting the ratio of the voltages on the top and bottom gates (V_t/V_b) according to their different capacitance, we can apply a vertical electric field on bilayer WSe_2 without injecting net charges into the sample.

For each electric field, we measure the reflectance contrast of bilayer WSe_2 ($\Delta R/R$) and further perform the second-order energy derivative [$d^2(\Delta R/R)/dE^2$] to sharpen the weak features.

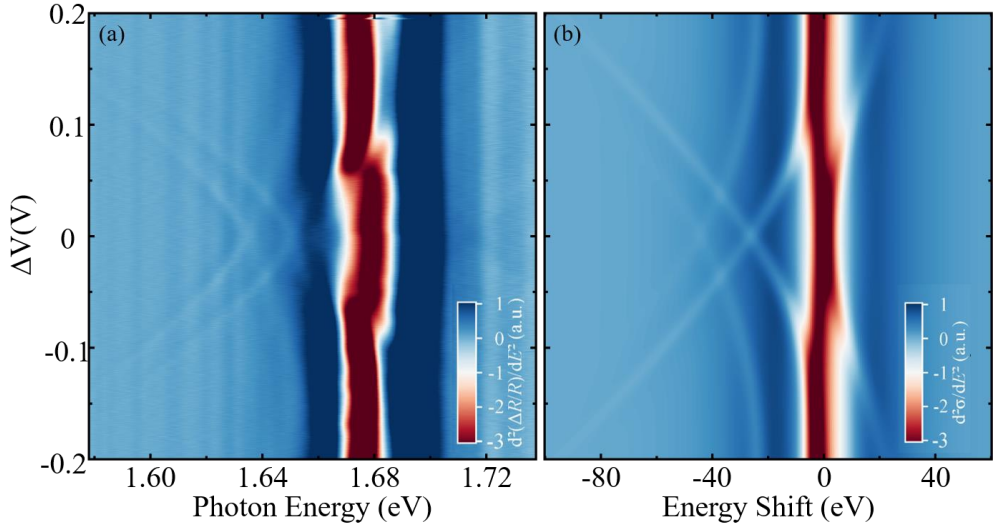

Figure 5.2 Defect-mediated coherent excitons in bilayer WSe_2 (a) The experimental electric-field-dependent map of the second-order energy derivative of reflectance contrast for bilayer WSe_2. The sample remains charge neutral at different electric field. **(b)** Theoretical simulation of the second derivative of conductivity for bilayer WSe_2 under varying electric field.

Figure 5.2 displays the second-order differential reflectance contrast map of a bilayer WSe_2 device at varying electric field. The strong feature at ~1.672 eV corresponds to the KK intravalley exciton. It exhibits no Stark shift as expected. Remarkably, at 23 meV and 38 meV below the KK feature, we observed two sets of X-shape lines. They are quite weak,

but clearly discernable in our map. We assign them as the QK and Q'Kexcitons for two reasons. First, their energy lie at the anticipated energy range of the QK and QK' excitons. Seocnd, their Stark shifts are comparable to the expected Stark shifts of the QK and QK' excitons. Third, their weak optical signals match the expectation for momentum-indirect excitons. As Q′K exciton has smaller binding energy than the QK exciton?, we assign the lower feature at 1.634 meV as the QK exciton and the higher feature at 1.649 meV as the Q'K exciton. In a perfect cyrtsal, momentum indirect excitons, such as the QK and Q'K excitons, are strictly forbidden from coupling with light by the conservation of momentum. Therefore, the weak optical signals of QK and Q'K excitons in our map must come from defect-assisted optical transitions of these two excitons. The role of defect is thus evidenced and crucial in our observation.

One prominent feature in the map is the crossover between the KQ' lines and the KK line. We observe clear signature of level repulsion between the KQ' and KK excitons. As Q'K and KK excitons have different CM momenta, they cannot be coupled by the Coulomb interaction in a pefect crystal. The observed level repulsion can only occur when the crystal translation symmetry is broken (i.e. in the presence of defects).

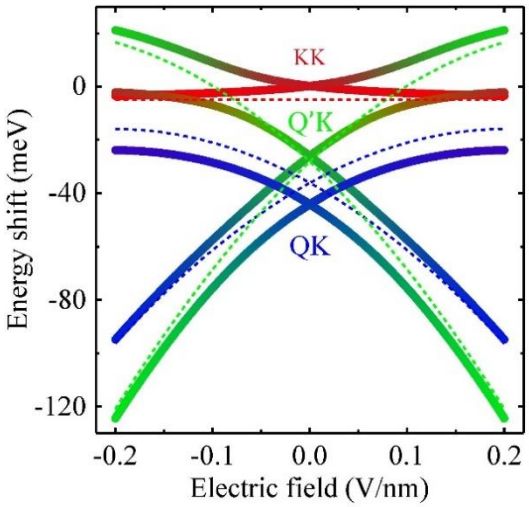

Figure 5.3 Theoretical analysis of coherent exciton coupling in bilayer WSe_2. The dotted lines show the QK, Q'K, and KK exciton energies under varying out-of-plane electric field without considering any coherent coupling between them. The solid lines show the energies of the hybridized exciton states between the QK, Q'K, and KK excitons under defect-mediated coherent coupling.

5.3 KK interlayer exciton

To explain the two X-shape features observed below the bright exciton (A^0) in the differential reflectance contrast map, we first consider the coupled states between the interlayer KK and K′K′ excitons (both with the hole localized in the top layer). These two excitons can form symmetric and antisymmetric combinations. The symmetric one corresponds to the spin-singlet bright exciton; the antisymmetric one, together with two dark interlayer K′K and KK′ excitons (both with hole localized in the top layer), becomes the three energy-degenerate states within the spin triplet. Only the spin-singlet is optically active but very weak due to the interlayer nature and strong localization of both electron and hole in the K valley (see **Figure 5.4a**). There is another optically allowed spin-singlet

interlayer KK exciton (with hole localized in the right layer). The two spin-singlet excitons are degenerate in energy by symmetry, and the electron-hole exchange (EHX) coupling between them is negligible due the spatial separation. Thus, the assignment of KK excitons cannot explain the two pairs of interlayer excitons (with energy spacing of 16 meV) as observed experimentally. Furthermore, the exciton-exciton coupling between the interlayer KK exciton with intralayer KK exciton through the EHX interaction will be very small, since the overlap of electron wavefunction in c1 band in the right layer with that in v1 band in the left layer is negligibly small. Due to the weak exciton binding in this interlayer KK exciton, the peak position is expected to be above the A^0 exciton. This actually agrees with the weak cross-like feature slightly above A^0 observed experimentally.

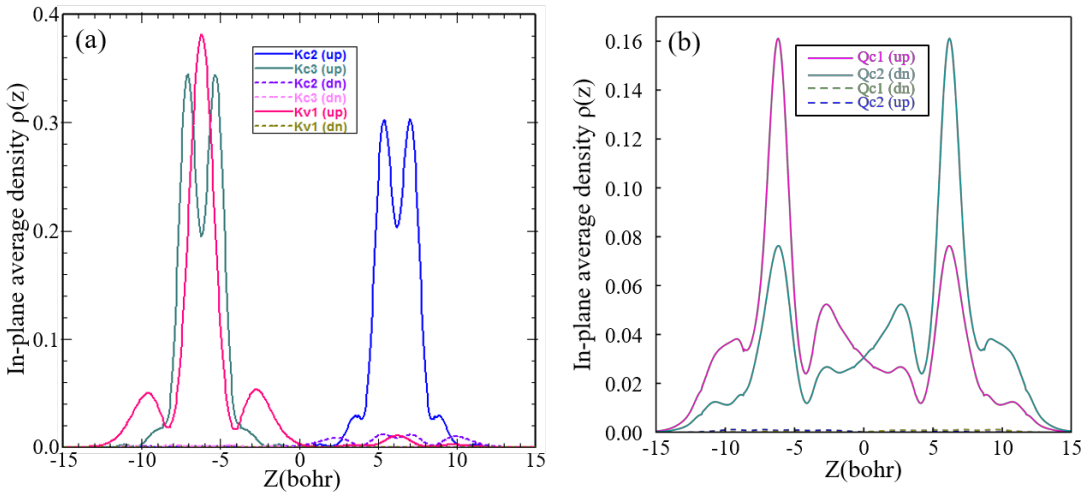

Figure 5.4 Illustration of in-plane averaged electron density of bilayer WSe_2 in (a) top valence band (K_{v1}), the second conduction band (K_{c2}) and the third conduction band (K_{c3}) at K point and **(b)** first conduction band (Q_{c1}) and the second conduction band (Q_{c2}) at Q point.

5.4 Intervalley-coupling induced optically active excitons

For bilayer WSe_2, the conduction-band minimum occurs at the Q point and the valence-band maximum occurs at the K point [68]. For defect-free samples, only momentum-direct excitons are optically active. However, typical samples usually have some number of defects that can induce intervalley scattering to cause optically active indirect excitons, especially when there are degenerate valleys such as the Q valleys. The electron density distributions in the lowest two degenerate conduction bands at Q point are shown in **Figure 5.4b.** We note that the charge density in second conduction band (Q'_{c2}) at Q' point is the same as that in band Q_{c2} (green curve in 5.4b) with a spin flip. For QK ($Q'K$) exciton, the electron will be in the first (second) conduction band in the Q (Q') valley with ~2/3 (1/3) charge density in the left layer. Although these excitons are indirect, they can become optically active with the assistance of defect scattering.

For the optical transitions starting from a spin-up electron in the top valence band ($v1$), We shall consider QK intralayer exciton (with hole localized in the left layer and $Q'K'$ (with hole localized either in the right layer) as well as $Q'K$ interlayer exciton. There is another set of excitons for the optical transitions starting from a spin-down electron in the valence band, which have the same exciton envelope function as the spin-up case due to the time-reversal symmetry. Let's first consider the spin-up case. Namely, the hole in these four excitons considered will be created from the top valence band with spin up either in the K valley (with charge density primarily localized in the left layer) or in the K' valley (with charge density primarily localized in the right layer). Because the energies of these four excitons are close, the coupling between them due to Coulomb interaction can be

significant. Here, we consider the intervalley-coupling induced optically active excitons associated with electron in the Q (Q′) valley and hole in the K (K′) valley. See **Figure 5.5** for illustration.

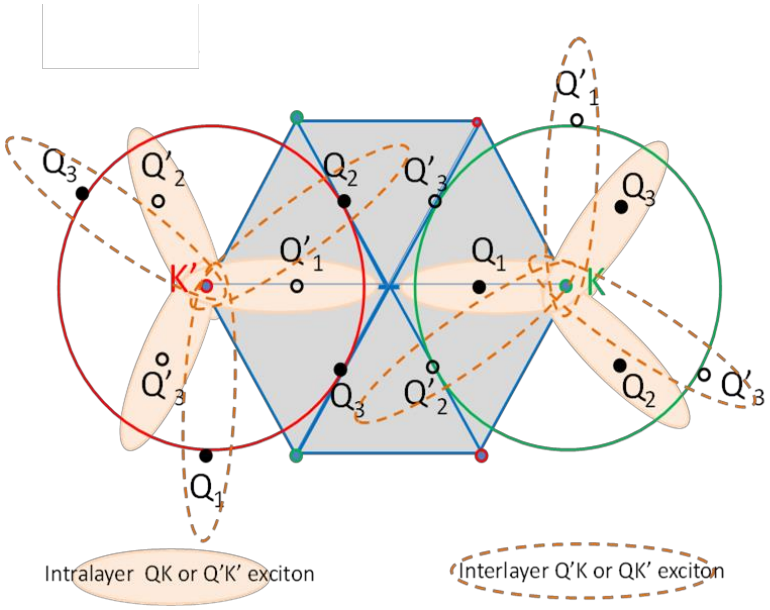

Figure 5.5 Illustration of coherently coupled QK intralayer and Q′K interlayer excitons induced by defect scattering in bilayer WSe_2.

Chapter 6
Conclusion

In this dissertation we have presented our findings in two major chapters, we summarize these here.

First, we fabricated dual-gated bilayer WSe_2 devices with hexagonal boron nitride (BN) encapsulation by micro-mechanical exfoliation and co-lamination of thin crystals. In this process, we use thin graphite as the gate and contact electrodes to enhance the device performance. By adjusting the ratio of the voltages on the top and bottom gates (V_t/V_b) according to their different capacitance, we can apply a vertical electric field on bilayer WSe_2 without injecting net charges into the sample. We aimed to investigate the intervalley excitons in bilayer WSe_2 system under the application of out-of-plane electric field. By using ultraclean bilayer WSe_2 devices, we were able to directly resolve the QΓ exciton emission and conduct a complete comparative electric-field-dependent studies between the two dominated emissions in bilayer WSe_2: QΓ and QK excitons. Remarkably, we observe that the QΓ exciton is located at ~18 meV below the QK exciton; this reveals considerably stronger binding of the QΓ exciton than the QK exciton. We also observe strong Stark effects in both excitons under an out-of-plane electric field, but the QΓ Stark shift is significantly weaker than the QK shift.

Moreover, both excitons exhibited strong two-phonon replicas, which are comparable to or even brighter than the one-phonon replicas and outshine the primary emission. We simulated the replica spectra by comprehensive theoretical calculation. Our

results revealed the existence of numerous two-phonon scattering processes with (nearly) resonant exciton-phonon scattering, which led to unusually strong two-phonon replicas in bilayer WSe_2.

Second, we conducted reflectance contrast spectroscopy in bilayer WSe_2. Using the second-order energy derivative of reflectance, we observed two weak features arising from defect-mediated optical coupling of the QK and Q′K intervalley excitons in bilayer WSe_2. Under the application of an out-of-plane electric field, the QK and Q′K excitons coupled with each other and also with the nearby KK intravalley excitons. On the one hand, we observed similar Stark shift between the QK and Q′K excitons, which contradicts their different dipole moments; this observation suggests level repulsion between them. On the other hand, we observed prominent level repulsion between the Q′K exciton and the KK excitons, signifying coherent coupling between these two types of excitons with different centre of mass momenta. We quantitatively simulated the results by a model that considers defect-mediated coherent coupling between the QK, Q′K, and KK excitons.

To conclude, our novel results demonstrate bilayer WSe_2 to be an exceptional valleytronics material, with switchable intervalley excitons and strong two-phonon scattering, which hardly exist in other atomically thin semiconductors. In addition, the emergence of coherent states between momentum-mismatched excitons provides important insight into the role of defects in coherent excitonic coupling in semiconductors.

Bibliography

[1] B. Partoens and F. M. Peeters, *From Graphene to Graphite: Electronic Structure around the K Point*, Phys. Rev. B - Condens. Matter Mater. Phys. **74**, 1 (2006).

[2] A. S. Mayorov, R. V. Gorbachev, S. V. Morozov, L. Britnell, R. Jalil, L. A. Ponomarenko, P. Blake, K. S. Novoselov, K. Watanabe, T. Taniguchi, and A. K. Geim, *Micrometer-Scale Ballistic Transport in Encapsulated Graphene at Room Temperature*, Nano Lett. **11**, 2396 (2011).

[3] S. V. Morozov, K. S. Novoselov, M. I. Katsnelson, F. Schedin, D. C. Elias, J. A. Jaszczak, and A. K. Geim, *Giant Intrinsic Carrier Mobilities in Graphene and Its Bilayer*, Phys. Rev. Lett. **100**, 11 (2008).

[4] C. Lee, X. Wei, J. W. Kysar, and J. Hone, *Measurment of the Elastic Properties and Intrinsic Strength of Monolayer Graphene*, Science (80-.). **321**, 385 (2008).

[5] F. Liu, P. Ming, and J. Li, *Ab Initio Calculation of Ideal Strength and Phonon Instability of Graphene under Tension*, Phys. Rev. B - Condens. Matter Mater. Phys. **76**, 1 (2007).

[6] A. A. Balandin, *Thermal Properties of Graphene and Nanostructured Carbon Materials*, Nat. Mater. **10**, 569 (2011).

[7] R. R. Nair, P. Blake, A. N. Grigorenko, K. S. Novoselov, T. J. Booth, T. Stauber, N. M. R. Peres, and A. K. Geim, *Fine Structure Constant Defines Visual Transparency of Graphene*, Science (80-.). **320**, 1308 (2008).

[8] J. Moser, A. Barreiro, and A. Bachtold, *Current-Induced Cleaning of Graphene*, Appl. Phys. Lett. **91**, 1 (2007).

[9] J. A. Venables, G. D. T. Spiller, and M. Hanbucken, *Nucleation and Growth of Thin Films*, Reports Prog. Phys. **47**, 399 (1984).

[10] O. A. Shenderova, V. V. Zhirnov, and D. W. Brenner, *Carbon Nanostructures*, Crit. Rev. Solid State Mater. Sci. **27**, 227 (2002).

[11] D. Tomaânek, W. Zhong, and E. Krastev, *Stability of Multishell Fullerenes*, Phys. Rev. B **48**, 15461 (1993).

[12] R. Setton, *Carbon Nanotubes - II. Cohesion and Formation Energy of Cylindrical Nanotubes*, Carbon N. Y. **34**, 69 (1996).

[13] A. K. Geim and K. S. Novoselov, *The Rise of Graphene PROGRESS*, Nat. Mater. **6**, 183 (2007).

[14] K. S. Novoselov, Z. Jiang, Y. Zhang, S. V. Morozov, H. L. Stormer, U. Zeitler, J. C. Maan, G. S. Boebinger, P. Kim, and A. K. Geim, *Room-Temperature Quantum Hall Effect in Graphene*, Science (80-.). **315**, 1379 (2007).

[15] E. Fradkin, *Critical Behavior of Disordered Degenerate Semiconductors. II. Spectrum and Transport Properties in Mean-Field Theory*, Phys. Rev. B **33**, 3263 (1986).

[16] A. M. J. Schakel, *Relativistic Quantum Hall Effect*, Phys. Rev. D **43**, 1428 (1991).

[17] J. González, F. Guinea, and M. A. H. Vozmediano, *Unconventional Quasiparticle Lifetime in Graphite*, Phys. Rev. Lett. **77**, 3589 (1996).

[18] K. S. Novoselov, A. Mishchenko, A. Carvalho, and A. H. Castro Neto, *2D Materials and van Der Waals Heterostructures*, Science (80-.). **353**, (2016).

[19] P. Cudazzo, I. V. Tokatly, and A. Rubio, *Dielectric Screening in Two-Dimensional Insulators: Implications for Excitonic and Impurity States in Graphane*, Phys. Rev. B - Condens. Matter Mater. Phys. **84**, 1 (2011).

[20] A. Ramasubramaniam, *Large Excitonic Effects in Monolayers of Molybdenum and Tungsten Dichalcogenides*, Phys. Rev. B - Condens. Matter Mater. Phys. **86**, 1 (2012).

[21] D. Y. Qiu, F. H. Da Jornada, and S. G. Louie, *Optical Spectrum of MoS2: Many-Body Effects and Diversity of Exciton States*, Phys. Rev. Lett. **111**, 1 (2013).

[22] A. Chernikov, T. C. Berkelbach, H. M. Hill, A. Rigosi, Y. Li, O. B. Aslan, D. R. Reichman, M. S. Hybertsen, and T. F. Heinz, *Exciton Binding Energy and Nonhydrogenic Rydberg Series in Monolayer WS2*, Phys. Rev. Lett. **113**, 1 (2014).

[23] J. Feldmann, G. Peter, E. O. Göbel, P. Dawson, K. Moore, C. Foxon, and R. J. Elliott, *Linewidth Dependence of Radiative Exciton Lifetimes in Quantum Wells*, Phys. Rev. Lett. **59**, 2337 (1987).

[24] A. Splendiani, L. Sun, Y. Zhang, T. Li, J. Kim, C. Chim, G. Galli, and F. Wang, *Emerging Photoluminescence in Monolayer*, Nano Lett. **10,1271**, (2010).

[25] K. F. Mak, C. Lee, J. Hone, J. Shan, and T. F. Heinz, *Atomically Thin MoS 2 : A New Direct-Gap Semiconductor*, Phys. Rev. Lett. **105,136805**, 2 (2010).

[26] T. Cheiwchanchamnangij and W. R. L. Lambrecht, *Quasiparticle Band Structure Calculation of Monolayer, Bilayer, and Bulk MoS 2*, Phys. Rev. B - Condens. Matter Mater. Phys. **85**, 1 (2012).

[27] L. Britnell, R. V. Gorbachev, R. Jalil, B. D. Belle, F. Schedin, M. I. Katsnelson, L.

Eaves, S. V. Morozov, A. S. Mayorov, N. M. R. Peres, A. H. Castro Neto, J. Leist, A. K. Geim, L. A. Ponomarenko, and K. S. Novoselov, *Electron Tunneling through Ultrathin Boron Nitride Crystalline Barriers*, Nano Lett. **12**, 1707 (2012).

[28] G. H. Lee, Y. J. Yu, C. Lee, C. Dean, K. L. Shepard, P. Kim, and J. Hone, *Electron Tunneling through Atomically Flat and Ultrathin Hexagonal Boron Nitride*, Appl. Phys. Lett. **99**, 1 (2011).

[29] C. R. Dean, A. F. Young, I. Meric, C. Lee, L. Wang, S. Sorgenfrei, K. Watanabe, T. Taniguchi, P. Kim, K. L. Shepard, and J. Hone, *Boron Nitride Substrates for High-Quality Graphene Electronics*, Nat. Nanotechnol. **5**, 722 (2010).

[30] O. Lopez-Sanchez, D. Lembke, M. Kayci, A. Radenovic, and A. Kis, *Ultrasensitive Photodetectors Based on Monolayer MoS 2*, Nat. Nanotechnol. **8**, 497 (2013).

[31] J. S. Ross, P. Klement, A. M. Jones, N. J. Ghimire, J. Yan, D. G. Mandrus, T. Taniguchi, K. Watanabe, K. Kitamura, W. Yao, D. H. Cobden, and X. Xu, *Electrically Tunable Excitonic Light-Emitting Diodes Based on Monolayer WSe2 p-n Junctions*, Nat. Nanotechnol. **9**, 268 (2014).

[32] R. Cheng, D. Li, H. Zhou, C. Wang, A. Yin, S. Jiang, Y. Liu, Y. Chen, Y. Huang, and X. Duan, *Electroluminescence and Photocurrent Generation from Atomically Sharp WSe2/MoS2 Heterojunction p-n Diodes*, Nano Lett. **14**, 5590 (2014).

[33] A. Pospischil, M. M. Furchi, and T. Mueller, *Solar-Energy Conversion and Light Emission in an Atomic Monolayer p-n Diode*, Nat. Nanotechnol. **9**, 257 (2014).

[34] R. S. Sundaram, M. Engel, A. Lombardo, R. Krupke, A. C. Ferrari, and M. Steiner,

Electroluminescence in Single Layer MoS 2, (2013).

[35] F. Withers, O. Del Pozo-Zamudio, A. Mishchenko, A. P. Rooney, A. Gholinia, K. Watanabe, T. Taniguchi, S. J. Haigh, A. K. Geim, A. I. Tartakovskii, and K. S. Novoselov, *Light-Emitting Diodes by Band-Structure Engineering in van Der Waals Heterostructures*, Nat. Mater. **14**, 301 (2015).

[36] G. Bin Liu, D. Xiao, Y. Yao, X. Xu, and W. Yao, *Electronic Structures and Theoretical Modelling of Two-Dimensional Group-VIB Transition Metal Dichalcogenides*, Chem. Soc. Rev. **44**, 2643 (2015).

[37] T. Jiang, H. Liu, D. Huang, S. Zhang, Y. Li, X. Gong, Y. R. Shen, W. T. Liu, and S. Wu, *Valley and Band Structure Engineering of Folded MoS 2 Bilayers*, Nat. Nanotechnol. **9**, 825 (2014).

[38] E. Cappelluti, R. Roldán, J. A. Silva-Guillén, P. Ordejón, and F. Guinea, *Tight-Binding Model and Direct-Gap/Indirect-Gap Transition in Single-Layer and Multilayer MoS2*, Phys. Rev. B - Condens. Matter Mater. Phys. **88**, 1 (2013).

[39] T. Li and G. Galli, *Electronic Properties of MoS 2 Nanoparticles*, J. Phys. Chem. C **111**, 16192 (2007).

[40] A. Splendiani, L. Sun, Y. Zhang, T. Li, J. Kim, C. Y. Chim, G. Galli, and F. Wang, *Emerging Photoluminescence in Monolayer MoS2*, Nano Lett. **10**, 1271 (2010).

[41] C. Zhang, A. Johnson, C. L. Hsu, L. J. Li, and C. K. Shih, *Direct Imaging of Band Profile in Single Layer MoS2 on Graphite: Quasiparticle Energy Gap, Metallic Edge States, and Edge Band Bending*, Nano Lett. **14**, 2443 (2014).

[42] H. Yu, G. Bin Liu, J. Tang, X. Xu, and W. Yao, *Moiré Excitons: From Programmable Quantum Emitter Arrays to Spin-Orbit–Coupled Artificial Lattices*, Sci. Adv. **3**, 1 (2017).

[43] W. J. Schutte, J. L. De Boer, and F. Jellinek, *Crystal Structures of Tungsten Disulfide and Diselenide*, J. Solid State Chem. **70**, 207 (1987).

[44] P. V. Nguyen, N. C. Teutsch, N. P. Wilson, J. Kahn, X. Xia, A. J. Graham, V. Kandyba, A. Giampietri, A. Barinov, G. C. Constantinescu, N. Yeung, N. D. M. Hine, X. Xu, D. H. Cobden, and N. R. Wilson, *Visualizing Electrostatic Gating Effects in Two-Dimensional Heterostructures*, Nature **572**, 220 (2019).

[45] A. M. Jones, H. Yu, N. J. Ghimire, S. Wu, G. Aivazian, J. S. Ross, B. Zhao, J. Yan, D. G. Mandrus, D. Xiao, W. Yao, and X. Xu, *Optical Generation of Excitonic Valley Coherence in Monolayer WSe 2*, Nat. Nanotechnol. **8**, 634 (2013).

[46] I. V. G. and A. A. F. K. S. Novoselov, A. K. Geim, S. V. Morozov, D. Jiang, Y. Zhang, S. V. Dubonos, *Electric Field Effect in Atomically Thin Carbon Films*, **306**, 666 (2016).

[47] W. H. Chae, J. D. Cain, E. D. Hanson, A. A. Murthy, and V. P. Dravid, *Substrate-Induced Strain and Charge Doping in CVD-Grown Monolayer MoS2*, Appl. Phys. Lett. **111**, (2017).

[48] F. Cadiz, E. Courtade, C. Robert, G. Wang, Y. Shen, H. Cai, T. Taniguchi, K. Watanabe, H. Carrere, D. Lagarde, M. Manca, T. Amand, P. Renucci, S. Tongay, X. Marie, and B. Urbaszek, *Excitonic Linewidth Approaching the Homogeneous Limit in MoS2-Based van Der Waals Heterostructures*, Phys. Rev. X **7**, 1 (2017).

[49] D. H. Lien, J. S. Kang, M. Amani, K. Chen, M. Tosun, H. P. Wang, T. Roy, M. S. Eggleston, M. C. Wu, M. Dubey, S. C. Lee, J. H. He, and A. Javey, *Engineering Light Outcoupling in 2D Materials*, Nano Lett. **15**, 1356 (2015).

[50] B. Radisavljevic, A. Radenovic, J. Brivio, V. Giacometti, and A. Kis, *Single-Layer MoS2 Transistors*, Nat. Nanotechnol. **6**, 147 (2011).

[51] C. R. D. L. Wang, I. Meric1,, P. Y. Huang, Q. Gao, Y. Gao, H. Tran, T. Taniguchi, K. Watanabe, L. M. Campos, D. A. Muller, J. Guo, P. Kim, J. Hone, K. L. Shepard, *One-Dimensional Electrical Contact To*, Sci. (New York, N.Y.)432 **342**, 614 (2013).

[52] R. Saito, Y. Tatsumi, S. Huang, X. Ling, and M. S. Dresselhaus, *Raman Spectroscopy of Transition Metal Dichalcogenides*, J. Phys. Condens. Matter **28**, (2016).

[53] M. Yamamoto, S. T. Wang, M. Ni, Y. F. Lin, S. L. Li, S. Aikawa, W. Bin Jian, K. Ueno, K. Wakabayashi, and K. Tsukagoshi, *Strong Enhancement of Raman Scattering from a Bulk-Inactive Vibrational Mode in Few-Layer MoTe2*, ACS Nano **8**, 3895 (2014).

[54] P. Tonndorf, R. Schmidt, P. Böttger, X. Zhang, J. Börner, A. Liebig, M. Albrecht, C. Kloc, O. Gordan, D. R. T. Zahn, S. M. de Vasconcellos, and R. Bratschitsch, *Photoluminescence Emission and Raman Response of Monolayer MoS2, MoSe2, and WSe2*, Opt. Express **21**, 4908 (2013).

[55] H. Terrones, E. Del Corro, S. Feng, J. M. Poumirol, D. Rhodes, D. Smirnov, N. R. Pradhan, Z. Lin, M. A. T. Nguyen, A. L. Elías, T. E. Mallouk, L. Balicas, M. A. Pimenta, and M. Terrones, *New First Order Raman-Active Modes in Few Layered*

Transition Metal Dichalcogenides, Sci. Rep. **4**, 1 (2014).

[56] B. Kardynal, *Excitonic States in Atomically Thin WSe 2 Semiconductor*.

[57] S. Shree, I. Paradisanos, X. Marie, C. Robert, and B. Urbaszek, *Guide to Optical Spectroscopy of Layered Semiconductors*, Nat. Rev. Phys. **3**, 39 (2021).

[58] T. Taniguchi and K. Watanabe, *Synthesis of High-Purity Boron Nitride Single Crystals under High Pressure by Using Ba-BN Solvent*, J. Cryst. Growth **303**, 525 (2007).

[59] G. Signorello, E. Lörtscher, P. A. Khomyakov, S. Karg, D. L. Dheeraj, B. Gotsmann, H. Weman, and H. Riel, *Inducing a Direct-to-Pseudodirect Bandgap Transition in Wurtzite GaAs Nanowires with Uniaxial Stress*, Nat. Commun. **5**, (2014).

[60] B. R. Carvalho, Y. Wang, S. Mignuzzi, D. Roy, M. Terrones, C. Fantini, V. H. Crespi, L. M. Malard, and M. A. Pimenta, *Intervalley Scattering by Acoustic Phonons in Two-Dimensional MoS2 Revealed by Double-Resonance Raman Spectroscopy*, Nat. Commun. **8**, 6 (2017).

[61] Z. Wang, Y. H. Chiu, K. Honz, K. F. Mak, and J. Shan, *Electrical Tuning of Interlayer Exciton Gases in WSe2 Bilayers*, Nano Lett. **18**, 137 (2018).

[62] S. Wu, J. S. Ross, G. Bin Liu, G. Aivazian, A. Jones, Z. Fei, W. Zhu, D. Xiao, W. Yao, D. Cobden, and X. Xu, *Electrical Tuning of Valley Magnetic Moment through Symmetry Control in Bilayer MoS 2*, Nat. Phys. **9**, 149 (2013).

[63] L. Debbichi, O. Eriksson, and S. Lebègue, *Electronic Structure of Two-Dimensional Transition Metal Dichalcogenide Bilayers from Ab Initio Theory*,

Phys. Rev. B - Condens. Matter Mater. Phys. **89**, 1 (2014).

[64] G. Wang, X. Marie, L. Bouet, M. Vidal, A. Balocchi, T. Amand, D. Lagarde, and B. Urbaszek, *Exciton Dynamics in WSe2 Bilayers*, Appl. Phys. Lett. **105**, 1 (2014).

[65] J. Förste, N. V. Tepliakov, S. Y. Kruchinin, J. Lindlau, V. Funk, M. Förg, K. Watanabe, T. Taniguchi, A. S. Baimuratov, and A. Högele, *Exciton G-Factors in Monolayer and Bilayer WSe2 from Experiment and Theory*, Nat. Commun. **11**, 1 (2020).

[66] Z. Sun, J. Beaumariage, Q. Cao, K. Watanabe, T. Taniguchi, B. M. Hunt, and D. Snoke, *Observation of the Interlayer Exciton Gases in WSe2-p:WSe2Heterostructures*, ACS Photonics **7**, 1622 (2020).

[67] A. M. Jones, H. Yu, J. S. Ross, P. Klement, N. J. Ghimire, J. Yan, D. G. Mandrus, W. Yao, and X. Xu, *Spin-Layer Locking Effects in Optical Orientation of Exciton Spin in Bilayer WSe 2*, Nat. Phys. **10**, 130 (2014).

[68] J. Lindlau, M. Selig, A. Neumann, L. Colombier, J. Förste, V. Funk, M. Förg, J. Kim, G. Berghäuser, T. Taniguchi, K. Watanabe, F. Wang, E. Malic, and A. Högele, *The Role of Momentum-Dark Excitons in the Elementary Optical Response of Bilayer WSe2*, Nat. Commun. **9**, 1 (2018).

[69] A. Ramasubramaniam, D. Naveh, and E. Towe, *Tunable Band Gaps in Bilayer Transition-Metal Dichalcogenides*, Phys. Rev. B - Condens. Matter Mater. Phys. **84**, 1 (2011).

[70] Z. Wang, L. Zhao, K. F. Mak, and J. Shan, *Probing the Spin-Polarized Electronic Band Structure in Monolayer Transition Metal Dichalcogenides by Optical Spectroscopy*, Nano Lett. **17**, 740 (2017).

[71] Z. Wang, J. Shan, and K. F. Mak, *Valley- and Spin-Polarized Landau Levels in Monolayer WSe2*, Nat. Nanotechnol. **12**, 144 (2017).

[72] M. He, P. Rivera, D. Van Tuan, N. P. Wilson, M. Yang, T. Taniguchi, K. Watanabe, J. Yan, D. G. Mandrus, H. Yu, H. Dery, W. Yao, and X. Xu, *Valley Phonons and Exciton Complexes in a Monolayer Semiconductor*, Nat. Commun. **11**, 1 (2020).

[73] E. Liu, J. Van Baren, C. T. Liang, T. Taniguchi, K. Watanabe, N. M. Gabor, Y. C. Chang, and C. H. Lui, *Multipath Optical Recombination of Intervalley Dark Excitons and Trions in Monolayer WSe2*, Phys. Rev. Lett. **124**, 196802 (2020).

[74] A. M. Jones, H. Yu, J. S. Ross, P. Klement, N. J. Ghimire, J. Yan, D. G. Mandrus, W. Yao, and X. Xu, *Spin-Layer Locking Effects in Optical Orientation of Exciton Spin in Bilayer WSe 2*, Nat. Phys. **10**, 130 (2014).

[75] A. Kormányos, G. Burkard, M. Gmitra, J. Fabian, V. Zólyomi, N. D. Drummond, and V. Fal'ko, *K · P Theory for Two-Dimensional Transition Metal Dichalcogenide Semiconductors* , 2D Mater. **2**, 022001 (2015).

[76] W. Zhao, Z. Ghorannevis, L. Chu, M. Toh, C. Kloc, P.-H. Tan, and G. Eda, *Evolution of Electronic Structure in Evolution of Electronic Structure in Atomically Thin Sheets of WS2 and WSe2*, ACS Nano 791 (2013).

[77] Z. Li, T. Wang, C. Jin, Z. Lu, Z. Lian, Y. Meng, M. Blei, S. Gao, T. Taniguchi, K. Watanabe, T. Ren, S. Tongay, L. Yang, D. Smirnov, T. Cao, and S. F. Shi, *Emerging Photoluminescence from the Dark-Exciton Phonon Replica in Monolayer WSe2*, Nat. Commun. **10**, 1 (2019).

[78] E. Liu, J. Van Baren, T. Taniguchi, K. Watanabe, Y. C. Chang, and C. H. Lui, *Valley-Selective Chiral Phonon Replicas of Dark Excitons and Trions in Monolayer WS E2*, Phys. Rev. Res. **1**, 1 (2019).

[79] Z. Li, T. Wang, C. Jin, Z. Lu, Z. Lian, Y. Meng, M. Blei, M. Gao, T. Taniguchi, K. Watanabe, T. Ren, T. Cao, S. Tongay, D. Smirnov, L. Zhang, and S. F. Shi, *Momentum-Dark Intervalley Exciton in Monolayer Tungsten Diselenide Brightened via Chiral Phonon*, ACS Nano **13**, 14107 (2019).

[80] G. Aivazian, Z. Gong, A. M. Jones, R. L. Chu, J. Yan, D. G. Mandrus, C. Zhang, D. Cobden, W. Yao, and X. Xu, *Magnetic Control of Valley Pseudospin in Monolayer WSe 2*, Nat. Phys. **11**, 148 (2015).

[81] A. Srivastava, M. Sidler, A. V. Allain, D. S. Lembke, A. Kis, and A. Imamoɨlu, *Valley Zeeman Effect in Elementary Optical Excitations of Monolayer WSe 2*, Nat. Phys. **11**, 141 (2015).

[82] D. MacNeill, C. Heikes, K. F. Mak, Z. Anderson, A. Kormányos, V. Zólyomi, J. Park, and D. C. Ralph, *Breaking of Valley Degeneracy by Magnetic Field in Monolayer ${\mathrm{MoSe}}_{2}$*, Phys. Rev. Lett. **114**, 37401 (2015).

[83] Y. Li, J. Ludwig, T. Low, A. Chernikov, X. Cui, G. Arefe, Y. D. Kim, A. M. Van Der Zande, A. Rigosi, H. M. Hill, S. H. Kim, J. Hone, Z. Li, D. Smirnov, and T. F. Heinz, *Valley Splitting and Polarization by the Zeeman Effect in Monolayer MoSe2*, Phys. Rev. Lett. **113**, 1 (2014).

[84] Y. C. Chang, T. C. McGill, and D. L. Smith, *Model Hamiltonian of Donors in Indirect-Gap Materials*, Phys. Rev. B **23**, 4169 (1981).

[85] W. Davenport, *Linear Augmented-Slater-Type-Orbital Method for Electronic-Structure Calculation*, Phys. Rev. B **29**, (1984).

[86] R. E. Watson, J. W. Davenport, and M. Weinert, *Linear Augmented-Slater-Type-Orbital Method for Electronic-Structure Calculations. IV. 5d-5d Alloys*, Phys. Rev. B **34**, 8421 (1986).

[87] Y. C. Chang, R. B. James, and J. W. Davenport, *Symmetrized-Basis LASTO Calculations of Defects in CdTe and ZnTe*, Phys. Rev. B - Condens. Matter Mater. Phys. **73**, 1 (2006).

[88] K. Kunc, M. Balkanski, and M. A. Nusimovici, *Lattice Dynamics of Several ANB8–N Compounds Having the Zincblende Structure. III. Trends in Model Parameters*, Phys. Status Solidi **72**, 249 (1975).

[89] H. Sahin, S. Tongay, S. Horzum, W. Fan, J. Zhou, J. Li, J. Wu, and F. M. Peeters, *Anomalous Raman Spectra and Thickness-Dependent Electronic Properties of WSe2*, Phys. Rev. B - Condens. Matter Mater. Phys. **87**, 1 (2013).

[90] R. Hanson, L. P. Kouwenhoven, J. R. Petta, S. Tarucha, and L. M. K. Vandersypen, *Spins in Few-Electron Quantum Dots*, Rev. Mod. Phys. **79**, 1217 (2007).

[91] Z. Jin, X. Li, J. T. Mullen, and K. W. Kim, *Intrinsic Transport Properties of Electrons and Holes in Monolayer Transition-Metal Dichalcogenides*, Phys. Rev. B - Condens. Matter Mater. Phys. **90**, 1 (2014).

[92] M. S. Diware, K. Park, J. Mun, H. G. Park, W. Chegal, Y. J. Cho, H. M. Cho, J. Park, H. Kim, S. W. Kang, and Y. D. Kim, *Characterization of Wafer-Scale MoS2 and WSe2 2D Films by Spectroscopic Ellipsometry*, Curr. Appl. Phys. **17**, 1329 (2017).

[93] K. S. Novoselov, *Nobel Lecture: Graphene: Materials in the Flatland*, Rev. Mod. Phys. **83**, 837 (2011).